Solid-State Spin-Integrated Circuits for Quantum Sensing and Control

by

Christopher C. Foy

B.S., Physics, Georgia Institute of Technology (2012)
S.M. Electrical Engineering and Computer Science, Massachusetts Institute of Technology (2016)

Submitted to the Department of Electrical Engineering and Computer Science
in partial fulfillment of the requirements for the degree of

Doctor of Philosophy

at the

MASSACHUSETTS INSTITUTE OF TECHNOLOGY

May 2020

Author .....
Department of Electrical Engineering and Computer Science
May 14, 2020

Certified by .....
Dirk R. Englund
Associate Professor of Electrical Engineering and Computer Science
Thesis Supervisor

Accepted by .....
Leslie A. Kolodziejski
Professor of Electrical Engineering and Computer Science
Chair, Department Committee on Graduate Students

Solid-State Spin-Integrated Circuits for Quantum Sensing and Control

by

Christopher C. Foy

Submitted to the Department of Electrical Engineering and Computer Science
on May 14, 2020, in partial fulfillment of the
requirements for the degree of
Doctor of Philosophy

Abstract

Spin systems are an increasingly important quantum-sensing platform. In particular, atomic defect centers in diamond called nitrogen-vacancy (NV) centers offer impressive room temperature imaging capabilities for both magnetic fields and temperature. NV-based sensing platforms have found utility in solid-state physics, biological systems, and vector magnetometry. These applications highlight the immense promise of NV quantum sensors. Despite this promise, the use of NV centers within commercial devices remains limited to date, with many impediments to transitioning this platform from the laboratory.

This thesis describes the development of solid-state spin-integrated circuits (S^3IC) for quantum sensing and control with the overarching goal of creating scalable NV platforms. We present two major experiments that develop S^3IC. These expand the application space of NV centers and improve device functionality. The first application was to develop an NV spin microscope capable of wide-field temperature and magnetic field imaging to elucidate functional device behavior at the microscopic scale. The second experiment was integrating the essential components of an NV spin microscope, spin control and detection, with integrated electronics. In this manner, S^3IC combines the exceptional sensitivity of NV centers with the robustness and scalability of modern electronic chip-scale platforms. This co-integration of spin systems into integrated electronics shows a potential path for migrating previous proof-of-principal sensing demonstrations into affordable packages that demonstrate both much greater system integration and custom electronic architectures. In short, this work demonstrates advances in NV-ensemble quantum sensing platforms and establishes a foundation for future integration efforts, perhaps inspiring innovations in both application space and the development of new quantum devices.

Thesis Supervisor: Dirk R. Englund
Title: Associate Professor of Electrical Engineering and Computer Science

Acknowledgments

I would like to acknowledge Carl Sagan, whose calm voice pushed a young mind to explore science. A large thanks is given to my high school physics teacher, Dr. Houston, who encouraged me to pursue physics. He was an under-appreciated jewel and his passion for the sciences was instilled in me.

Further, I would like to thank Kurt Broderick and James Dayley for teaching me fabrication skills. They were also very kind to act as sounding boards to bounce ideas off. These technicians were always willing to offer feedback and give advice; and I am very grateful. I would also like to thank David L Lewis at the Cypress Machine Shop. His help in learning machining was invaluable in the completion of this work. I am lucky to know them.

This thesis could not have been assembled without help from my colleagues within the Quantum Photonics Group. In particular, Matt Trusheim's input was essential for developing many of the ideas within this work. I would also like to thank Sinan Karaveli. His ability to use every piece of equipment in the lab was very helpful, and he has taught me much. While we were forced to work together because we shared an optical table, I am glad to consider him a friend. Florian Dolde, Tim Schroder, Lorenzo De Santis, Mikkel Heuck, Ryan Hamerly, Edward Chen, Hannah Clevenson, Luozhou Li, Sara Mouradian, Jiabao Zheng, and Catherine Lee also gave significant help. Of course my fellow group members, who are too many to be stated here, deserve my sincerest gratitude. Nevertheless I must try: Kevin Chen, Hyeongrak (Chuck) Choi, Ian Cristen, Erik Eisenach, Jordan Goldstein, Tsung-Ju (Jeff) Lu, Christopher (Chris) Panuski, Cheng Peng, Mihika Prabhu, Noel Wan, Michael Walsh, Reyu Sakakibara, and Hyowon Moon. I also was fortunate to work with younger scientists who will shape the field of quantum science into the future: Isaac Harris, Liane Sarah Belamd Bernstein, Sarah Elizabeth Muschinske, Alex Sludds, Maddie Sutula, Saumil Bandyopadhyay, and Reggie Wilcox. I would like to particularly thank Donggyu Kim for his help and for agreeing to play the piano at my wedding. Eric Bersin was also a helpful if jaded confidant; he is great because he has one's back

in the middle of a dungeon (D&D).

This dissertation would not have been possible without help from my coauthors, to whom I owe many thanks: Lenan Zhang, Kevin Bagnall, Evelyn N. Wang, Shai Maayani, Yoel Fink, Or A. Shemesh, Ishan Gupta, Ophir Gaathon, Abraham Wolcott, and Edward S. Boyden. I would like to particularly thank Mohamed I. Ibrahim, who is simultaneously my best and worst collaborator. Not only is he incredibly hardworking and creative, but he is helpful to have around to move a couch. Many thanks to all my coworkers and their companionship during the long hours in lab.

James Fujimoto has been my academic advisor at MIT and helped me make sure I was always staying on top of the myriad array of department obligations. I would also like to thank Janice Balzer. She holds the Englund group together with tireless background work to make sure everything runs smoothly. She deserves a raise (note to Dirk).

I would also like to thank my fiance Constance Zhu for the thankless, and perhaps unknown, job of checking up on me during the writing of this thesis to confirm that I had not yet shed my mortal coil. I would also like to thank her for her cooking. She is the light of my life.

My friends that I made at Georgia Tech also deserve acknowledgment. These fellow students, and our shared memories, will always be remembered fondly. Here is a thanks to all these friends who live on distant shores. May time never weaken our bonds.

I would also like to thank my family. They supported me when I was too young to support myself and for better or worse, shaped me into who I am today. To my brothers (Shawn and Josh Foy), with whom I frequently fought in my youth, I would also like to offer thanks. Of course a special thanks should be given to my mother (Serena Sheerahamed) and father (Gary Foy).

Finally I would like to acknowledge my committee members. First my advisor, Dirk Englund. His help was invaluable. I am thankful for his advice over the many years that I strove to complete my PhD. I could always count on him (and the MIT Writing Center) to correct my grammar. His love of science and creativity shine

through in every interaction. He always has a new idea to consider. I could not have asked for a better environment to pursue my scientific interests. Next, Danielle Braje gave great advice. I am glad that I was able to offer her excuses to get back into the lab. Finally, Ruonan Han, who is so nice (Do not lose your easy smile). Thanks for being on both my RQE and PhD Committee.

Contents

List of Figures

Chapter 1

Introduction

1.1 Overview of Quantum Sensing Platforms

Sensors are a vitally important technology with large influence [210, 115, 155, 58, 1, 104]. Of particular interest are sensing systems that aim to exploit quantum coherence for metrology[61] - known as quantum sensors. Within the last two decades, quantum sensors have advanced from Nobel Prize award-winning proof-of-principle experiments on quantum physics[139, 140, 64, 62, 138] into fully realized systems[153, 152]. These systems include atomic clocks[117, 98], superconducting quantum interference devices (SQUIDs)[51], and vapor-cell technologies such as spin exchange relaxation-free (SERF) magnetometers[174, 105, 121]. Quantum devices can achieve accuracy, repeatability, and precision approaching fundamental limits[167, 71, 44, 16]. In each case, quantum sensors offer the prospect of both evolutionary and revolutionary advances over their classical counterparts[199] with orders-of-magnitude better performance[61, 44] at the cost of increasing device complexity.

This thesis will focus on a subset of quantum sensing - magnetometry. Magnetometers can be used for many applications including nanoscale nuclear-magnetic resonance (NMR) spectroscopy[67, 30], magnetoencephalography (MEG)[78], tests of fundamental physics[104, 155], and device-level characterization[58]. Existing quantum magnetometers are poorly matched to these applications, because they require cryogenic systems (SQUIDs) or complex experimental apparatus (vapor-cell technolo-

gies). These limitations have piqued interest in nitrogen-vacancy (NV) color centers in diamond[1]. An NV center is an atom-like system that has a variety of technical and fundamental properties that make for an attractive sensing platform. These properties include (i) its long spin dephasing time under ambient conditions, (ii) coherent microwave spin manipulation, (iii) optical spin-state initialization and readout, and (iv) the relative technological simplicity of its platform. This combination of characteristics has led to rapid development. Within a decade, NV centers have advanced from initial proposals [188, 43] and demonstrations [127, 12, 2, 46, 160] to applications spanning condensed matter physics[32, 58], biology[165, 215], NMR[215], Earth and planetary science[65], and vector magnetometry[71, 89].

1.2 The NV center as a Platform for Quantum Sensing

NV centers in diamond have attracted great interest because of their exceptional spin properties at room temperature; NV centers exhibit outstanding nanoscale sensitivity to both magnetic fields[127, 12, 70, 96, 66, 182] and temperature[135, 112] while offering broadband sensing capabilities[16, 17, 177, 118, 26, 214, 31, 183, 120, 149, 175, 27, 169, 170, 192, 32, 192, 144]. In addition, NV platforms excel in their technical simplicity[16, 69, 8, 94] relative to alternative technologies[71] requiring only commercial RF components and visible optical elements, detection devices, and sources. In particular, effective optical initialization and readout of NV spins do not require specialized lasers systems. NV experiments are commonly performed with commercial 532 nm solid-state lasers or even light-emitting diodes[137]. NV sensing platforms are solid state, being naturally "trapped" in stable, well-defined spatial locations within the host diamond. Further, NV centers do not require cryogenics, vacuum systems, or large applied bias fields to operate at ambient conditions. The NV is remarkably photostable, exhibiting neither photobleaching nor blinking[160]. Amazingly, NV-diamond sensors are incredibly durable, operating at pressures up to 60 GPa[92, 47]

and over immense temperature ranges (cryogenic to 700 K[195, 196, 151]). Furthermore, the chemical inertness of diamond allows for compatibility with biological samples[110, 176]. These properties make NV-based sensing platforms an attractive candidate for magnetic field and temperature (MT) imaging with nanometer-scale spatial resolution[69, 8, 94, 35].

To realize the tremendous promise of NV centers in diamond and transition this platform from the laboratory into actual commercial devices[1], several important impediments must be overcome. These include shrinking NV optical setups from optical table size to chip scale, making them easier to use while expanding their functionality. Consequently, this dissertation focuses on the creation of an efficient NV-based quantum sensing platform through the development of solid-state spin-integrated circuits (S^3IC). S^3IC platforms use the NV centers as both probes of integrated circuits (IC), offering valuable insight into device-level characterization, and as co-integrated components necessary for device performance. These experiments highlight the symbiotic relationship of S^3IC devices. S^3IC devices serve as a diagnostic tool to simultaneously probe device-level electrical current profiles[91, 58] and elucidate device thermophysical properties and heat transport[222, 58]; likewise they act as efficient spin interfaces, enabling a scalable implementation of quantum-classical control hardware[87, 102, 89]. This synergistic relationship, where spin systems both improve and are advanced by modern micro processing techniques, is an integral component towards realizing next-generation quantum sensing platforms based on NV-spin ensembles.

The main contributions of this thesis are the development of S^3IC for both quantum sensing and control. These contributions are achieved through two experiments. The first developed an NV spin microscope capable of wide-field temperature and magnetic field imaging. We used NV centers hosted within nanodiamonds to elucidate functional device behavior at the microscopic scale. In particular, we studied systems that have strong electro-thermal coupling. We analyzed both a dynamic process, electromigration, and a commercial device: gallium nitride high electron mobility transistors (GaN HEMTs). This platform allowed us to study device physics at chip-scale. The second experiment integrated the essential components of an NV spin micro-

scope, spin control and detection, with complementary metal–oxide–semiconductors (CMOS). We developed a highly scalable microwave (MW) launcher that generates uniform MW fields. We also developed CMOS-compatible green filters. This quantum sensing chip prototype combined the exceptional sensitivity of NV centers with the robustness and scalability of CMOS. The co-integration of spin systems into integrated electronics shows a potential path for migrating previous proof-of-principal sensing demonstrations into affordable packages that demonstrate both much greater system integration and custom electronic architectures. This work demonstrates advances in NV-ensemble quantum sensing platforms and establishes a foundation for future integration efforts, perhaps inspiring innovations in both application space and the development of new quantum devices.

1.3 This Work

1.3.1 Organization of this dissertation

1.3.2 Publications

Much of the work presented in this dissertation has been previously published or submitted for publication. Main works contributing to this thesis[1]:

- [58]: **Christopher Foy**, Lenan Zhang, Matthew E. Trusheim, Kevin R. Bagnall, Michael Walsh, Evelyn N. Wang, and Dirk R. Englund. Wide-field magnetic field and temperature imaging using nanoscale quantum sensors. ArXiv e-prints, 2019.

- [102]: Donggyu Kim*, Mohamed I. Ibrahim*, **Christopher Foy***, Matthew E. Trusheim,Ruonan Han, and Dirk R. Englund. A CMOS-integrated quantum sensor based on nitrogen–vacancy centres. Nature Electronics, 2(7):284–289, 2019.

[1] *Equal Contributions to manuscript

- [89]: Mohamed I. Ibrahim*, **Christopher Foy***, Dirk R. Englund, and Ruonan Han. High-scalability CMOS quantum magnetometer with spin-state excitation and detection in diamond color centers. ArXiv e-prints, 2020

Works contributing in smaller part to this thesis include:

- [122]: Shai Maayani, **Christopher Foy**, Yoel Fink, and Dirk R. Englund. Distributed quantum fiber magnetometry. Laser & Photonics Reviews, 2019.

- [176]:Or A. Shemesh*, Ishan Gupta*, Ophir Gaathon, **Christopher Foy**, Sinan Karaveli, Jae-Byum Chang, Asmamaw Wassie, Abraham Wolcott, Daniel A. Martin-Alarcon, Reyu Sakakibara, Dirk Englund, and Edward S. Boyden. Membrane targeted delivery of nitrogen-vacancy nanodiamonds. In preparation, 2020.

  Chapters 2, 3, 4, 5, and 6 reproduce and adapt material from previous published works. Chapter 3 is adapted from Ref. [58], with Chapter 4 and 5 being adapted from Ref. [87], [102], and [89]. In addition, sections of chapter 6 report results from references [122] and [176].

1.3.3 Co-worker Contributions

The work presented in this dissertation would not have been possible without my many active collaborations. This highly interdisciplinary work required the valuable contributions of my research colleagues and collaborators. First, my advisor, Dirk Englund, oversaw all projects contained within this dissertation; his advice was invaluable for the completion of this work. The rest of my co-workers' contributions are summarized below.

The work described in Chapter 3 was chiefly envisioned, designed, and implemented by myself. However, Lenan Zhang, Matt Trusheim, Kevin Bagnall, Michael Walsh, and Evelyn Wang all made substantial contributions. Lenan and Kevin acquired the GaN HEMTs and helped design the experiments, analyze the data, simulate the thermal interfaces, and write the manuscript for publication[58]. Matt initially

mentored me on NV spin physics and with the development of the model. Finally, Michael developed the original MATLAB code base used in this work.

Donggyu Kim, Mohamed Ibrahim, and I participated equally in the reproduced work shown within Chapter 4. Together we conceived the diamond–CMOS integration, with the assistance of our advisors Dirk Englund and Ruonan Han. Mohamed developed the idea of stacking the microwave inductor, plasmonic filter, and photodiode within the 3D architecture. Mohamed and myself contributed chiefly to the chip specifications. Donggyu and I equally did the experimental design. Donggyu performed the FDTD simulations for the optical filter design. I wrote the MATLAB source code to control the experiment and, with significant help from Donggyu, constructed the optical setup. All authors contributed to the writing of the manuscripts [87, 102].

The work presented in Chapter 5 was done equally by Mohamed and myself. We both put considerable effort into the chip design with Mohamed developing both the MW launcher and IC design. The optical setup, MATLAB code base, and diamond acquisition were led by myself. Mohamed and I performed the experiments, analyzed the data, and characterized the chip performance. Mohamed chiefly wrote the manuscript, with significant editing and analysis done by myself.

Chapter 6 presents two experiments spanning references [122] and [176]. In [122], Shai Maayani and I both developed the fiber geometry and experiments and analyzed the data. Shai constructed the fibre and did most of the experiments. We both wrote the manuscript. In contrast, in [176], Or Shemish and Ishan Gupta did most of the work, with me performing the experiments for Figure 4.

Chapter 2

Overview of the Nitrogen-vacancy Center

2.1 Nitrogen-vacancy Center Physics

The NV center is a crystallographic defect within diamond[187]. It is composed of a vacancy (a missing carbon atom from the diamond lattice) that is adjacent to a nitrogen impurity as shown in Figure 2-1a.

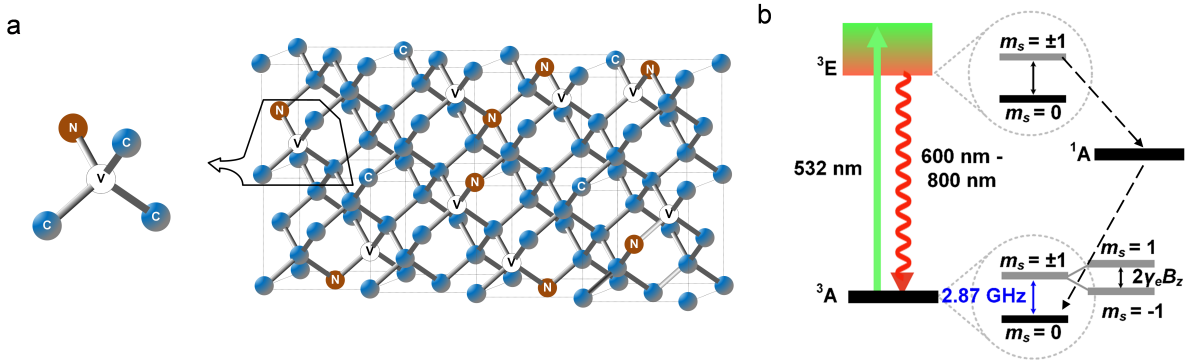

Figure 2-1: **Overview of the NV Center**. **a**, Atomic structure of the NV center, with nitrogen, vacancy, and carbon atoms identified. **b**, Simplified NV energy level diagram[46].

The NV is comprised of six electrons of which two are unpaired, yielding an effective spin 1 system[93, 161]. The room temperature energy level diagram for an NV is shown in Figure 2-1b. This diagram shows several transitions for the NV center.

The leftmost set of levels, ^{3}A and ^{3}E[14], are the electronic orbital states. These are a triplet ground state and a triplet excited state, respectively. The $|m_s = 0\rangle$ state shown in black and the lifted degenerate spin excited states, $|m_s = \pm 1\rangle$, are separated by an energy, h(2.87 GHz)[46, 160], which results from spin-spin coupling between the two unpaired electron spins. The degeneracy of the $|m_s = \pm 1\rangle$ spin states can be lifted by applying a magnetic field that has a component aligned with the NV's axis. In addition to radiative decay back to the $|m_s = 0\rangle$ state, the $|m_s = \pm 1\rangle$ states have another decay path through a metastable 1A state[126, 46]. Conventional NV optical readout exploits the $|m_s = \pm 1\rangle$ state's higher probability to couple to this singlet state relative to the $|m_s = 0\rangle$ state. NVs that couple to the singlet state do not fluorescence in the 600-800 nm band[73], whereas NV centers decaying directly to the spin-triplet ground state can continue to cycle between the ground and excited triplet states, generating fluorescence in the 600 - 800 nm band[16]. Thus, the NV has different fluorescence rates depending on its spin state. The decrease in emitted fluorescence distinguishes the $|m_s = \pm 1\rangle$ and $|m_s = 0\rangle$ spin states.

This spin-dependent fluorescence is shown in Figure 2-2 where the resonant frequencies of the $|m_s = \pm 1\rangle$ states are shown. The $|m_s = \pm 1\rangle$ resonance frequencies, $\epsilon_{\pm 1}$, are given by solving for the eigenvalues of the simplified room temperature NV Hamiltonian shown below[160]:

$$H/h = D(T)S_z^2 + E\left(S_x^2 - S_y^2\right) + \gamma B_z S_z \tag{2.1}$$

In Equation 2.1, γ is the NV gyromagnetic ratio, E is the NV's strain[160], *D(T)*[3] is the temperature-dependent NV zero field splitting parameter, $\vec{B}$ is the magnetic field, $\hat{z}$ is the normalized NV axis, and B_z is the axial magnetic field along $\hat{z}$. Thus, fluctuations in the NV's local thermal environment change the $|m_s = 0\rangle \rightarrow |m_s = \pm 1\rangle$ zero field splitting parameter, *D(T)*[3], whereas magnetic fields lift the degeneracy of the NV's $|m_s = \pm 1\rangle$ state through the Zeeman effect[188]. For weak non-axial or aligned magnetic fields ($\vec{B} \sim B_z < 100$ mT), the resonance frequencies of the $|m_s = \pm 1\rangle$ states are determined by Equation[160] 2.2:

$$\epsilon(T, B_z)_{\pm 1} = D(T) \pm \sqrt{E^2 + (\gamma B_z)^2} \tag{2.2}$$

where again the $\epsilon_{\pm 1}$ are the NV resonance frequencies corresponding to the $|m_s = 0\rangle \rightarrow |m_s = \pm 1\rangle$ transitions[160].

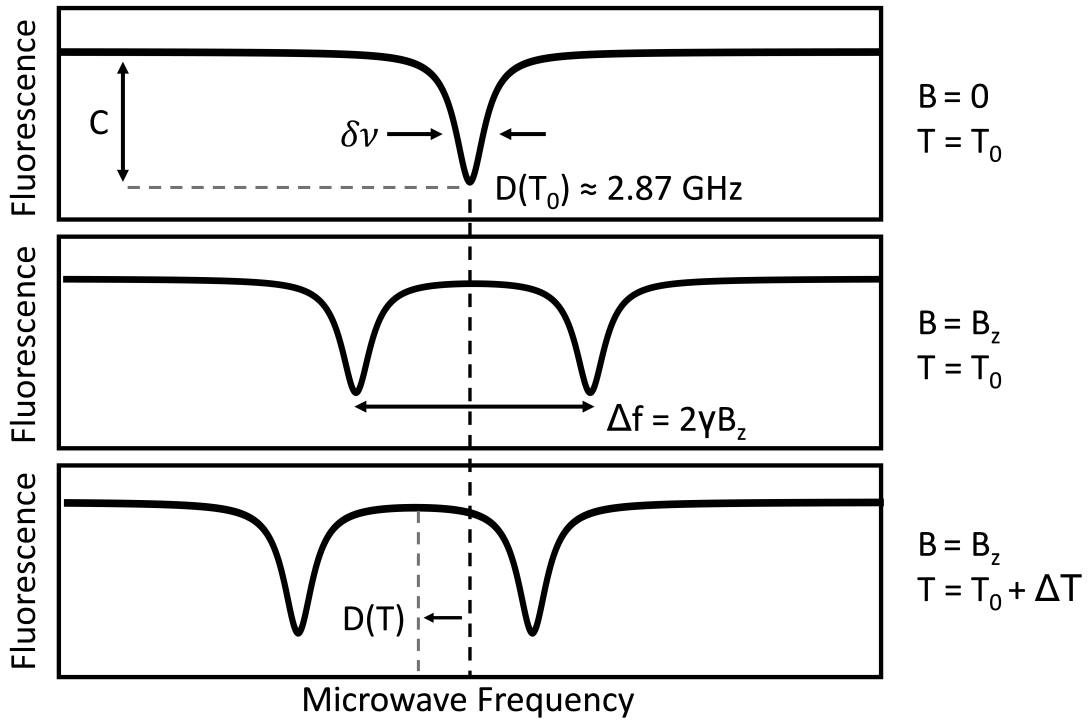

Figure 2-2: **NV ODMR Spectrum**. (a) idealized ODMR spectra of an NV center with both $B = B_z = 0$ and $\Delta T = 0$ with the $|m_s = \pm 1\rangle$ states shown. The normalized fluorescence difference, C, for the $|m_s = \pm 1\rangle$ states is indicated as well as the resonance linewidth $\delta\nu$. A magnetic field aligned to the NV axis causes the resonance to split by an amount given by $\Delta f = 2\gamma B_z$ (b) while an increase in temperature (c) causes a shift in *D(T)* to lower MW frequency.

We optically detect the $\epsilon_{\pm 1}$ transitions through the NV magnetometry protocol called continuous-wave optically detected magnetic resonance (CW-ODMR)[50, 171, 193, 17, 166]. ODMR spectroscopy experiments[126, 60, 2] allow us to determine *D(T)* and B_z by determining the $\epsilon_{\pm 1}$ transitions. The effect of magnetic field and temperature on ODMR fluorescence is shown graphically in Fig:2-2. The difference between the two resonances is proportional to the applied axial magnetic field (Fig:2-

2b). The frequency, Δf, associated with such an energy gap is proportional to $|\overrightarrow{B_z}|$:

$$\Delta f = f_+ - f_- = 2\gamma_e|\overrightarrow{B_z}|, \tag{2.3}$$

where f_+ and f_- are the frequencies for the transitions from $|m_s = 0\rangle$ to $|m_s = +1\rangle$ and $|m_s = -1\rangle$, respectively. We use Δf to derive $\overrightarrow{B_z}$. The global shift, *D(T)*, is related to the change in the local temperature (Fig:2-2c).

An idealized ODMR spectrum of a single NV has the form

$$I(f; \epsilon, \delta\nu, C) = 1 - R\sum_{m=1}^{2} L(f; \epsilon_m, \delta\nu, C) \tag{2.4}$$

where R is the photon detection rate, $L(f; \epsilon, \delta\nu, C)$ is the three-parameter Lorentzian function, f is the microwave frequency, $\delta\nu$ is the linewidth of the transition, and C is the normalized change in fluorescence rate between the $|m_s = 0\rangle$ and $|m_s = \pm 1\rangle$ states. Single crystal diamond has four NV spin populations which separately lay along the tetrahedral axes of the host diamond. Accordingly, an external magnetic field $\overrightarrow{B_{\text{ext}}}$ has four projections – $\overrightarrow{B_{z1}}$, $\overrightarrow{B_{z2}}$, $\overrightarrow{B_{z3}}$, $\overrightarrow{B_{z4}}$ – along the NV orientations. This leads to four pairs of splitting in a single ODMR measurement (Fig:2-3). Therefore, NV centers have a vector-field measurement capability by monitoring the different magnetic field projects and reconstructing $\overrightarrow{B_{ext}}$. That is advantageous over conventional Hall and fluxgate-based sensors, where three devices in *x- y- z-* axes are needed for vector detection.

2.2 Overview of ODMR Optical Setup

CW-ODMR is a simple and widely employed magnetometry method[60, 2]. The simplicity originates because both the MW driving field and the optical polarization and readout occur incoherently. Laser excitation continuously polarizes NV centers into the bright state ($|m_s = 0\rangle$) while resonant microwaves drive the NVs' spin population into the less fluorescent $|m_s = \pm 1\rangle$ states, reducing the emitted fluorescence.

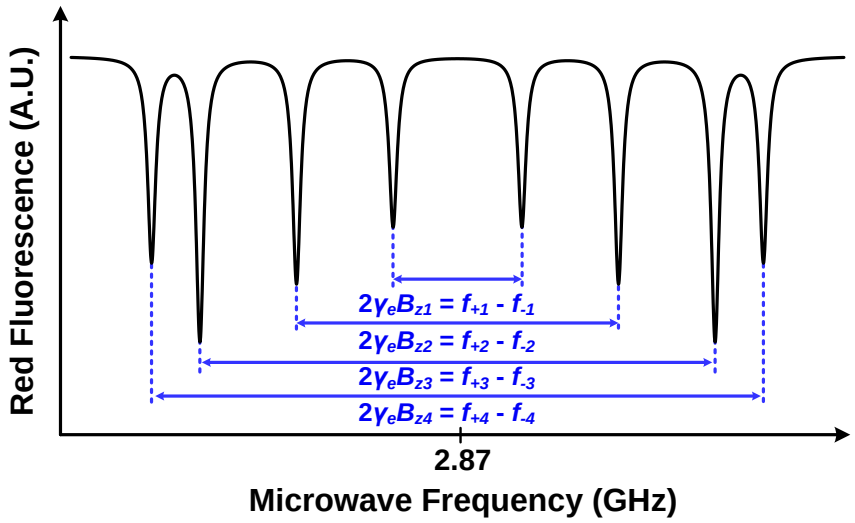

Figure 2-3: **Zeeman Splitting of Bulk Diamond ODMR.**The red-fluorescence intensity of the diamond at varying microwave frequency. An external magnetic-field bias is applied with projections along the four N-V axes.

This work focuses on the detection of the NV-ODMR fluorescence with cameras. Unlike APDs or photodiodes, cameras offer the key advantage of straightforward parallelization of ODMR to provide magnetic field and temperature wide-field imaging with micrometer-scale spatial resolution[113]. Thus, we emphasize design considerations that should be considered for imaging NV-ODMR fluorescence. Chapter 3 showcases the advantages of this approach.

Fig:2-4 is a schematic for the CW-ODMR fluorescence imaging optical setup used within this thesis. This experiment apparatus, sometimes referred to as a "spin microscope," is used to transduce NV-ODMR fluorescence into images of the magnetic field and temperature spatial profile. This work uses a single pass geometry[182] rather than a multi pass[39] or total-internal-reflection geometry[66]. The green (532 nm) laser used to excite the NV centers and for optical polarization is directed through an objective. Thus, engineering this excitation path for a desired field of view (FOV) is crucial. Further, while modulating this light is not required, it is still useful both experimentally and for more advanced NV-sensing protocols (2.4). Thus two key criteria need to be considered: choosing a beam diameter inside the AOM for optimized diffraction efficiency and rise time and choosing both f_5 and the objective for a de-

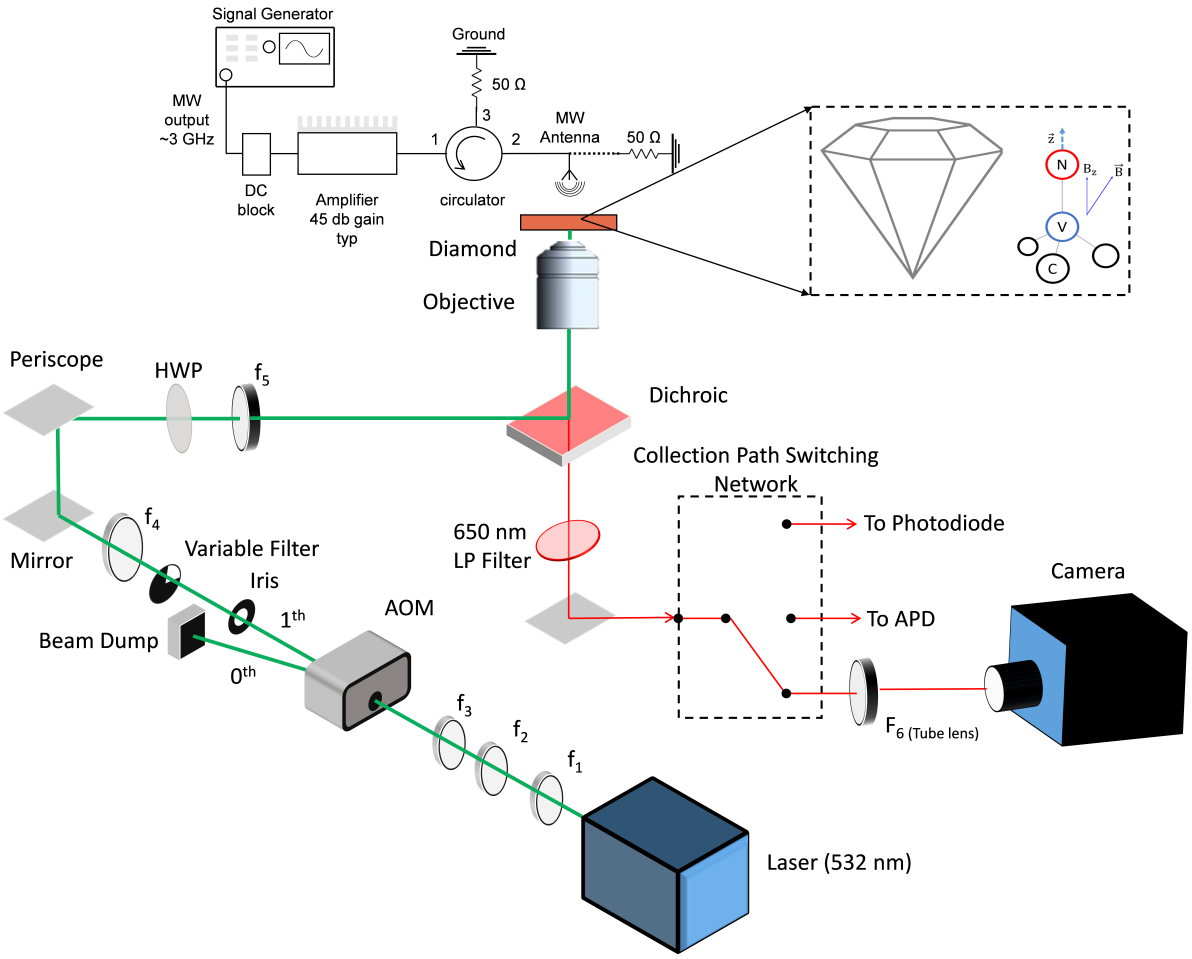

Figure 2-4: **NV-ODMR Setup Schematic**. Green 532 nm laser light is first demagnified by the first two lenses to shrink the required optical path length. A third positive lens focuses the beam into an acoustic-optical modulator (AOM). The zeroth-order beam is absorbed by a beam dump while the first-order diffracted beam passes through both an iris and a variable filter. A fourth lens collimates the beam. A periscope directs the beam toward the diamond where a half-wave plate allows optimization of the beam polarization to maximize NV fluorescence for all NV orientations. A fifth lens focuses the beam onto the back aperture of the objective after reflecting off a dichroic. The ODMR fluorescence is collected by the objective and directed toward the switching network where, depending on flipper mirror orientation (not shown), the fluorescence is either (i) imaged by a camera or (ii) detected by a photodiode or an avalanche photodiode (APD). Simultaneously, MW fields are generated, amplified, and then radiated to drive the NV's spin population.

sired FOV and collection efficiency. To resolve the first, we use the lens triplet shown (f_1, f_2, and f_3) in Fig:2-4. The first lens pair (f_1 and f_2) demagnifies the laser beam by an amount equal to f_2/f_1. This process reduces f_3 by the amount determined by

Equation 2.5[136]:

$$f_3 = \frac{4}{1.27}\frac{w_{AOM}}{(532nm)}\frac{w_0}{f_2/f_1} \tag{2.5}$$

where w_0 is the inital waist emitted by the laser, and w_{AOM} is the desired waist within the AOM. w_{AOM} is determined by referring to the AOM datasheet. Thus, f_2/f_1 acts to reduce the needed optical path length to reach w_{AOM}.

After the AOM, another lens triplet (f_4, f_5 , and $f_{objective}$) needs to be determined. The first-order diffracted beam is sent through an iris to reduce stray light, and then a variable filter is used to control the light intensity. To determine the beam waist at the sample surface (w_{sample}), the magnification of the entire system needs to be determined. Equation 2.6 determines w_{sample}:

$$w_{sample} = w_0 * M = w_0\frac{f_2}{f_1}\frac{f_4}{f_3}\frac{f_{objective}}{f_5} \tag{2.6}$$

Within Equation 2.6, f_1, f_2, and f_3 are already constrained. Further, as objectives are often determined based on their numerical apertures and working distance, $f_{objective}$ is often not a free parameter. Thus only f_4 and f_5 are free to be chosen.

Once the NVs are excited, their photoluminescence is collected by the objective and subsequently colliminated. This collected fluorescence is filtered by a 650 nm long pass filter to eliminate NV^0 background[4, 66] and subsequently imaged by a camera. For optimal image quality, the diameter, position, and value of f_6 need to be determined. We start by determining the exit pupil diameter of the objective, $d_{\text{objective}}$, which is given by [141]

$$d_{\text{objective}} = 2f_{\text{objective}} * NA \tag{2.7}$$

with the maximum distance between the tube lens and the objective constrained by[141]

$$L = \frac{(d_{\text{tubelens}} - d_{\text{objective}})}{d_{\text{objective}}}f_6 \tag{2.8}$$

Finally, f_6, should be chosen to have the maximum magnification possible to completely fill the camera CCD area. Thus, $f_6/f_{\text{objective}} * w_{\text{sample}}$ should equal the CCD

radius.

Many parameters must be considered when deciding on the camera. These include, but are not limited to, quantum efficiency (QE), frame rate, pixel size, pixel well depth, and read noise. Each of these directly impacts critical parameters of the spin microscope. For optimal choice of a camera, the exact experimental specifications need to be carefully considered. For example, the spatial resolution of the system will be $\max([\frac{\lambda}{2NA}, \frac{pixelsize}{f_6/f_{\text{objective}}}])$. Thus, the pixel size needs to be considered in order to reach diffraction limited performance. Two limitations of cameras are their inability to suppress background fluorescence and their slow data acquisition rate, which reduces sensitivity. Interestingly, novel CMOS lock-in cameras (Heliotis heliCam C3) [22] designed for optical coherence tomography[52] solve both problems, offering an intriguing avenue for enhancing the sensitivity of spin microscopes[212]. These devices offers lock-in frequencies exceeding 250 KHz, allowing for effective noise suppression and faster data acquisition rates. This new camera technology should continue to be explored within the space of NV imagers.

2.3 Magnetic Sensitivity using CW-ODMR

To determine the shot-noise-limited sensitivity of an NV magnetometer performing CW-ODMR, we first reconsider Equation 2.2 and Equation 2.4. Changes in B_z and T will change the $\epsilon_{\pm 1}$ transitions and thus will impact I for a given on-resonance value of f. For a shot-noise-limited measurement duration, δt, the standard deviation is given by

$$\alpha = \sqrt{I \delta t} \tag{2.9}$$

For small C, the shot-noise-limited magnetic sensitivity, η_{B}, is given through the relation[171, 17, 50]

$$\eta(T/\sqrt{Hz}) = \delta B_{\min} \sqrt{\delta t} \approx \frac{\gamma \sqrt{R}}{\max\left|\frac{\partial I}{\partial f}\right|} \tag{2.10}$$

$$\eta \approx \alpha \frac{\gamma \delta \nu}{C \sqrt{R}} \tag{2.11}$$

where the α prefactor represents the steepest slope for an ODMR lineshape located at $f = \frac{\delta\nu}{2\sqrt{3}}$ [50]. For Lorentzian lineshapes, $\alpha = 4/3\sqrt{3} \approx 0.77$. Due to power broadening in CW-ODMR experiments, a gaussian lineshape may be observed[50, 17]. In this case, $\alpha = \sqrt{e/8\ln 2} \approx 0.7$[50].

Equation 2.11 determines the CW-ODMR magnetic field sensitivity. To determine the temperature sensitivity, the NV's gyromagnetic ratio γ (28 nT/Hz) must be replaced by the temperature variations of D. A temperature change causes both an expansion of the diamond's lattice (reducing spin-orbit coupling) and the NV's coupling to the diamond's phonon modes[3, 45]. These effects yield a room-temperature frequency shift of $\frac{\partial D}{\partial T} \approx 74$ KHz/°C[3, 45].

2.4 Alternative to CW-ODMR Magnetometry

CW-ODMR is easier to implement than other NV sensing protocols but suffers from many drawbacks. These originate from its incoherent excitation and MW driving. In addition, this method suffers from MW and optical power broadening, which degrades sensitivity[50]. Optimum sensitivity is reached when the optical excitation rate, MW driving frequency, and NV coherence time contribute equally to $\delta\nu$[50]. Under these conditions, the fluorescence rate is $\sim 10^3$ lower than the spin projection limit[17].

In contrast, there exists a range of magnetometry protocols which leverage the coherence of NV centers to significantly improve sensitivity[16]. Common modalities include pulsed ODMR [50, 17], Ramsey[157, 16, 166], echo-type sequences[76, 118, 26, 214], and double-quantum coherence magnetometry[124, 19]. Each of these protocols improves sensitivity by maximizing population transfer to the $|m_s = \pm 1\rangle$ states[50], improving spin readout, eliminating common mode noise sources (strain, temperature)[109], or by extending the NV's coherence time by sacrificing measurement bandwidth and sensitivity to static fields. For AC magnetometry, dynamical decoupling protocols extend the NV's coherence time typically by one to two orders of magnitude[111, 18] and approach the longitudinal spin relaxation time[130].

Each of the above protocols requires coherent control of the NV's spin state.

They also require the ability to have precise gating of coherent MW fields and optical excitation pulses. In many sensing demonstrations, particularly the ones that will be explored in this thesis, some or all of these criteria are not met. Given this limitation, CW-ODMR is a useful tool to demonstrate proof-of-principal measurements where improvements in sensitivity and functionality, through coherent phase control of the NV's spin state, can be left to future efforts.

Chapter 3

Wide-field Magnetic Field and Temperature Imaging using Nanoscale Quantum Sensors

3.1 Introduction

As described in Chapter 1.1, this thesis emphasizes the development of S^3IC devices. S^3IC devices integrate spin systems with integrated electronics to improve spin control, but also use the incredible advantages of NV quantum sensors to address the challenges facing ICs. One key challenge of ICs is the elucidation of functional device behavior[90], particularly for systems with coupled thermo-magnetic environments. Simultaneous MT measurements afforded by NV-based wide-field imaging optical setups are a favorable alternative to existing techniques which separately measure temperature (e.g., infrared (IR) microscopy[28], micro-Raman spectroscopy[28, 103], and thermo-reflectance microscopy[28]) or magnetic fields (e.g., scanning probe magnetic force microscopy and SQUIDs). Thus, this work highlights how diamond NV spin systems can be used as a diagnostic tool for ICs, further developing S^3IC.

High frame-rate wide-field MT imaging not only provides a better understanding of the current density inside devices, but detects current leakage or short circuits.

This is necessary to optimize the design and fabrication of electronics. Simultaneously, temperature imaging reveals device thermal transport and shows the evolution of hotspots, which is essential to estimate device lifetime and their failure mechanisms[21, 11]. For this reason, an imaging approach that offers simultaneous MT imaging provides valuable information. This information includes both electrical boundary conditions and thermal boundary resistance, which are critical for device-level electro-thermal modeling. This modeling guides both device performance optimization and chip-scale characterization.

In this chapter we use the exceptional temperature and magnetic field sensitivity of NV spins in conformally-coated nanodiamonds to realize simultaneous wide-field MT imaging at the device level. Our "quantum conformally-attached thermo-magnetic" (Q-CAT) imaging enables (i) wide-field, high-frame-rate imaging (100 - 1000 Hz); (ii) high sensitivity; and (iii) compatibility with standard microscopes. We apply this technique to study the industrially important problem of characterizing multifinger GaN HEMTs. We spatially and temporally resolve the electric current distribution and resulting temperature rise, elucidating functional device behavior at the microscopic level. The general applicability of Q-CAT imaging serves as an important tool for understanding complex MT phenomena in material science, device physics, and related fields.

The chapter introduces a typical use case for an NV-nanodiamond (NVND) magnetometer. Next we extend the ODMR model for NV centers developed in Chapter 2 to NVNDs, building on the works shown in Ref. [81, 128]. We also perform statistical characterization of NVND properties in regards to generating MT images. We emphasize the applicability of Q-CAT imaging by measuring a variety of material systems of increasingly complex coupled electro-thermal physics. The chapter also includes projections for a next-generation NVND imager with improved sensitivity and capability. Much of this chapter is adapted from Ref. [58].

3.2 Overview of Quantum-Conformally Attached Thermo-magnetic Imaging

NVNDs are an appealing sensor for MT imaging. NV centers in diamond have attracted great interest because of their exceptional spin properties under ambient conditions, exhibiting outstanding sensitivity to both magnetic fields[127, 12, 70, 96, 66, 182] and temperature[135, 112]. NVNDs have gained increased interest for their additional benefits and expanded application space. These applications include drug delivery[146], thermal measurements of biological systems[110, 178, 59, 186, 13, 165], and scanning magnetometer tips[191, 68]. Their small size allows both increased collection efficiency due to the reduction in total internal reflection and direct measurement of their local MT environment[165]. These characteristics make NVNDs an attractive platform for MT imaging assuming their corresponding deficiencies, variability in both sensor performance[58] and sample-NVND thermal interface [58], are mitigated.

While numerous temperature mapping techniques are broadly used for characterization– IR microscopy[28], micro-Raman spectroscopy [28, 108, 40], and thermo-reflectance microscopy[28]– each of these techniques has many undesirable features. IR and thermo-reflectance microscopy are both commonly used wide-field techniques but suffer from complicated calibration procedures and difficulties in measuring adjacent metal and semiconductor regions at the sample surface. Micro-Raman spectroscopy has the major advantage of directly probing the temperature in the active device layers, but is limited to serial acquisition with a $\sim$1 μm diameter spot. In addition, for device-level measurements, the micro-Raman thermometry signal couples temperature rise, stress, and electric field [11]. Decoupling this signal requires complicated calibration and is possible only for materials with more than three Raman peaks[11]. In contrast, the calibration for NVND sensing is relatively simple, owing to the atomic nature of the sensing platform, and is thus not affected by the multiphysics coupling inside the device. The wide-field nature of Q-CAT imaging provides orders-of-magnitude better frame rates than pixel-by-pixel scanning seen in micro-Raman

thermometry (Section 3.8). As an example, this thesis will show Q-CAT imaging's ability to probe the temporal evolution of the temperature distribution around a gold-glass microfabricated structure as it undergoes electromigration. Micro-Raman would poorly capture this dynamic process (Section 3.8). If the above techniques could capture the temperature profile, the electric/magnetic current distribution would still not be understood, or should be measured separately.

Q-CAT imaging is an attractive new diagnostic tool to measure the MT profiles of microelectronics with high spatial and temporal resolution. As an example, we consider Fig:3-1, which shows the temperature and magnetic profile of a field-effect transistor. A gate electrode modulates source-drain current, affecting the geometry-dependent magnetic fields (gold arrow) and temperature (red surface) spatial profile. High current densities at the gate cause high temperatures that accelerate device degradation[200]. To image this profile, we apply a film of NVNDs conformally on top of the device. Exciting the NVND ensembles within an FOV gives a fluorescence image similar to that seen in Fig:3-1 inset. Transducing these fluorescence images into MT images requires modeling how NVND fluorescence changes as a function of $\left|\vec{B}\right|$ and T.

3.3 Sensing with NVND Ensembles

Fig: 3-2a models how the ODMR spectra shown in Fig: 2-2 for single NV system evolves as the number of the NV centers, N, within a diffraction limited spot increases. Thus, as N for a given B_z within a diffraction-limited volume increases, the final observed ODMR spectrum is the sum of the individual NV ODMR spectra having the form

$$I(f;\epsilon,\delta\nu,C_{\mathrm{m}}) = 1 - R/(N)\sum_{i=1}^{N}\sum_{m=1}^{2} L(f;\epsilon_{\mathrm{mi}},\delta\nu,C) \tag{3.1}$$

NV centers located in single crystal bulk diamond can have at most 4 NV orientations[123, 209, 38, 166] which lie along the diamond's crystallographic axes.

As was shown in Equation 3.1, the resulting ODMR spectra is the sum of all

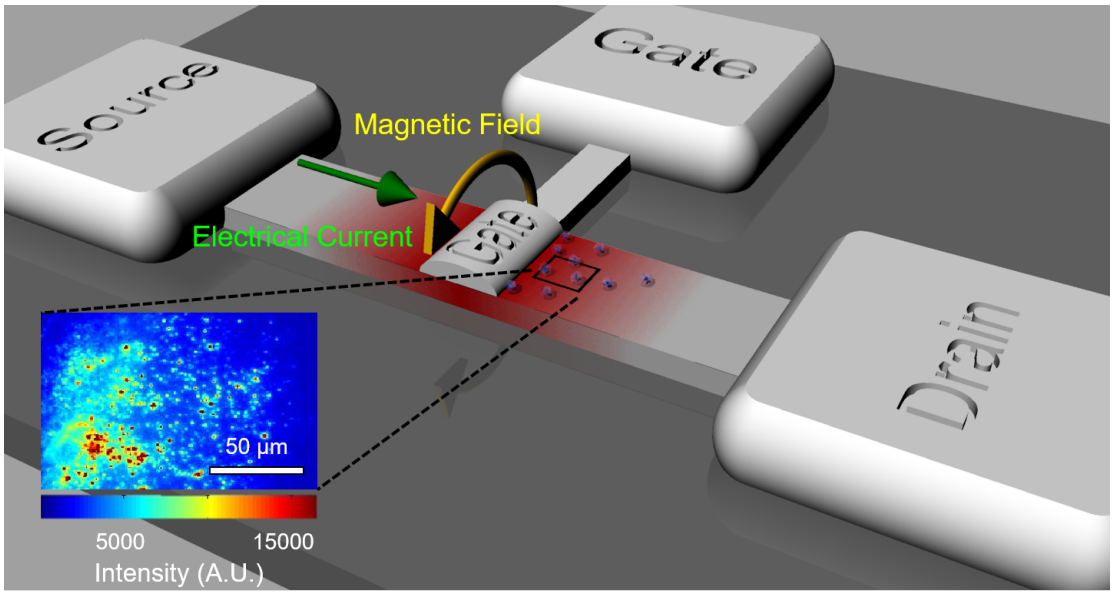

Figure 3-1: **Overview of Q-CAT imaging**. **a**, Illustration of an application of Q-CAT imaging. A transistor experiences joule heating from electric current flowing between the drain and the source. (Inset), Fluorescence image of deposited NVNDs. NVNDs act as local probes of the magnetic field and temperature along the channel.

N spectra. For NVND ensembles, the number of possible NV orientations is not fixed[35]. As the number increases, NV resonances are no longer individually resolvable, as shown in Fig: 3-2a. To describe this behavior, we model the NVND ensemble as an isotropic distribution of NV orientations, each oriented at an angle $\theta \in [0, \pi]$ with respect to the objective axis. The ODMR spectrum described by Equation 3.1 becomes

$$1 - I(f; T, \left|\vec{B}\right|, \delta\nu, C) \propto \int_0^{\pi} \sum_{m=1}^{2} R(\theta) L(f; \epsilon(T, \left|\vec{B}\right|)_{m\theta}, \delta\nu, C) \sin\theta d\theta \tag{3.2}$$

where the summation becomes an integral, and $R(\theta)$ represents the angular dependent weighting of the NV's normalized fluorescence value (see appendix A for full derivation).

Due to the isotropic nature of the NV orientations within N, Equation 3.2 and Fig: 3-2a show that NVNDs are insensitive to magnetic field orientation, so $B_z \rightarrow \left|\vec{B}\right|$. This makes NVND sensors a scalar magnetometer, in contrast to single-crystal NV ensembles with vector magnetometry capabilities[182, 166]. Fig: 3-2b shows that the

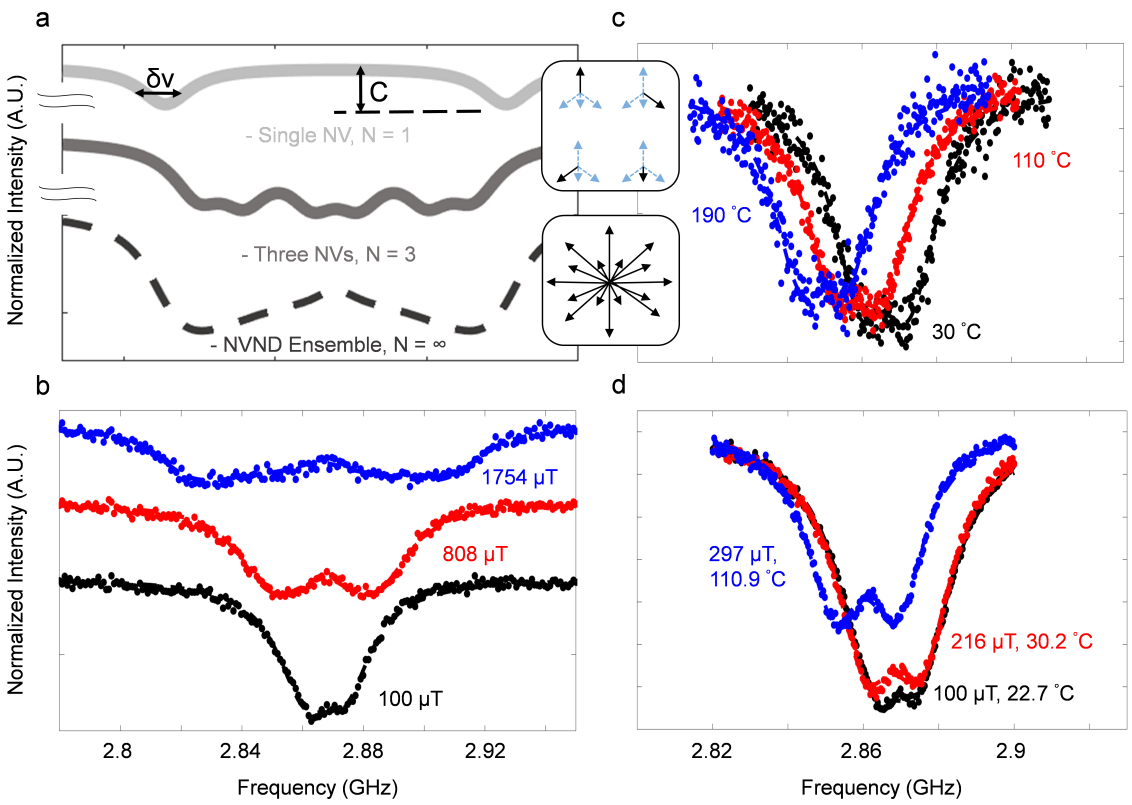

Figure 3-2: **Overview NVND ODMR Spectra**. **a**, Simulated ODMR spectra for the case of 1, 3 and infinite NVs within the diffraction limit for a given $\left|\vec{B}\right|$. Resonances seen in the ODMR spectra change are resolvable at low N, but become inhomogeneously broadened as $N \to \infty$. (inset), The top image shows NVs within defined crystallographic orientations such as those found in bulk diamond systems. The middle image shows 3 NV orientations constrained to the diamond's crystallographic orientations. The bottom image represents NVs found in aggregated polycrystalline diamond. The NVs are modeled to be spherically symmetrical around an origin (bottom inset). **b**, An increase in magnetic field broadens the ODMR curve. **c**, An increase in temperature shifts D to lower frequencies. **d**, The different responses of the NV ODMR spectrum to $\left|\vec{B}\right|$ and T allows for simultaneous measurements of the NVND's MT environment.

resulting NVND ODMR spectra broadens rather than maintains the discrete number of resonances previously observed as function of $\left|\vec{B}\right|$. Fig: 3-2c illustrates how the center of the ODMR spectrum shifts to lower frequencies as its ambient temperature increases. Finally, Fig:3-2d shows $I(f; D(T), \left|\vec{B}\right|, \delta\nu, C)$ for two values of $\left|\vec{B}\right|$ and T. Fitting the measured spectra to Equation 3.2 allows the determination of both $\left|\vec{B}\right|$ and $D(T)$.

3.4 Statistical Characterization of NVND Ensembles

In addition to having ODMR spectra that broaden with $\left|\vec{B}\right|$, NVND properties differ for a given fabrication process[197] or surface treatment[100]. Thus, for NVNDs, there exists large variation in their important parameters such as strain, magnetic and thermal sensitivity, and coherence time [197, 164]. This variability of nanodiamond material parameters and orientations has presented challenges for wide-field imaging studies using NVNDs; simultaneous MT imaging at the electronic device level remains limited to date.

Temperature imaging with NVNDs requires extracting T from $D(T)$. Thus, D as a function of temperature needs to be determined. Previous studies have investigated this dependence with limited numbers of NVNDs[151], degrading the precision and accuracy of $D(T)$. In addition, NVNDs can have different $D(T)$, originating from varying nanodiamond impurity concentration, strain, and surface geometry[3, 45]. To determine $D(T)$ we calibrated Q-CAT imaging with known temperatures. Importantly, the wide-field nature of Q-CAT imaging allowed for the investigation of several hundreds of nanodiamonds in parallel - ideal for studying nanodiamond properties. This experiment allowed for determination of the NVND's $D(T)$ distribution.

To excite the NVs across a large FOV, a spin microscope as shown in Chapter 2 was used. A Verdi g2 532 nm single-mode longitudinal laser was focused through a custom microscope onto the back aperture of an objective. The resulting collimated excitation beam was used to pump the NVNDs. Emitted red fluorescence from the NVNDs was collected and measured using an Andor EMCCD camera. A 532 nm notch filter and 650 nm long pass were used to eliminate background fluorescence from the green excitation pump and the neutral charge state of the NV, respectively. The microwave excitation was swept by using a signal generator (Hewlett Packard ESG - D4000A). Collected fluorescence was correlated with microwave frequency in post-processing to determine the NVND ODMR spectra.

To determine D as a function of temperature, we tracked $D(T)$ across 2573 com-

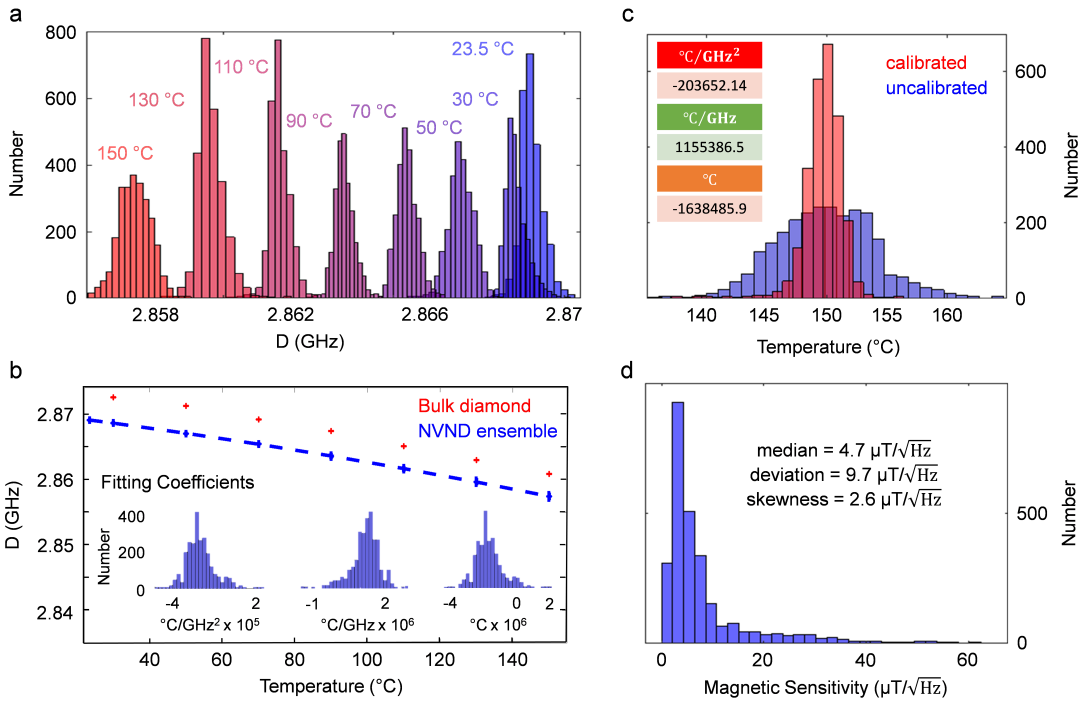

Figure 3-3: **Statistical analysis of NVND properties**. **a**, Histograms of D as a function of T for NVND ensembles. **b**, Fit of the mean value of D vs T. (inset), Histogram of the fit coefficient. **c**, Histogram of the measured temperature across all NVNDs using the average fit coefficients (uncalibrated) and individual fit coefficients for each NVND (calibrated). **d**, Distribution of NVND magnetic sensitivity.

mercially available 100-nm CO-OH terminated nanodiamonds (Adámas Nanotechnologies) from 23.5-150 °C (Fig: 3-3a) using a temperature-controlled stage. The heating stage was supplied by Instec Inc (HCP621 V) rated for a temperature precision of 50 mK. Fig:3-3b shows a second-order polynomial fit of the average NVND $D(T)$ compared with the measured $D(T)$ of bulk diamond NVs. NVNDs' D was lower than bulk diamonds' across all temperatures, which we attribute to the nanodiamond's large strain (E $>$ 5 MHz). Histograms of the distribution of fitting coefficients are within Fig:3-3b inset. We note that the mean measured standard deviation of the NVND thermal response across all temperatures (3.88 °C) was greater than what was expected from measurement error (2.17 °C $\pm$ 0.46°C), indicating that individual NVNDs have varying thermal responses. This variation could result from differences in the thermal resistance at the nanodiamond sample interface, or, as previously theorized[3], inherent variation in NVND thermal response. Fig:3-3c shows the dis-

tribution in the measured temperature using the mean value of the fitting coefficients (Fig:3-3c inset). While individual NVNDs have shot-noise scaling in determining D at a particular temperature, Fig:3-3c demonstrates that the variation in thermal response within the NVND ensemble limits their temperature accuracy for imaging applications.

To compensate for the variation in $D(T)$, we applied the fitting coefficients in Fig: 3-3b inset to each NVND. This individual NVND $D(T)$ calibration improved the mean temperature precision to 2.6 °C per pixel ($\sim$ 1 μm x 1 μm) across all NVNDs, which was within the variation expected from the experimental noise. These results suggest that improving the uniformity of $D(T)$ among NVNDs should be a priority for future nanodiamond fabrication studies. The precision of Q-CAT imaging is comparable to that of alternative thermal imaging techniques such as micro-Raman spectroscopy (1 - 10 °C)[28] and IR (1 - 10 °C) [28].

We also investigated the NVNDs' magnetic field sensitivity (Fig:3-3d) and measured a median of 4.7 $\mu T/\sqrt{Hz}$. We measured a standard deviation of 9.7 $\mu T/\sqrt{Hz}$ and a skewness of 2.6 $\mu T/\sqrt{Hz}$. This distribution contains values ranging from 1.2 to 64.4 $\mu T/\sqrt{Hz}$. This range indicates that future studies on NVND sensitivity need to carefully consider the entire distribution in order to rigorously determine how changes to NVND surface chemistry[133] and fabrication affect performance.

3.5 Sources of Measurement Error

In addition to measurement error (such as shot noise) there are additional sources of systematic error that originate from this model of NVNDs. One source of error originates from simultaneous contributions of E and $\left|\vec{B}\right|$ to the NV's resonant frequencies as shown in Equation 2.2. NVND's strain can vary significantly; thus to individually determine each NVNDs' strain, we require that at least two datasets be taken. As shown in Figure 3-4a, an ODMR spectrum was first measured at ambient magnetic field, B_0. B_0 was determined by using an external gauss meter, and was $\sim$50 μT - 100 μT for all figures shown in the supplemental and main text. The spectrum measured

at B_0 was curve fitted, treating B_0 as a constant, using Equations 2.2 and 3.2 to get the parameters E, $\delta\nu$, C, and D. We used these parameters to determine $\left|\vec{B}\right|$ and T at subsequent measurements. This was shown in the increasing magnetic field values in Fig. 3-4a. Since B_0 was treated as a constant, it affects E, which will affect subsequent measurements of $\left|\vec{B}\right|$. To quantify this impact, we measured the magnetic error as a function of magnetic field for the dataset shown in Figure 3-4a due to the strain measurement, where $B_0 = 0$ μT instead of $B_0 = 100$ μT. The different values of B_0 change the measured strain of the NVNDs. The resulting magnetic error is shown in Fig. 3-4b. The magnetic error decreases as $\left|\vec{B}\right|$ increases. This was because the contribution of E to the NV's resonant frequencies decreases. To determine the

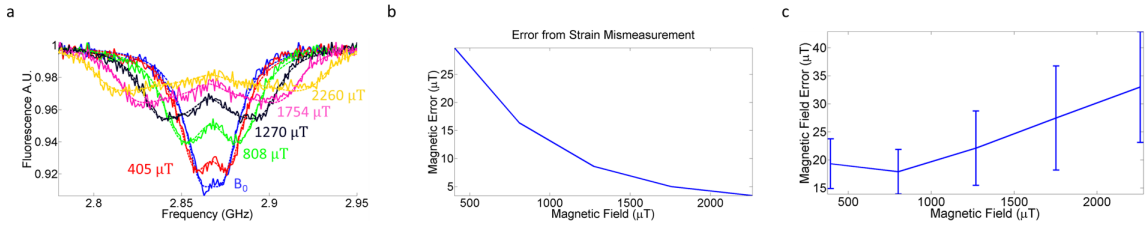

Figure 3-4: **Sources of Measurement Error**. **a**, ODMR spectrum of NVNDs as a function of $\left|\vec{B}\right|$. **b**, Magnetic error from strain mismeasurement as a function of $\left|\vec{B}\right|$. **c**, Experimental magnetic error as a function of $\left|\vec{B}\right|$.

contribution of strain mismeasurement error in relation to experimental noise, in Fig. 3-4c we plotted the mean 95% confidence interval in our magnetic field measurement as a function of magnetic field at the correct B_0. We noted that the error bounds increase as a function of magnetic field. This error results from reduced signal to noise ratio (SNR) of our measurement and the broadening of the observed NV resonance. We saw that the error from strain mismeasurement was smaller than the experimental error.

Another source of measurement error was correlations between changes in $\left|\vec{B}\right|$ and T. In this manner, changes in T may influence measurements of $\left|\vec{B}\right|$ and vice versa. Thus, to measure these correlations we performed the two measurements shown in Fig. 3-5. In Fig. 3-5a we measured the magnetic field while increasing only the temperature. We expected the measured magnetic field to always equal 100 μT

because the magnetic field was constant. In this way, we determined how changes in temperature affected our ability to determine the magnetic field. We saw little deviation in measured magnetic field over a change of 190 °C. Similarly, Fig. 3-5b shows the change in measured temperature when only $\left|\vec{B}\right|$ was increased. We expect no change in the measured temperature as only the applied magnetic field was changing. We see that the measured temperature was close to the measured ambient temperature. The experimental standard deviation across our NVND ensembles (blue curve) was much larger than the 95% confidence interval of our fit, which implied that model error was the dominant noise source in this experiment. From these measurements we see that there was little correlation between measurements of $\left|\vec{B}\right|$ and T.

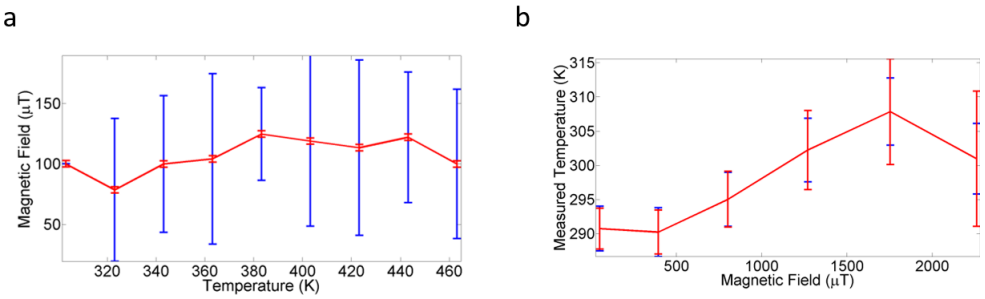

Figure 3-5: **Correlation Measurements**. **a**, $\left|\vec{B}\right|$ as a function of T. **b**, T as a function of $\left|\vec{B}\right|$. For both measurements, the red curve represents theoretical error bounds based on the 95% confidence interval of our fit. Blue curves represent the standard deviation of the measurements.

3.6 Simulating the Effect of NVND Coating on Sample Thermal Profile

The nanodiamond coating layer had negligible effect on the local temperature profile in measurements due to the low thermal conductivity of nanodiamonds. This was simulated using Comsol MultiPhysics. We simulated how the temperature profile of a 100 nm hot spot changed with the application of the nanodiamond coating. A

schematic of our simulation is shown in Fig. 3-6a, where a 100 nm hot spot was maintained at 100 °C. The sides of the block are maintained at ambient temperature. A 1D contour plot at the top surface is shown in Figure 3-6b. The red line is the

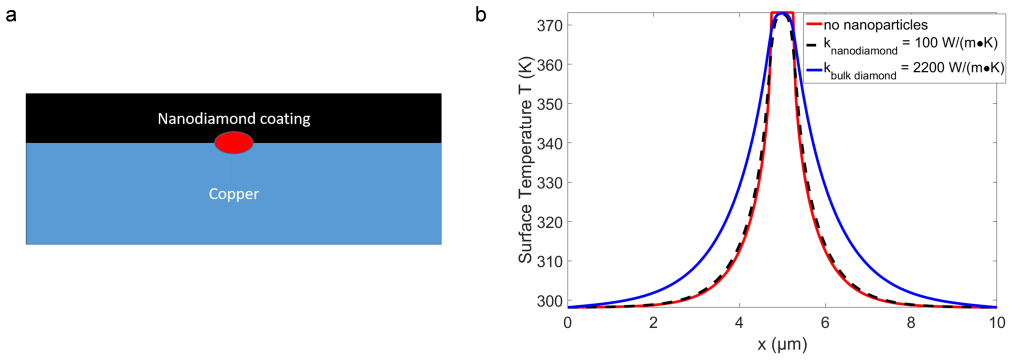

Figure 3-6: **Schematic of Simulated Geometry**. **a**, The nanodiamond coating was treated as a top layer with thermal conductivity $k_{\text{nanodiamond}} = 100\frac{W}{mK}$. The red circle represents the hot spot. **b**, Temperature profile cross-section with different diamond layers.

profile when no nanodiamond coating was applied. The black dashed line represented the situation when a nanodiamond coating with an average thermal conductivity of 100 W/(m*K) [49] was applied. Finally the blue line is the simulated profile when the coating's thermal conductivity matches that of bulk diamond [7]. This case was meant to simulate the effect of layering a thin film diamond membrane for temperature imaging[79]. We saw that a thermal conductivity equal to bulk diamond led to degradation in spatial resolution. However, the nanodiamonds with much lower thermal conductivity, could accurately capture the temperature profile of the hot spot.

To determine the effect that the non-uniform deposition coatings had on the measured thermal profile we simulated the geometry shown in 3-7a. A 100 nm thick bump was placed directly above a hot spot. 3-7b simulated the affect the non-uniformity in nanodiamond thickness had on the measured thermal profile. We saw good agreement between the temperature profiles despite the variation in thickness.

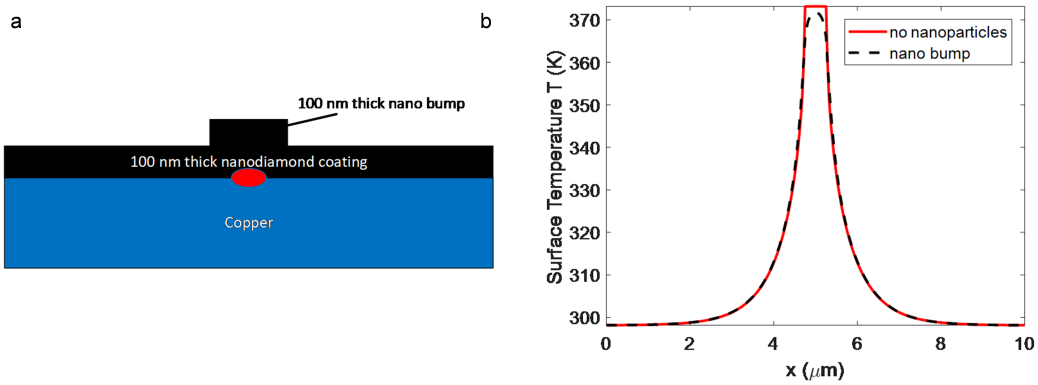

Figure 3-7: **Thermal Profile Cross Section of Non-Uniform Coating.a**,The nanodiamond coating was treated as a top layer with thermal conductivity $k_{\text{nanodiamond}} = 100\frac{W}{mK}$. A 100 nm thick bump was placed directly above the hot spot. **b**, Temperature profile before (red) and after the application of the nanodiamond bump (black dashed).

3.7 Demonstrating Q-CAT Imaging

To demonstrate Q-CAT imaging, we imaged one of the simplest structures that couples electromagnetism and heat transport: a thin gold wire with a narrowed tapered region. Similar structures have been imaged previously[194, 5]. However, this demonstration was the first time NVNDs have been used to conduct wide-field MT imaging. Fig: 3-8a is a false-color scanning electron microscope (SEM) image of the test system. The sample shown in Fig:3-8 was fabricated in MIT's cleanroom facility, the Microsystems Technology Laboratory, using photolithography. We deposited a positive resist (S1813) onto a #1 glass coverslip and spun at 3 krpm for 1 minute. The coverslips were exposed through a mask at 2100 $\mu W/cm^2$ for 40 seconds. Finally, they were developed in CD-26 for 15 seconds while being stirred. Next, a titanium adhesion layer (20 nm) and a gold metallic layer (100 nm, 50 nm respectively) were deposited. After deposition, acetone was used to strip the resist.

Local Joule heating was induced by running electric current (30 mA) through the tapered region (dashed black box). The surrounding metal structure supplies the resonant microwave field, which drove the NV's spin resonances. We deposited NVNDs on top of the structure (thickness $\sim$ 100 nm). The NVNDs are commercially available and are suspended in water. Thus to deposit them, we pipeted solution

containing them onto the surface. This NVND coating solved two issues found with bulk diamond NV thermometry; due to the conformal coating, it has good thermal contact with substrates and avoids heat spreading due to the much lower thermal conductivity of diamond nanoparticles[49, 58]. Both issues limit spatial resolution and artificially reduce peak temperature. An electron multiplying charge coupled device (EMCCD) camera imaged the NVND red fluorescence as shown in Fig: 3-8b. Fig:3-8c-d are images of the magnetic field and temperature of the tapered region, which were measured simultaneously by extracting $\left|\vec{B}\right|$ and D from fits of ODMR spectra measured at each pixel. We determined temperature by converting D using the coefficients presented in Fig: 3-3c inset. These images give insight into how the current flows through the structure, with a high magnetic field region at the structure's edge because the current density increases from both the structure's tapering and magnetic contributions from the side walls. The temperature was 10 °C higher at the kinked region, which indicates that this area is the probable point of failure for the device. Fig:3-8e-f show MT (COMSOL) simulations of the taper region. The measurements and simulations show strong agreement, and we attribute deviations from the simulations to the unknown fluctuations in the structure's surface morphology. This proof-of-concept study shows two significant advantages of the proposed technique. First, the study demonstrates the electric/magnetic current distribution and the associated heating at the wide-field. Second, Q-CAT imaging resolved the microscale temperature distribution on the glass substrate, which has a weak thermoreflectance and Raman signature.

3.8 Q-CAT Imaging of Dynamic Processes

While the previous experiments were conducted at steady state, we also showcase Q-CAT imaging of a dynamic process that is difficult to capture with conventional techniques[28]. Thus, we applied Q-CAT imaging to study electromigration within microstructures. Electromigration is a runaway process[200], which concerns the failure of a conductor due to momentum transfer between the conducting electrons and

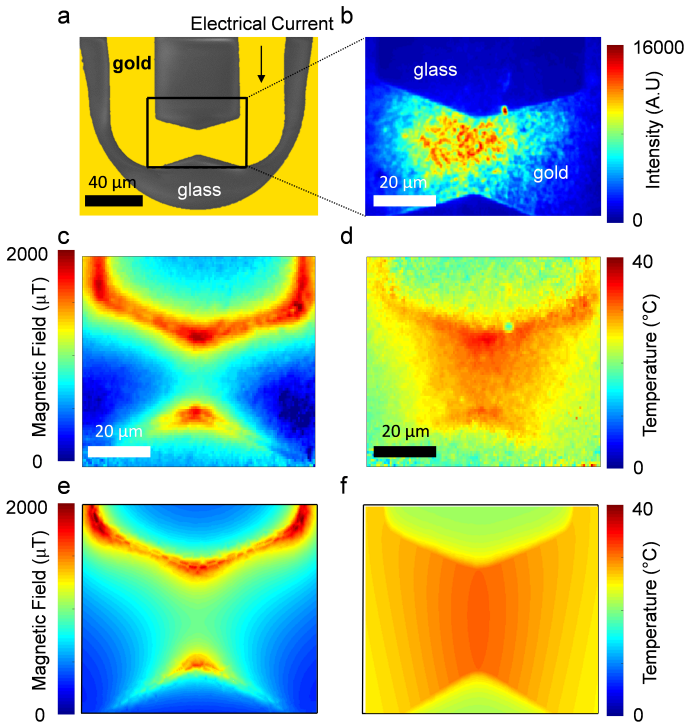

Figure 3-8: **Q-CAT imaging of a microfabricated structure**. **a**, False-color SEM of the microfabricated structure. **b**, Fluorescence image of deposited NVNDs. **c-d**, Magnetic and temperature image of the region-of-interest (ROI) indicated in **a**. **e-f**, MT simulations of the tapered region.

the metal atoms, causing the metal ions to move and create discontinuities[200, 97]. As we will show, a wide-field technique like Q-CAT imaging was well-suited to study this dynamic phenomenon because it allows high frame-rate-MT imaging.

To begin the electromigration process, we increased the current through a similar kinked wire to a constant 35 mA and drove the device to failure. Fig: 3-9a is a fluorescence image of the structure at t = 0 s. Fluorescent areas result from deposited NVNDs. Q-CAT imaging showed that the temperature increased over three distinct time intervals as the wire underwent electromigration (Fig: 3-9b). In the first shaded region, the device was still operating normally, and resistance was constant. In the second shaded interval, the resistance started to linearly increase; in the final region, failure was imminent and the resistance of the wire exponentially increased (Fig: 3-9d). The local temperature increased over time from 50 °C to 220 °C. Within 10 ms of the final image shown in Fig: 3-9b, the wire broke and could no longer support

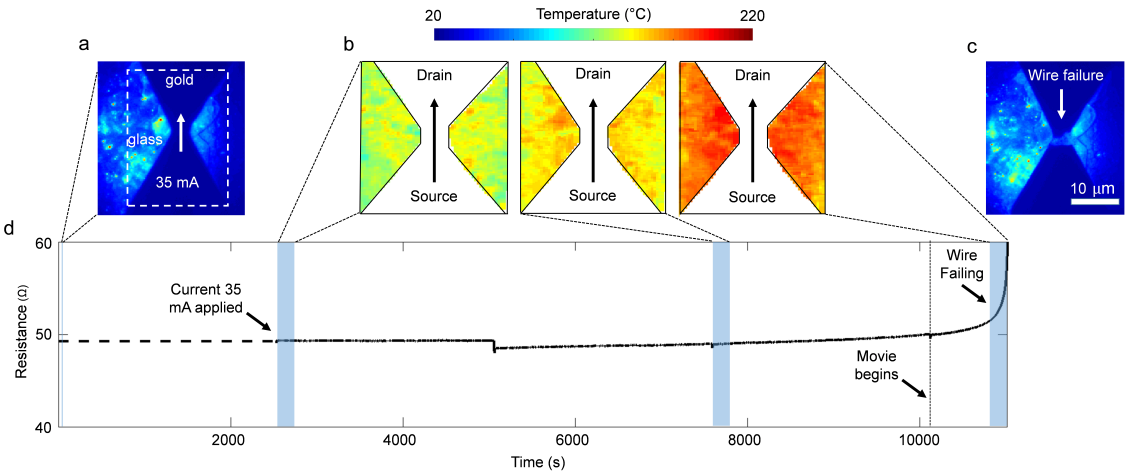

Figure 3-9: **Q-CAT imaging of electromigration**. **a**, Fluorescence image of kinked wire after NVND deposition. **b**, Temperature images of the wire, after 35 mA of current was applied, until wire failure. **c**, Fluorescence image of wire after failure. **d**, Resistance as a function of time. Resistance was determined by dividing the applied voltage by the current. Boxes represent measurement time for each image. The periodic jumps were artifacts that result from the experiment being suspended as the camera buffer was emptied. The dashed line was the extrapolated resistance before current was applied. The attached video's frame rate was artificially increased to shorten video time.

electric current. Fig:3-9c is a fluorescence image of the wire after failure, with a tear at the kink, the location of temperature maximum. The high temperature indicated the location of maximum electric current density and highest electron-gold momentum transfer – the source of electromigration. As expected, due to the constant current of 35 mA, the overall magnetic field distribution did not change over the course of the measurement. This process, beginning at the vertically dashed line, is shown in the attached video, which was sped up for ease of viewing.

The exposure time for each fluorescence image was 10 ms, with a total integration time of 100 ms per microwave frequency, corresponding to a total measurement time for each of the shaded intervals of ∼48 seconds. However, 83% of the measurement time was occupied by camera readout time. In addition, the high count rate of the NVNDs ($<$ 1x10^7 cps) coupled with the small electron well depth of our camera ($<$80,000e$^-$) limited the minimum exposure time. For a camera optimized for bright samples with higher frames per second, the exposure time could be decreased further,

with increased optical pump power. This limitation indicates that a frame rate of 100-1000 Hz is possible if a sparse sampling scheme was adopted and the experimental overhead frame readout time (50 ms) was eliminated using a camera with integrate-while-read capabilities and high frame rates[189]. This frame-rate compares favorably to *in situ* methods such as micro-Raman which requires ∼1 second per pixel. For this reason, it takes more than 1000 s to obtain the temperature distribution of a device with 1000 μm^2 area using micro-Raman thermometry. By contrast, Q-CAT imaging only requires 50 s to measure temperature and magnetic field distributions within the same area, comparable to other wide-field techniques such as IR imaging or thermo-reflectance microscopy. In addition, the transparency of glass limits the SNR of thermo-reflectance microscopy or Micro-Raman thermometry.

3.9 Sparse Sampling

With the model for Q-CAT imaging developed, measured NVND ODMR spectra can be fitted to determine their ambient temperature and magnetic field. This approach requires sampling the full ODMR spectrum at many frequency points to back out these parameters. A measurement technique that allows for the determination of the applied magnetic field from one frequency point allows for a drastically higher imaging rate. Figure 3-10a illustrates how the normalized fluorescence changes as a function of microwave frequency and $\left|\vec{B}\right|$. These changes match what is shown in Figure 3-2. We note in Figure 3-10a the greatest change in normalized fluorescence was located at D (black dashed line). This is in contrast to bulk diamond, where the point of greatest sensitivity is located at $f = \frac{\delta\nu}{2\sqrt{3}}$. In Figure 3-10b we low pass the normalized fluorescence at D and plot it as a function of $\left|\vec{B}\right|$ (blue curve). We fit this curve to a polynomial (red curve). We can use the inverse of this polynomial fitting to measure a changing magnetic field at >1 Hz. Figure 3-10c shows the measured $\left|\vec{B}\right|$ vs. applied magnetic field using this method. This mapping also gives us information on the sensitivity of our nanodiamonds across our FOV. We determined the sensitivity by using the maximum first derivative of the fitted polynomial for each NVND. We

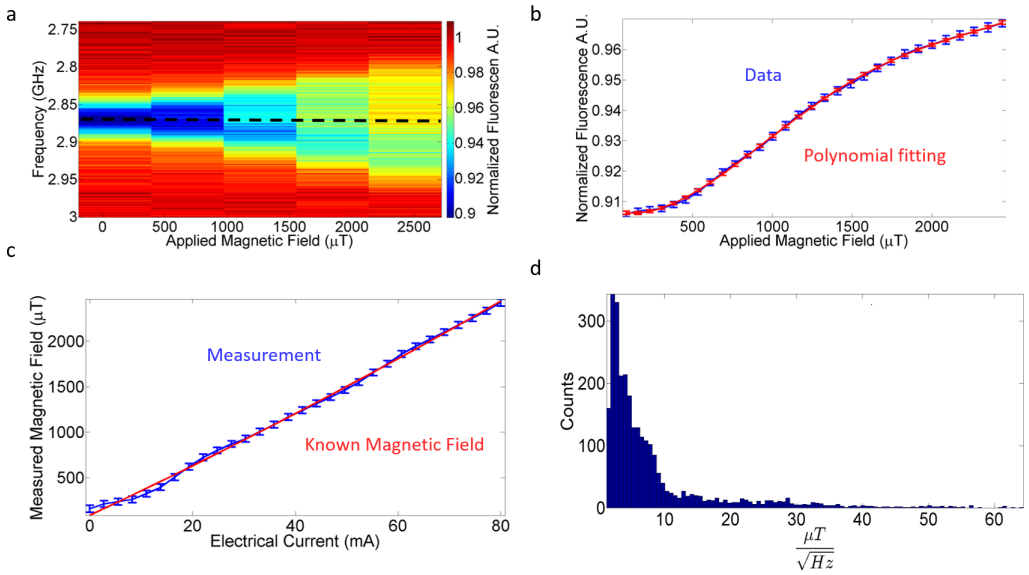

Figure 3-10: **Sparse Sampling Protocol**. **a**, NVND ODMR spectrum as a function of f and $\left|\vec{B}\right|$. The black dashed line was the frequency that **b** was measured at. **b**, Measured C as a function of $\left|\vec{B}\right|$ with polynomial fit. **c**, Comparison between measured $\left|\vec{B}\right|$ and applied $\left|\vec{B}\right|$ using sparse sampling protocol. **d**, Histogram of NVND magnetic sensitivity.

define sensitivity as

$$\nu = \frac{\alpha}{\beta}\sqrt{\delta T} \tag{3.3}$$

where α is the measured standard deviation in the normalized fluorescence, β is the slope of Figure 3-10c, and δT is the total measurement time. A histogram of measured sensitivity is shown in Figure 3-10d. The median was 4.7 $\mu\text{T}/\sqrt{\text{Hz}}$, and these results are comparable to measurements on other similar nanodiamond systems and heavily implanted bulk diamonds[160].

3.10 Q-CAT imaging of GaN HEMTs

We further expanded Q-CAT imaging beyond proof of principle experiments. We imaged a technologically important problem where the interplay between temperature and electric currents is crucial and Q-CAT's wide-field MT imaging capability

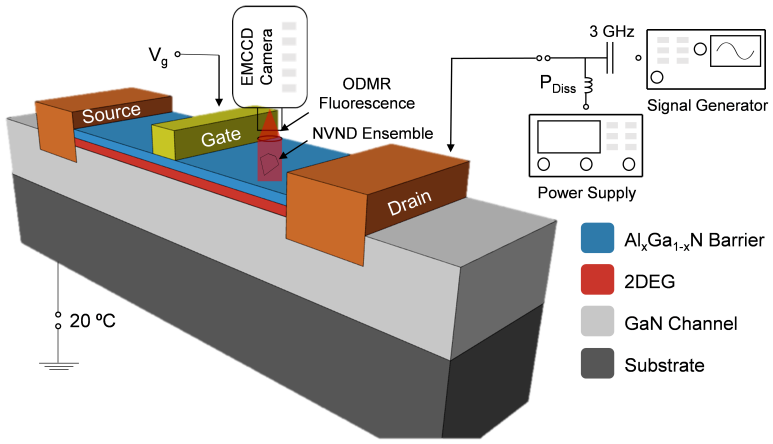

Figure 3-11: **Q-CAT Imaging Schematic for a GaN HEMT**.

is essential - GaN HEMTs. GaN HEMTs are field-effect transistors which incorporate a junction between two materials with different band gaps. They are increasingly used in applications ranging from radio frequency amplifiers[220] to high power electronics[37]. The extremely high power density ($>$ 5 W/mm) in GaN HEMTs gives rise to a concentrated ($\sim$1 μm) channel temperature ($>$200 °C), which leads to device failure[11, 106, 163, 107]. The operation of GaN HEMTs involves non-linear coupling between electromagnetism and heat transport, making their dynamics difficult to capture by simulation, especially when considering device variations. The problem is particularly challenging for the complex geometries of commercial, multi-finger GaN HEMTs. We will image GaN's MT environment to both understand how current flows through the device and identify temperature maxima - the likely failure point, whose magnitude is predictive of device lifetime.

Fig:3-11a illustrates a GaN HEMT under Q-CAT imaging. The GaN HEMT was acquired from Wolfspeed/Cree (CGHV1J006D-GP4) and was mounted on a custom printed circuit board (PCB). Gate and drain voltages were controlled through programmable power supplies and a bias tee was used to feed in the 3 GHz frequency. A thermoelectric cooler mounted with a liquid cooling stage supplied by Koolance was used to cool the GaN HEMT's backside to 20 °C during operation. The current, carried as a 2D electron gas (2DEG) from drain to source, was modulated by the top gate. Fig.3-11a shows the associated magnetic field for a commercial 6-finger GaN

HEMT superimposed over an SEM of the device. A power of 290 mW was applied across the drain while a gate voltage of -2.5 V (threshold voltage -2.8 V) was applied to keep the device in the ON state. The magnetic field decreases from the base of the drain by $\sim$ 300 μT as the current drops along the channel width, as illustrated by the yellow arrows.

We sought to investigate the area with high magnetic field, the channel stop, and thus we conducted high resolution (50x) MT imaging of that region (Fig.3-11a-d). As expected, the magnetic field on the left side of the channel stop was higher, because the resistance of the GaN channel was much higher than that of the drain. The resulting temperature profile was obtained simultaneously. Significant temperature rise was localized around the gate, which agrees with previous experimental observations [11, 106, 163, 107]. Particularly, attributed to the high spatial resolution and wide-field nature of Q-CAT imaging, a sharp temperature drop was well-resolved at the end of the gate along the channel direction (Fig.3-11b-d), indicating limited leakage current at the channel's end. Fig.3-11e is the peak temperature as a function of dissipated power. We measure a thermal resistance of 73 $\pm$ 0.8 °C/W, which agrees with previous measurements of the same model (75 °C/W)[11]. These results elucidate device physics at a spatial resolution that is competitive with *in situ* methods, at wide-field.

3.11 Nanodiamond Coating

To perform imaging we applied 100 nm COOH nanodiamonds. Each nanodiamond has $\sim$500 NVs. These nanodiamonds were suspended in water. To apply the nanodiamonds to our sample, we sonicated the nanodiamond solution at high power for $\sim$2 hours and then pipeted it onto our surface. After the water dried, we used a SEM to image the deposited nanodiamonds. The deposited nanodiamonds are shown in Figure 3-13a. Note that the black spot was a product of the SEM. Figure 3-13a shows the nanodiamonds aggregating within the water droplet, with Figure 3-13b showing several different nanodiamonds within the droplet in a 1μm x 1μm area. An SEM

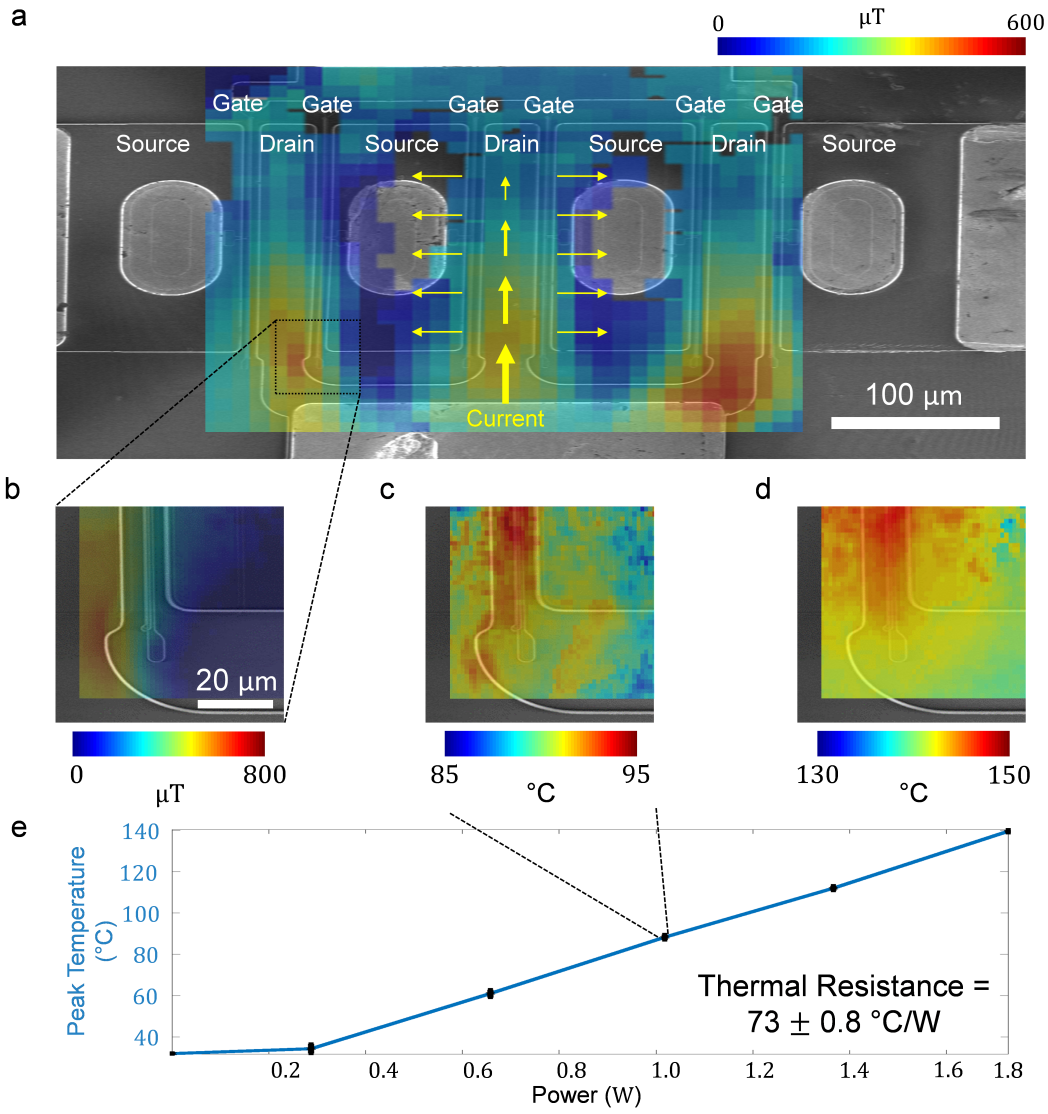

Figure 3-12: **Q-CAT imaging of a multifinger GaN HEMT**. **a**, Magnetic image of a six-finger GaN HEMT in the ON state (4 V, 72 mA). An SEM was superimposed to guide the eye. The magnetic field concentrates at the drain and decreases along the channel width. **b**, High-resolution magnetic field (290 mW) and **c-d**, temperature images of the channel stop (1 W and 1.73 W respectively). **e**, Peak temperature in the ON state as a function of the drain bias. We measure a thermal resistance of 73 ± 0.8 °C/W.

of a microfabricated structure, similar to Fig: 3-8a, is shown in Fig. 3-13c before nanodiamonds are deposited. The structure has a thickness of ∼100 nm. We next looked at the boxed region after nanodiamond deposition in Fig. 3-13d. We note that individual nanodiamonds are not discernible. Instead, there was a coating of

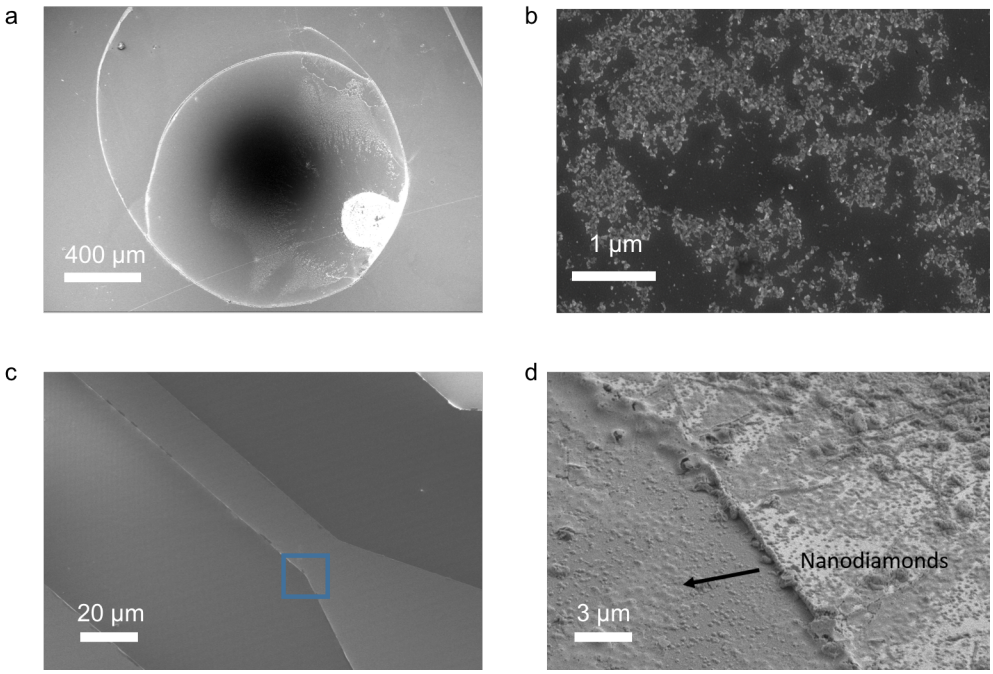

Figure 3-13: **SEM of Deposited Nanodiamonds**. **a**, SEM of deposited nanodiamonds onto a glass slide. **b**, Zoom-in view of deposited nanodiamonds. **c**, SEM of gold microstructure. **d**, Zoom-in of the microstructure after nanodiamond deposition.

nanodiamonds with a mean height of ∼70 nm. We also observe a uniform coating of nanodiamonds across the sample. The heavily aggregated model used in this work was supported by this good evidence.

In Figure 3-14, we show an SEM of an electroplated structure. This structure was ∼15 µm tall. In Fig. 3-14a-b we show the SEM before nanodiamonds were deposited. Fig. 3-14b is a zoom-in of the boxed region. In Figure 3-14c-d, we image the same structure after nanodiamond deposition. We note that the sidewalls of the structure were also coated with nanodiamonds. This coating implies that nanodiamonds can be used to image the magnetic field and temperature of nonplanar geometries. This functionality is especially appealing for certain non-planar systems such as ceramic memories.

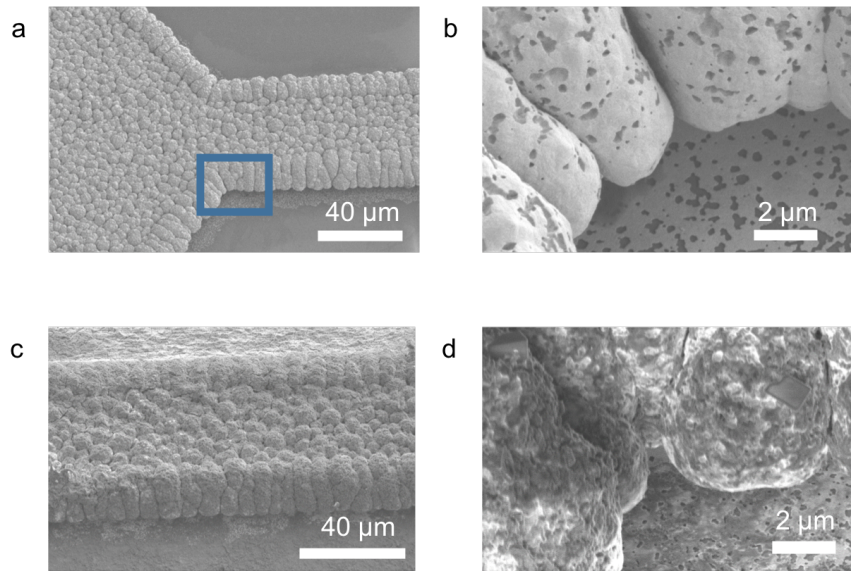

Figure 3-14: **Nanodiamond Deposition on Non-planar Geometries**. **a**, SEM of electroplated structure. **b**, Zoomed-in SEM of boxed region. **c**, SEM of electroplated structure after nanodiamond deposition. **d**, Zoomed-in region after nanodiamond deposition.

3.12 Conclusion

Significant improvements in the sensitivity of Q-CAT imaging are possible. These improvements could be achieved with NVNDs possessing coherence times approaching what has been demonstrated with bulk diamond[14, 197]. Sensitivity could be further extended by using dynamical decoupling pulse sequences[188]. We estimate that mK/$\sqrt{\text{Hz}}$[110] temperature precision and sub nT/$\sqrt{\text{Hz}}$[14] magnetic field sensitivity are achievable with Q-CAT imaging. Q-CAT imaging has further advantages not demonstrated in this work. The unique method of NVND deposition enables the imaging of non-planar geometries. Also, the temporal resolution of this technique could be extended for periodic signals through stroboscopic imaging, in which the laser readout for the NVNDs is pulsed in sync with the application of the electric current. In this manner, a temporal resolution of 10 ns could be achieved, which is limited by the laser gating time. This application could be of interest in studying the transient MT behavior of microelectronic devices, such as the peak temperature of GaN HEMTs at MHz frequencies.

In conclusion, Q-CAT imaging has a number of significant advantages: wide-field measurement with a field of view greater than 100 μm x 100 μm, compatibility with microscopes and almost all materials, and a mean thermal sensitivity comparable to micro-Raman spectroscopy and IR microscopy. Further, while the current implementation offers diffraction limited spatial resolution (< 1 μm), several super-resolution techniques do apply to nanodiamonds and are fully compatible with our demonstration: these include stimulated emission depletion (STED)[9], deterministic emitter switch microscopy[35, 198] and stochastic reconstruction microscopy (STORM)[148].

One possible shortcoming of Q-CAT imaging is that it requires samples that are resilient to microwave fields, which is common for most solid-state devices. In addition, because Q-CAT imaging is an optical measurement, it requires samples with low background red fluorescence ($< 1\text{x}10^6$ cps) under green excitation. We believe that these requirements are not especially restrictive for many active fields of research. Allowing, at a fundamental level, investigation of both steady state and transient thermal transport in a variety of materials systems and characterization of material thermophysical properties. At the device level, Q-CAT imaging helps understand the working principle, life-time and failure mechanisms of devices. These applications are of interest to various fields such as microelectronics, ceramic memories and lithium-ion batteries.

Chapter 4

A CMOS-integrated Quantum Sensor Based on Nitrogen–vacancy Centres

This chapter describes our initial attempts at constructing S^3IC for quantum sensing and control. While Chapter 3 displayed our efforts towards integrated NV-spin systems with microelectronic devices to study their MT environment, this chapter highlights the symbiotic relationship of S^3IC devices. We now showcase how integrated circuits also improve the control of semiconductor spins while enabling a scalable implementation of a quantum-classical control interface. Through tailored CMOS technology, we integrate the essential components for on-chip NV quantum state control and measurement: a microwave inductor, optical color filter, and photodetector, within a submillimeter-scale chip. By driving and detecting the electron spin transitions on the chip (on chip), we demonstrate, for the first time, a chip-scale quantum magnetometry instrument. This work dramatically reduced the instrumentation footprint for quantum magnetometry and thermometry, offering an ultra-compact and scalable platform for quantum sensing.

This chapter begins by integrating NVND ensembles for on chip quantum sensing. We discuss the design of the quantum sensing system and then discuss both the experimental setup and results. We then improve chip performance by integrated NVs within bulk diamond. This improved hybrid diamond-CMOS platform demonstrated ambient quantum vector magnetometry, with a two-fold improvement in sensitivity,

and simultaneous thermometry as well. Much of this chapter is adapted from both Ref. [87] and Ref. [102].

4.1 Introduction

Quantum metrology based on solid-state spins has shown outstanding sensing capabilities for various environmental physical quantities. In particular, the NV center has emerged as a leading room-temperature quantum sensor for temperature[110, 135, 150, 112], strain[142, 190, 198], electric fields[48, 36, 29], and magnetic fields[127, 12, 70, 96, 213, 66, 27] especially to determine atomic species [125, 181, 74, 162, 10, 120, 119, 67]. The advances of NV-based quantum metrology are based on its long spin coherence time[14] and its efficient optical interface for spin polarization and readout. Furthermore, picotesla magnetic field sensitivity at DC under ambient conditions has been achieved[39] by interrogating NV center ensembles.

Conventional approaches for NV magnetometry based on ODMR[188] involve discrete off-the-shelf instruments that limit practical applications and scalability. NV-ODMR requires (i) a microwave signal generator, amplifier, and delivery interface for NV spin manipulation; (ii) an optical filter to reject the pump laser; (iii) a photodetector for NV spin-dependent fluorescence measurements; and (iv) a pump laser. The use in conventional quantum sensing experiments of bulky instruments makes NV magnetometry difficult outside of the lab or within mobile devices. Here, we realize a custom CMOS architecture that addresses these challenges. We integrated requirements (i-iii) directly with a diamond sensor. This architecture stacks the microwave inductor, filter, and photodiode into a 200 μm × 200 μm footprint. This interface is critical to implement large-scale quantum systems for both quantum sensing and information processing[217]. In addition, our approach will open up the possibilities for developing a stand-alone error-corrected quantum system with efficient error decoding and feedback through CMOS logic gates, adding value to both the quantum sensing and quantum information processing communities.

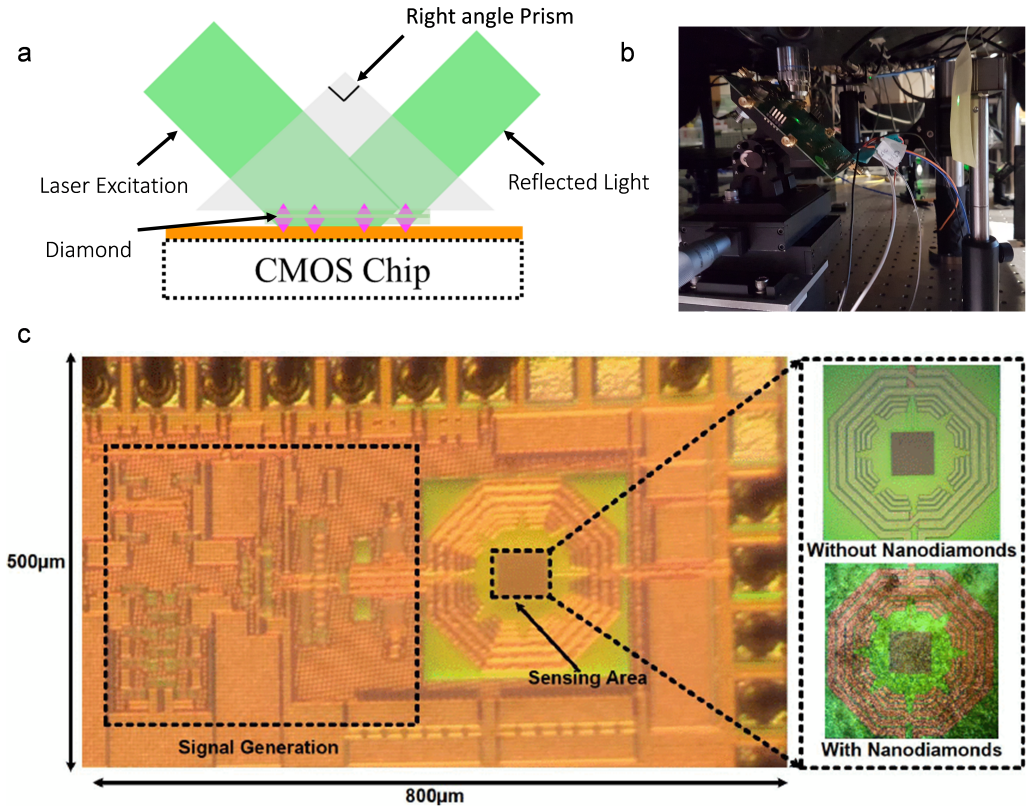

Figure 4-1: **NVND CMOS-integrated quantum sensing architecture.** **a**, A green pump laser excites an NVND ensemble on top of the CMOS chip. A right angle prism improves optical isolation. **b**, Image of optical setup used to perform on chip ODMR. **c**, Bright-field image of CMOS chip with quantum sensing region identified. Microwave fields generated on-chip manipulate NV electron spins through an on chip inductor, leading to ODMR. Inset: Quantum sensing region with and without deposited nanodiamonds.

4.2 Chip-Scale Quantum Sensing with NVND Ensembles

To explore the feasibility of a chip-scale, low-cost quantum magnetometer, a custom-designed CMOS prototype was realized and reported, for the first time, in Ref.[87]. To perform chip-scale quantum sensing, we first designed and fabricated our chip. Our chip was fabricated with a standard 65 nm low-power CMOS technology from TSMC and integrated most of the critical components (except the green light source) for ODMR measurements. The technology provides 1.2 V and 2.5 V MOSFET transistors; the latter with a minimum gate length of 280 nm were used in this work.

The CMOS technology also provides 9 copper interconnect layers, an aluminum pad/redistribution layer, and a top nitride layer for surface passivation. We next deposited NVND ensembles on top of the chip. We decided to perform our first proof-of-principle experiments with NVND ensembles based on our previous experience (Chapter 3) and their easy ability to be deposited onto integrated circuits. To deposit the diamond nanocrystals on the chip, first, the chip passivation layer, which emits unwanted background red fluorescence in our testing, was etched using CF4 plasma. Next, a drop of nanodiamond solution was applied on the treated chip surface; nanodiamonds were then attached to the chip via Van der Waals' forces after drying. Fig:4-1a shows a schematic of this experiment. The pump laser background measured by the photodetector located below the nanodiamonds was reduced by coupling the green beam into a right angle prism. Fig:4-1b shows the optical setup for this experiment and 4-1c is a top view of the CMOS chip with the signal generator, antenna, and sensing region shown. The sensing region with and without nanodiamonds is shown with the inner square being the embedded photodiode, which detected the spin dependent fluorescence. Performing all of these steps allows the CMOS chip to perform ODMR.

NV magnetometry detects external magnetic fields through the Zeeman shift induced on the NV's ground-state sublevels[188]. As described in Chapter 2, an external magnetic field $\vec{B}$ induces an energy shift $\gamma_e B_z$ on the NV ground state spin triplet ($|m_s = 0, \pm 1\rangle$). The spin transition frequencies, $\epsilon_{\pm 1}$, between sublevels $|0\rangle$ and $|\pm 1\rangle$, are given by

$$\epsilon_{\pm 1} = (D - \beta_T \Delta T) \pm \gamma_e B_z, \tag{4.1}$$

where $D = 2.87$ GHz is the room-temperature natural ground-state splitting between sublevels $|0\rangle$ and $|\pm 1\rangle$, γ_e is the electronic gyromagnetic ratio (28 GHz/T), $\beta_T \approx$ 74 kHz/K [3], and ΔT is the temperature shift from room temperature. Measuring $\epsilon_{\pm 1}$ gives B_z and ΔT in their difference and sum, respectively. In addition, measuring B_z for at least three of the four possible NV orientations in diamond quantifies all components of $\vec{B}$ for vector magnetometry[123, 209, 38, 166].

The NV ground state transitions $\epsilon_{\pm 1}$ are measured by ODMR under green laser excitation, as illustrated in Fig:2-2. The spin magnetic sublevel $|0\rangle$ has a bright cycling transition, where it emits red fluorescence. In contrast, the $|\pm 1\rangle$ can undergo an intersystem crossing into a metastable, dark spin-singlet state, from where it decays back into the $|0\rangle$ sublevel. This has two consequences: optical spin polarization into sublevel $|0\rangle$ and lower average fluorescence of the $|\pm 1\rangle$ spin populations. The microwave field moves spin population between $|0\rangle$ and $|\pm 1\rangle$. Sweeping the applied microwave frequency leads to the ODMR spectra shown in Fig:2-2, from which $\epsilon_{\pm 1}$ are determined.

On-Chip microwave Generation and Delivery

In our chip-scale NV magnetometer, the on-chip generated microwave fields drove the ground-state spin transitions. Figure 4-2a shows the circuitry for on-chip microwave generation and delivery. This circuitry was composed of a phase-locked loop (PLL), a current driver, and a resonant loop inductor. The PLL generated the microwave sweep signal from 2.6 GHz to 3.1 GHz required for ODMR. The main component of this loop was an on-chip voltage-controlled ring oscillator (VCO) with 3 differential inverter stages. Using a ring VCO[158] avoided large inductors and minimizes the cross-talk between the oscillator and the microwave inductor which drives the NV ensemble. The mutual-locking inverter pair (e.g., INV_2 in Fig:4-2a) formed a latch and ensured the differential phases between the left and right branches of the VCO. The frequency tunability of the oscillator was realized via 3 pairs of MOS variable capacitors (e.g. C_{VCO} in Fig:4-2a), of which the capacitance changed from 22 fF to 75 fF when the PLL control voltage V_{ctrl} varied from 0 to 5 V. The CMOS chip was wire-bonded to a PCB board. An off-chip synthesizer circuit (AD9525 by Analog Devices) provided a charge pump, a phase/frequency detector, and a frequency divider. It combined with the internal ring VCO to form a phased-locked loop.

The VCO output signal was frequency-divided by 24 and then compared to a 120 MHz reference signal provided by an external signal source (HP ESG-D4000A). The

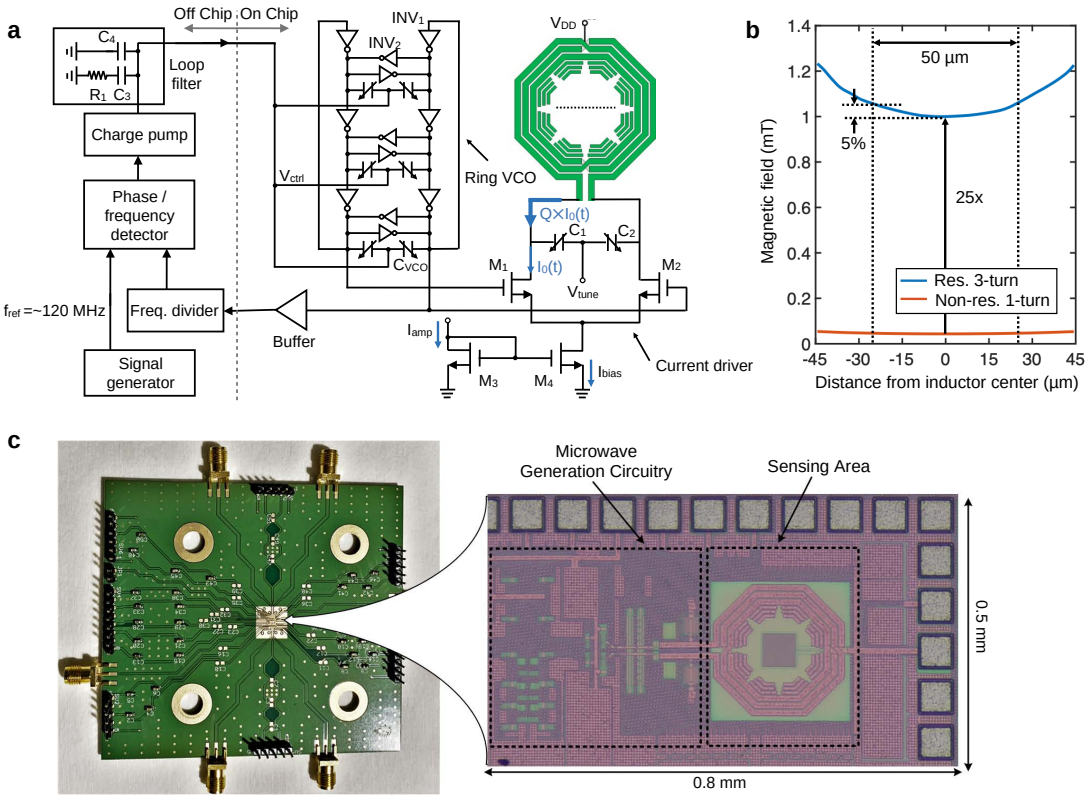

Figure 4-2: **On-chip CMOS microwave generation and inductor characteristics. a**, Schematic of microwave generation circuitry. **b**, High-frequency electromagnetic fields simulations (HFFS) for the on-chip inductor. Magnetic field amplitude is plotted as a function of distance from the inductor center (dashed line in **a**). The resonant multi-turn loop inductor (blue) produces 25× higher amplitude than the nonresonant single turn inductor (red) at the same DC current. The insertion of the parasitic capacitive loops yields a microwave uniformity of 95% over 50 µm. **c**, Optical micrograph of the CMOS chip (right) and photo of the printed circuit board for testing (left).

loop filter of the PLL was a typical second-order low-pass filter. The values of the components shown in Fig:4-2a were R_1=0.4 kΩ, C_3=4.5 nF and C_4=150 pF. The entire phase-locked loop was closed with off-chip components to enhance the stability and decrease the phase noise of the signal.

The microwave fields were delivered to the NV ensemble through the loop inductor (Fig:4-2a) implemented on the top-most copper layer (Metal 9) with a thickness of 3.4 µm. To efficiently deliver the microwave field, the loop inductor and a pair of shunt capacitors (C_1 and C_2 in Fig:4-2a) formed a resonating load for the current driver.

C_1 and C_2 were MOS variable capacitors with capacitance ranging from 312 fF to 1.4 pF. By electrically tuning them via V_{tune}, the load resonated near D. This current driver, fed by the output of the ring VCO, produced oscillating current in the inductor at the VCO microwave frequency. To improve the performance of this inductor for advanced NV sensing protocols[44], we needed to increase the applied microwave field amplitude. The amplitude is enhanced by a factor Q of the driver DC bias current ($I_{\text{bias}} \approx 5$ mA from a 2.5 V power supply), where Q (~ 15) is the quality factor of the inductor. In addition, we used a three-turn loop to multiply the microwave field strength. Overall, we had 25× enhanced microwave field strength compared to a non-resonant single turn loop (as plotted in Fig:4-2b). With an outer diameter of 236 μm, the loop exhibits an inductance of ∼3 nH. In addition, the aforementioned sensing protocols also require highly uniform microwave fields over the excitation volume. To achieve this, three capacitive parasitic loops were inserted[87]. We tailored the radius of these loops, so that their opposite induced field homogenizes the overall generated field. Another degree of freedom is the capacitive gaps in the parasitic loops. This controlled the amount of current flowing in these loops. Therefore, we optimized these two parameters (i.e. the parasitic loop radius and the capacitive gap) for the three parasitic loops to achieve $> 95\%$ uniformity. The spectral purity (phase noise) of the microwave was 90 dBc/Hz at an offset frequency of 1.5 kHz.

4.3 On-chip Optical Filtering of Green Pump Laser

Plasmonic filters based on a multi-stacked-layer gratings in the back end of line (BEOL) of CMOS technologies have been demonstrated previously in [80, 87]. In our first CMOS quantum sensor[87], a single-layer filter based on the same principle of wavelength-dependent plasmonic loss was adopted. The NV spin transitions were detected using an on-chip photodetector. A CMOS-compatible periodic metal-dielectric structure (Fig:4-3) in the Metal 8 interconnect layer filtered the green pump light. Specifically, incident light coupled to the surface plasmon polariton (SPP) at the metal-dielectric interface, where green light rapidly decays due to frequency-

dependent Ohmic loss[221, 80].

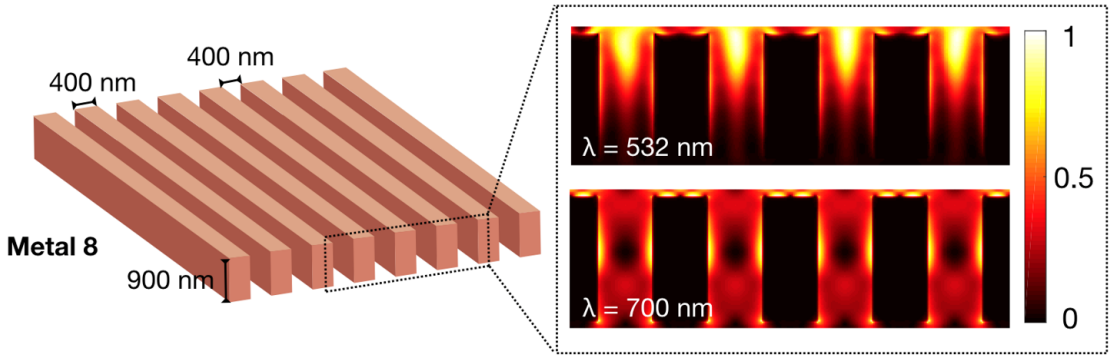

Figure 4-3: **Schematic of on chip Plasmonic Filter. a**, CMOS-compatible optical pump beam filter implemented using a single-layer plasmonic grating filter implemented on Metal 8[87]. The periodic metal-dielectric grating absorbs the green laser. Inset plots finite-difference-time-domain (FDTD) calculation of the optical intensity map inside the structure for green (top) and red light (bottom). Incident light polarization is perpendicular to the grating line.

Figure 4-3 shows the structure of the filter used in [87, 102]. Each slit is considered as a parallel plate waveguide transmitting light inside a dielectric (relative permittivity $\epsilon_d \approx 1.5$) in the z- direction. The incoming light was modeled as a plane wave with a transverse electrical field E_x and a propagation constant $k_0 = \omega\sqrt{\epsilon_d}/c$ (c is the speed of light in vacuum). This light was coupled to the TEM mode of the parallel-plate waveguides, which has identical propagation constant k_0. As the propagating wave interacted with the metal, the surface plasmon polariton (SPP) mode at the metal-dielectric interface is excited. Note that the dispersion relation of SPP mode is:

$$k_{z,\mathrm{SPP}} = \beta_{\mathrm{SPP}} + j\alpha_{\mathrm{SPP}} = k_0\sqrt{\frac{\epsilon_m}{\epsilon_m + \epsilon_d}}. \tag{4.2}$$

Where the permittivity ($\epsilon_m = \epsilon_{\mathrm{mr}} + j\epsilon_{\mathrm{mi}}$) of the metal (copper in our case) has a negative real part, which leads to $\beta_{\mathrm{SPP}} > k_0$. Although coupling from the TEM waveguide mode and the SPP mode generally does not occur,[1] it still does in this case. That is

[1]Normally, dedicated material/geometrical configurations, such as the Otto and Kretschmann-Raether configurations, are needed to enable the excitation of the SPP mode.

because, by examining the value of β_{SPP} in (4.2):

$$\beta_{\mathrm{SPP}} = \mathrm{Re}(k_0\sqrt{\frac{\epsilon_m}{\epsilon_m+\epsilon_d}}) \approx k_0(1-\frac{\epsilon_d}{2\epsilon_{\mathrm{mr}}}), \tag{4.3}$$

we see that since $|\epsilon_{\mathrm{mr}}|$ remains large, the relative mismatch between the β_{SPP} and β_{TEM}=k_0, namely $\epsilon_d/2\epsilon_{\mathrm{mr}}$ in (4.3), are ∼0.07 for red (700 nm) and ∼0.2 for green (530 nm). These calculations were based on the Drude-Brendel-Bormann model [156, 75]. Along the vertical propagation distance of the grating (i.e. the M8 grating thickness d=900 nm, or $2\lambda_{\mathrm{red}}$=$2.5\lambda_{\mathrm{green}}$ in dielectric), the accumulated phase mismatch is:

$$\Delta\phi = 2\pi\frac{\epsilon_d}{2\epsilon_{\mathrm{mr}}}\frac{d}{\lambda}, \tag{4.4}$$

or ∼50^o (red) and ∼180^o (green), respectively. Therefore, for red light, constructive coupling from the TEM mode to SPP mode still occurs within the single-layer grating. For green light, although phase mismatch appears to be large, the coupling is still effective in the M8 slit due to the large SPP loss; and when the TEM wave reaches the bottom half of the slit, its power is already heavily depleted. To quantify the loss of the SPP mode, we derive the attenuation factor α_{SPP} in (4.2):

$$\alpha_{\mathrm{SPP}} = \mathrm{Im}(k_0\sqrt{\frac{\epsilon_m}{\epsilon_m+\epsilon_d}}) \approx k_0\frac{\epsilon_d\epsilon_{\mathrm{mi}}}{2\epsilon_{\mathrm{mr}}^2}, \tag{4.5}$$

α_{SPP} exhibits large difference between red (≈$0.01k_0$) and green (≈$0.26k_0$) as calculated based also on the Drude-Brendel-Bormann model.

These effect culminate in the simulated performance of the plasmonic filter. Fig:4-3 inset plots the intensity map for the green (λ = 532 nm, Top) and red light (λ = 700 nm, Bottom), showing the ∼ 95 % and ∼ 5 % absorption for green and red light through the structure, respectively. For a total green-to-red rejection ratio of ∼10 dB in our experiment. The performance of the filter as a function of wavelength was simulated using a FDTD solver, Lumerical, and is shown in Fig:4-4.The typical NV spectrum is superimposed for context.

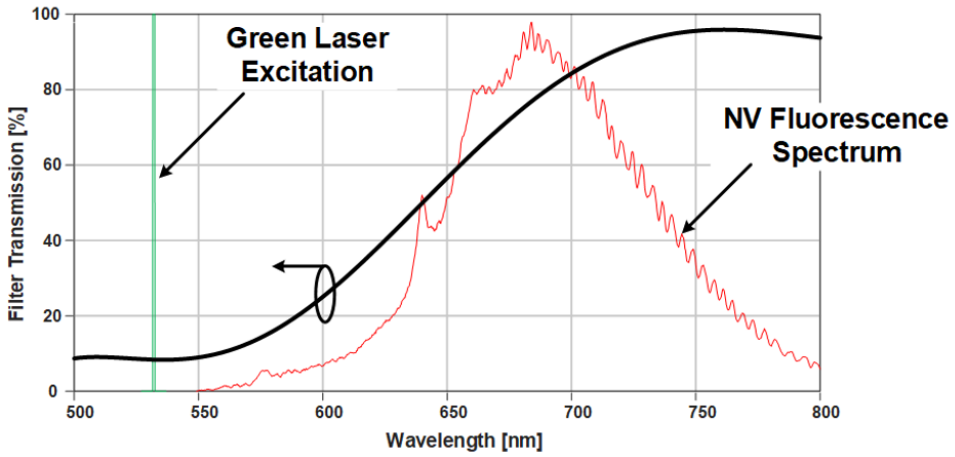

Figure 4-4: Simulated transmission values through the filter as a function of wavelength. The typical NV spectrum is superimposed for context.

4.4 On-chip Spin Readout

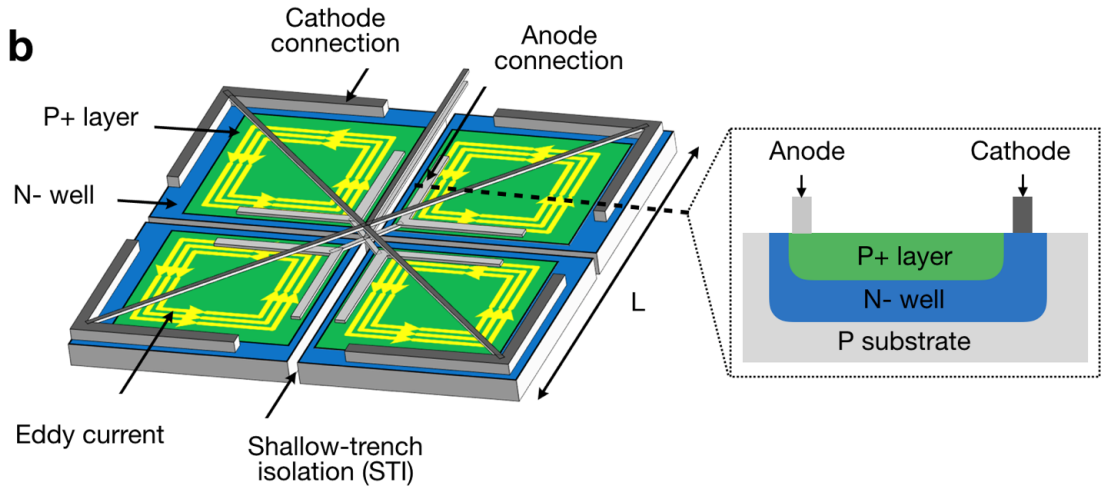

Figure 4-5: **On Chip Photodiode** Photodiode geometry: photodiode area is divided into four sub areas, separated by a shallow trench isolation, to reduce eddy current (yellow loops) losses. Inset: cross-section along dashed line.

The photodiode consists of a P+/N-well/P-sub junction shown in Fig:4-5 which is preferable for long wavelength detection[131]. Since we placed the photodiode with its conductive layers below the inductor (Fig:4-2a), large eddy currents near 2.87 GHz can be induced. This reduces the quality factor of the inductor, resulting in microwave amplitude reduction. We reduced this eddy current by half, by dividing

the photodiode area into four sub areas as shown in Fig:4-5b. Furthermore, the anode/cathode connectors were arranged in a similar way to patterned ground shielding used in CMOS inductors[219]. This arrangement avoids any closed loops, which helps to cut the eddy current that may flow in the metallic connections. The photodiode has a measured responsivity of 0.23 A/W at the wavelength of 532 nm (corresponding to a quantum efficiency of 0.54), and a noise-equivalent-power of $\sim 4.9 \pm 2.6$ nW/$\sqrt{\text{Hz}}$ at 1.5 kHz.

To estimate the reduction in noise for this geometry we analyzed the effect of eddy currents for this geometry. For a square photodiode with a side length of L, the eddy current power P_{eddy} is quadratically proportional to the change of the magnetic flux $d\phi(t)/dt$:

$$P_{\text{eddy}} \propto \frac{(d\phi(t)/dt)^2}{R} \propto \frac{L^4 \left(\frac{dB}{dt}\right)^2}{L} \propto L^3 \left(\frac{dB}{dt}\right)^2.$$

Here, t is the time; R is the resistance; and B is the magnetic field generated by the loop inductor in Metal 9. By dividing the photodiode active area into N by N sub areas, the eddy current is reduced by $N^2 \times (L/N)^3/L^3 = 1/N$.

4.5 On chip ODMR with NVND Ensembles

To characterize the chip performance we first performed wide-field CW-ODMR similar to what was demonstrated in Chapter 3. Fig:4-6a is a schematic of the experimental setup. A linearly polarized DPSS green laser beam (500 mW, $\lambda = 532$ nm, Verdi G2, Coherent) is delivered to the diamond through a telescope of $f_1 = 35$ mm and $f_2 = 150$ mm. The beam diameter incident on the diamond is $\sim$500 μm. A half-wave plate rotates the polarization of the laser beam to maximize the laser absorption through the periodic metal/dielectric structure in the Metal 8 layer. The resulting collimated light was used to excited the deposited NVND ensemble. The emitted ODMR fluorescence was then collected and imaged on to an external camera. Simultaneously, the on-chip generated microwave frequency was swept while the images were acquired. We saw a drop in fluorescence at $D = 2.87$ GHz. To confirm that

the observed resonance resulted from the deposited NVNDs, we applied $\left|\vec{B}\right| = 17.2$ G. We observed a broadening of the ODMR spectrum as expected from Chapter 3. We observed a contrast of 10%. The large linewidth we observed is due to the power broadening of the NV transition[50] due to the large MW field amplitude from our unique MW inductor geometry.

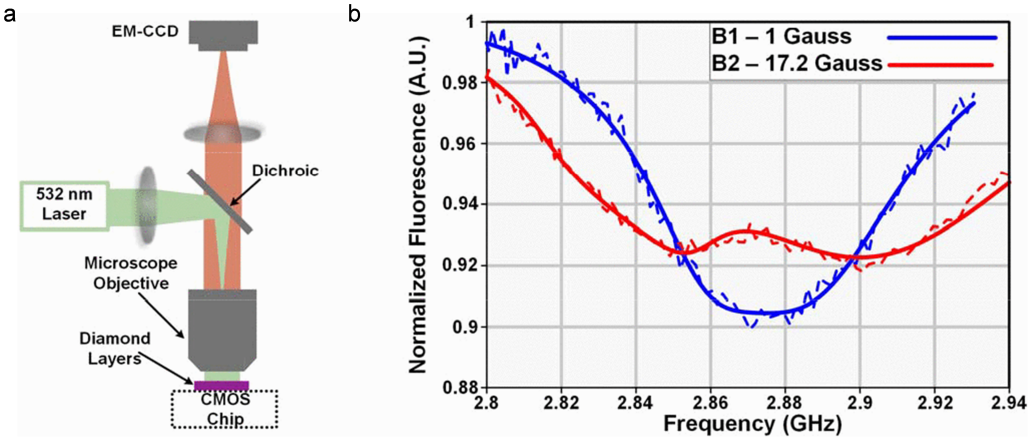

Figure 4-6: **Off Chip Optical detection of NV spin-dependent fluorescence.** **a**, Schematic of experimental setup. **b**, Measured NVND ODMR spectra at $\left|\vec{B}\right| = 1$ G (blue) and $\left|\vec{B}\right| = 17.2$ G.

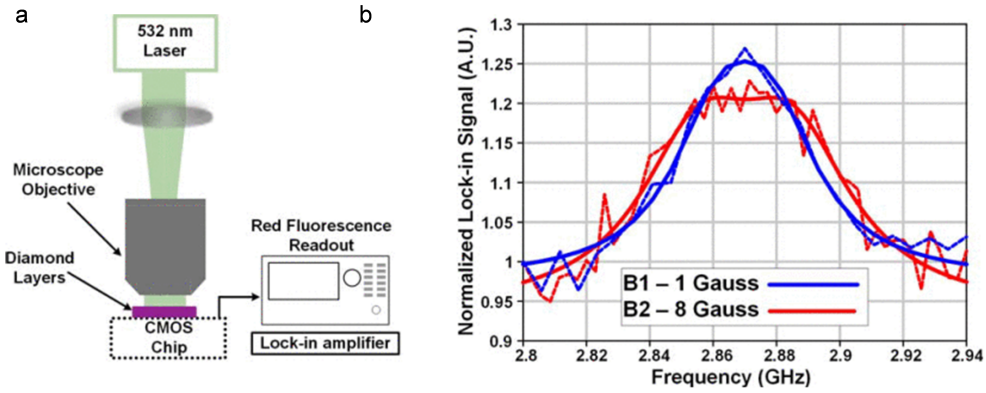

Figure 4-7: **On Chip Optical detection of NV spin-dependent fluorescence.** **a**, Schematic of experimental setup. **b**, Measured NVND ODMR spectra at $\left|\vec{B}\right| = 1$ G (blue) and $\left|\vec{B}\right| = 8$ G.

To measure the ODMR fluorescence on chip, we used an experimental schematic similar to Fig:4-7a. Where a green laser was focused on to the back aperture of an ob-

jective and used to excite the deposited nanodiamonds. The emitted fluorescence was detected using the on chip photodiode. To increase SNR, the microwave signal used to drive the NV centers was AM modulated (fm=1kHz). Most of the fluorescence-induced current was rejected with only the component caused by $\epsilon_{\pm}$ spins with a frequency at fm were detected. This current component was then measured by a lock-in amplifier and generated the ODMR spectrum seen in Fig:4-7b. Similar to Fig:4-6b, when an external static magnetic field was applied, the Zeeman effect was observed. Since the crystal orientation of nanodiamonds are random, we observed spectral broadening, rather than splitting. We measured a sensitivity of 73 $\mu T/\sqrt{Hz}$.

4.6 On chip ODMR with NV Center in Bulk Diamond

While NVND ensembles were excellent for the initial proof-of-principle demonstrations, the lack of resolvable resonances presented the following problems:(i) they limited sensitivity by increasing $\delta\nu$, (ii) they prevented first-order canceling of temperature induced noise[39, 102], (iii) as scalar magnetometers[58] they prohibited vector magnetometry[166, 89], and (iv) they did not allow advanced dynamical decoupling pulse protocols which can enhance the sensitivity by orders of magnitude or more[16]. Thus, we next integrated buld diamond with our CMOS chip.

Figure 4-8 illustrates this new device for on-chip ODMR. We first prepared the diamond for experiments. To avoid the direct injection of the green laser pump beam into the CMOS, we cut the CVD-grown diamond single crystal (supplied by Element 6) as shown in Fig:4-8a, A 45° cut in the corner of the diamond directed the off-chip green pump beam along the length of the diamond slab and avoided the direct injection of the green laser pump beam into the CMOS. This excitation geometry reduced the pump laser background into the photodetector located below the diamond. The diamond was irradiated by an electron beam with a dosage of 10^{18} e^{-} cm^{-2} at 1 MeV. Then, the diamond was annealed for 2 hours at 850° Celsius

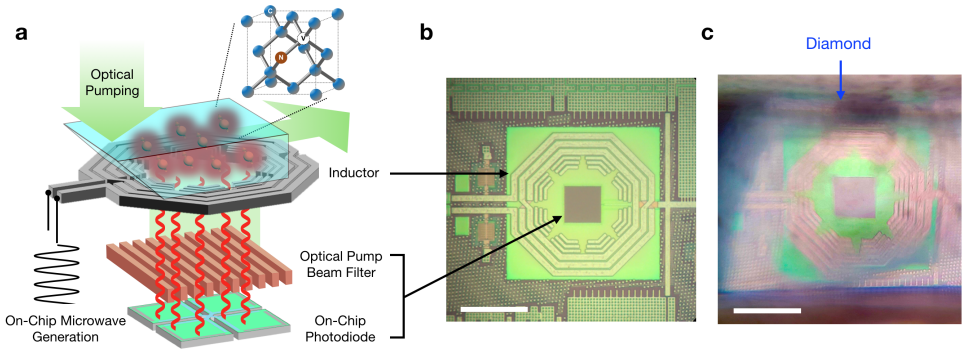

Figure 4-8: **CMOS-integrated quantum sensing architecture. a**, A green pump laser excited NV ensembles in the diamond slab. Microwave fields generated on-chip manipulate NV electron spins through an on-chip inductor, leading to ODMR. A metal/dielectric grating absorbs the green pump beam and transmits the NV spin-dependent fluorescence to the on-chip photodiode. Inset: NV atomic structure. Top-view micrograph of the fabricated CMOS chip without (**b**) and with (**c**) the diamond slab. Scale bar is 200 μm.

and then subsequently picked and placed onto the CMOS chip under a microscope. This irradiation and annealing produced NV centers at a density of $\sim$ 0.01 ppm. Immersion oil fills the diamond-CMOS interface to adhere the diamond slab. This also minimizes the fluorescence loss by reducing the refractive index difference. The on chip microwave generator and inductor drove the NV electron spin transitions.

We detected NV-ODMR with a lock-in technique. The green laser beam continuously excited the NV ensemble, and the frequency-modulated (FM) microwave fields (f_m = 1.5 kHz and modulation depth of 6 MHz) drove the NV electron spin transition. The spin-dependent fluorescence produced photo-current within the on-chip photodiode (Fig:4-5b). Then, we read out the modulated photo-current with the voltage drop across a 50 Ω resistor at f_m with one second integration time, which corresponded to an equivalent noise bandwidth of 0.078 Hz (considering the filter roll-off of 24 dB/oct) with a Stanford Research Systems lock-in amplifier (SR865A). The use of the lock-in amplifier rejects the DC current offset of the photodiode, which was caused by the unmodulated green laser, and avoids the low-frequency flicker noise accordingly.

Figure 4-9a shows the lock-in signal for the ODMR experiment under zero applied external magnetic field. This spectrum corresponds to the derivative of the ODMR

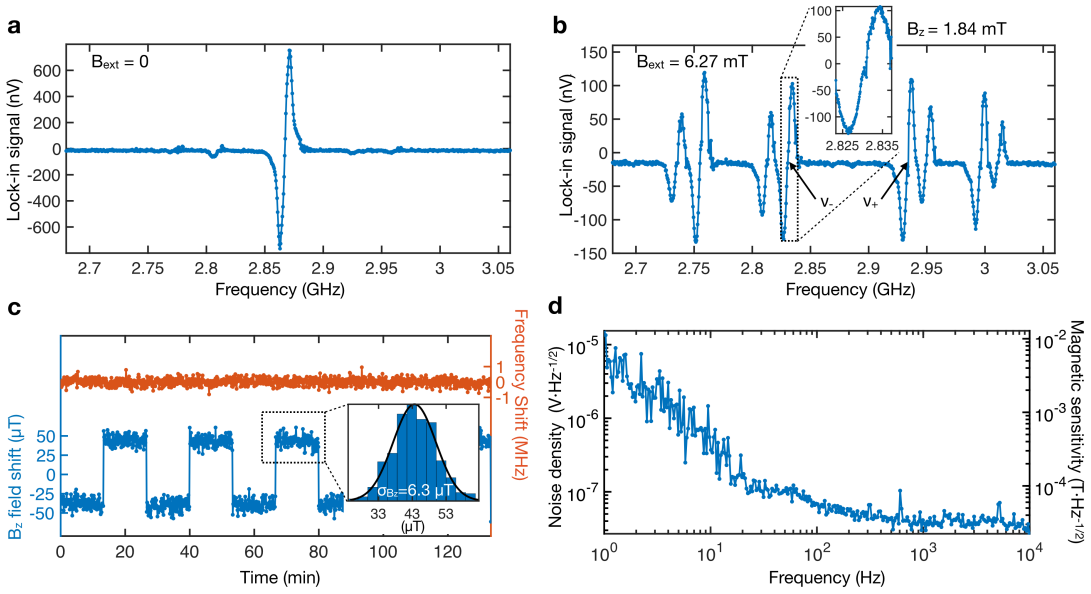

Figure 4-9: **On-chip detection of ODMR and NV-based quantum magnetometry.** **a**, Frequency-modulated (FM) lock-in signal of NV spin-dependent fluorescence at zero external magnetic field (in addition to $B \sim 100$ μT of the earth magnetic field). **b**, FM lock-in signal with a permanent magnet ($B = 6.27$ mT): B_z was the magnetic field along the NV-axis with the spin transition at $\epsilon_{\pm}$. The linewidth of the ODMR was 7 MHz. Slopes dV/df at $\epsilon_- = 2.8303$ GHz and $\epsilon_+ = 2.9330$ GHz were 42.969 nV/MHz and 42.450 nV/MHz, respectively.**c**, On-chip magnetometry (Blue) and temperature effect (Red) separation: lock-in signals at both $\epsilon_{\pm 1}$ were observed while switching the polarity of external electromagnet with a period of 26 min. Inset plots the histogram of measured magnetic field B_z with a standard deviation of 6.3 μT. This uncertainty corresponds to a magnetic field sensitivity of 32.1 $\mu T/\sqrt{Hz}$. After calibration of β_T, the plotted center frequency (red) could be converted to a temperature. Measurements were conducted with a time constant of 1 second. **d**, Noise spectral density monitored at ϵ_-.

spectrum shown in Fig:2-2. Next, we aligned a permanent magnet (6.27 mT) to split the spin transitions of the four NV orientations. Figure 4-9b shows the ODMR spectrum, which exhibits the expected eight spin transitions. The use of the corresponding four NV ensembles enables vector magnetometry. In particular, we noted the spin transitions at $\epsilon_- = 2.8303$ GHz and $\epsilon_+ = 2.9330$ GHz of the NV ensemble.

Monitoring the lock-in signal V at ϵ_- and ϵ_+ allows independent measurements of magnetic field and temperature, as described above. Specifically, the sum of the lock-in signal change ΔV at $\epsilon_{\pm 1}$ is proportional to ΔT, while the difference provides

ΔB_z:

$$\Delta T = \frac{1}{2\beta_T}\left(\left.\frac{\Delta V}{dV/df}\right|_{\epsilon_+} + \left.\frac{\Delta V}{dV/df}\right|_{\epsilon_-}\right) \tag{4.6}$$

and

$$\Delta B_z = \frac{1}{2\gamma_e}\left(\left.\frac{\Delta V}{dV/df}\right|_{\epsilon_+} - \left.\frac{\Delta V}{dV/df}\right|_{\epsilon_-}\right). \tag{4.7}$$

Figure 4-9c plots the detected ΔB_z induced by an electromagnet (blue) and measured center frequency shift (red). The plotted center frequency could be converted to a temperature after β_T calibration.

The magnetic field sensitivity is given by the following relation:

$$S = \frac{\sigma_{B_z}}{\sqrt{\text{ENBW}}}. \tag{4.8}$$

Here, σ_{B_z} was the noise in ΔB_z measurement, and ENBW is the equivalent noise bandwidth of the lock-in detector. In our measurement, ENBW $= 5/(64\tau)$ with a time constant τ of 1 second, accounting for the 24 dB/oct of the lock-in amplifier filter roll-off. By measuring σ_{B_z} of 6.3 μT from the modulated spin-dependent fluorescence (Inset in Fig:4-9c), we determined our DC magnetic field sensitivity of 32.1 $\mu\text{T}/\sqrt{\text{Hz}}$ that includes additional $\sqrt{2}$ factor of ϵ_+ and ϵ_- signal average. This DC magnetic field sensitivity was limited by the noise detected in the ENBW at $f_m = 1.5$ kHz. Figure 4-9d plots the noise spectral density measured at ϵ_- (no temperature compensation) using the lock-in amplifier, where the noise floor was ~ 35 $\text{nV}/\sqrt{\text{Hz}}$. This noise was then converted to the magnetic field sensitivity with the slope at ϵ_- and γ_e (plotted in the right y-axis in Fig:4-9d).

Noise Estimation

In our experiment, the measurement noise (38 $\text{nV}/\sqrt{\text{Hz}}$ at $f_m = 1.5$ kHz) primarily derives from the green laser intensity noise, due to the limited performance of the optical filters. This laser intensity noise was orders of magnitude larger than other noise sources: (i) the NV red fluorescence shot noise was $R\sqrt{2qi_D} \sim 9$ $\text{pV}/\sqrt{\text{Hz}}$ at

$f_m = 1.5$ kHz, where $i_D \sim (1/C)(100\ \text{nV}/\sqrt{Hz})/R$, the ODMR contrast of $C \sim 0.02$, $q = 1.6 \times 10^{-19}$ C, and $R = 50\ \Omega$; (ii) the thermal noise of 50 Ω resistance was $\sim 0.9\ \text{nV}/\sqrt{\text{Hz}}$, which was used to convert the photo-current to voltage; and (iii) the noise converted from the microwave spectral purity ($\phi_p = -90$ dBc/Hz at f_m) was $\propto V_s \phi_p f_m \beta \sim 1\ \text{fV}/\sqrt{\text{Hz}}$. Here, V_s is the signal voltage amplitude, and β is the slope of the FM-ODMR curve. We assumed that $\phi_p \ll 1$.

Conclusion and Outlook

The achieved magnetic field sensitivity is orders of magnitude worse compared to the best DC sensitivities reported: 290 $\text{pT}/\sqrt{\text{Hz}}$ and 28 $\text{pT}/\sqrt{\text{Hz}}$ for vector[39] and scalar[34] magnetometry, respectively, to our best knowledge. Our sensitivity is mainly limited by the green laser intensity noise (Section 4.6). However, this performance can be improved by including (i) metal gratings in multiple CMOS metal layers based on the wavelength-dependent Talbot effect[211, 89] and (ii) fabricating a resonant grating[145] in diamond. These additionally attenuate the green laser and consequently reduce the laser intensity noise by several orders of magnitude. In addition, using a diamond waveguide geometry[39] – possibly with a higher NV density[2] (0.01 ppm to 10 ppm) – should increase the SNR by orders of magnitudes. Moreover, dynamical decoupling sequences[188, 44] can improve the sensitivity by a few orders of magnitude for measuring magnetic fields at frequencies above the NV decoherence rate.

One component not presently integrated into our diamond-CMOS platform is the pump laser for NV optical excitation. This optical pump can be integrated into our platform through using a chip-scale laser diode[137], green Vertical-Cavity Surface-Emitting Lasers[101], or CMOS-compatible waveguided delivery of the optical pump beam[129]. We note that the CMOS-integration of all currently off-chip electronic components, such as the phase-locked loop with frequency modulation and the lock-in amplifier, has been demonstrated in prior research[207]. These indicate the feasibility of millimeter-scale form factors for future quantum-sensing systems.

In conclusion, we demonstrated chip-scale quantum magnetometry by integrating diamonds with CMOS technology. Throughout the CMOS multi-layers, essential components to detect NV-ODMR - a microwave generator, an inductor, an optical pump beam filter, and a photodetector - were fabricated. NV spin ensembles integrated on to the CMOS chip measure external magnetic fields with the sensitivity of 32.1 $\mu T/\sqrt{Hz}$. This compact spin-CMOS platform can be extended toward on-chip sensing of other quantities such as electric fields. We emphasize that the CMOS circuit in this work provides direct physical interactions with the NV quantum states beyond electronic I/O signaling[33].

In addition to chip-scale quantum sensing capability, our CMOS-based spin control and readout scheme will uniquely provide a scalable solution for implementing spin quantum-bit controls. This is particularly essential to develop a large-scale quantum information processor[217, 203, 33, 143], which enables quantum enhanced sensing[63, 202, 44] and quantum information processing [23, 147, 86].

Chapter 5

High-Scalability CMOS Quantum Magnetometer with Spin-State Excitation and Detection of Diamond Color Centers

Magnetometers based on quantum mechanical processes enable high sensitivity and long-term stability without the need for re-calibration, but their integration into fieldable devices remains challenging[102, 87]. This chapter extends the work presented in Chapter 4, where we further miniaturize the conventional NV-quantum-sensing platform. By integrating key components for spin control and readout, the chip performed magnetometry through ODMR. The MW field was highly uniform across the NV centers in the diamond, which was enabled by a CMOS-generated ∼2.87 GHz magnetic field with <5% inhomogeneity across the large-area current-driven wire array. The magnetometer chip was 1.5 mm^2 in size, prototyped in 65-nm bulk CMOS technology, and attached to a 300×80 μm^2 diamond slab. NV fluorescence was measured by a CMOS-integrated photodetector. This on-chip measurement was enabled by efficient rejection of the green pump light through a CMOS-integrated spectral filter based on a combination of spectrally dependent plasmonic losses(4) and diffrac-

tive filtering in the CMOS BEOL. This filter achieves ∼25 dB of green light rejection. We measured a sensitivity of 245 nT/Hz$^{1/2}$, marking a 130× improvement over the previous CMOS-NV sensor prototype (Chapter 4). This improvement resulted from better spectral filtering and homogeneous microwave generation over a larger area. Much of this chapter is adapted from Ref. [89].

5.1 Introduction

Integrating solid-state quantum sensors with integrated electronics is gaining increasing attention[87, 102, 89]. Key to this attention are ensembles of NV centers in diamond which have emerged as an outstanding room-temperature sensor platform [73, 12, 187, 113, 183]. NV-based magnetometry has achieved sensitivities at or below the picotesla level[213, 39], with applications ranging from bacteria magnetic imaging[113], NMR spectroscopy[30], and wide-field microscopy of superconducting materials [168]. However, an impediment to fieldable devices lies in the co-integration of different subsystems needed for ODMR, including microwave generation/delivery to diamond, optical excitation, filtering and fluorescence-based spin detection.

Chapter 4 presented our solution to this integration problem by performing ODMR with a custom-designed CMOS circuit coupled to a diamond NV ensemble[87, 102]. However, insufficient pump light rejection and small homogeneous microwave field area posed a major limitation on magnetic sensitivity. In Chapter 5, we present a new CMOS prototype that addresses these problems to achieve a >100× sensitivity improvement, down to 245 nT/Hz$^{1/2}$[89].

The chapter is organized as follows, we describe the improved chip architecture that incorporates both high-homogeneity microwave delivery and improved optical filtering, realized in a 65-nm CMOS process. We then present our improved performance. It concludes with an outlook on further improvements to magnetometry and the incorporation of additional quantum sensing functions through increased scalability and reductions in cost, size and power.

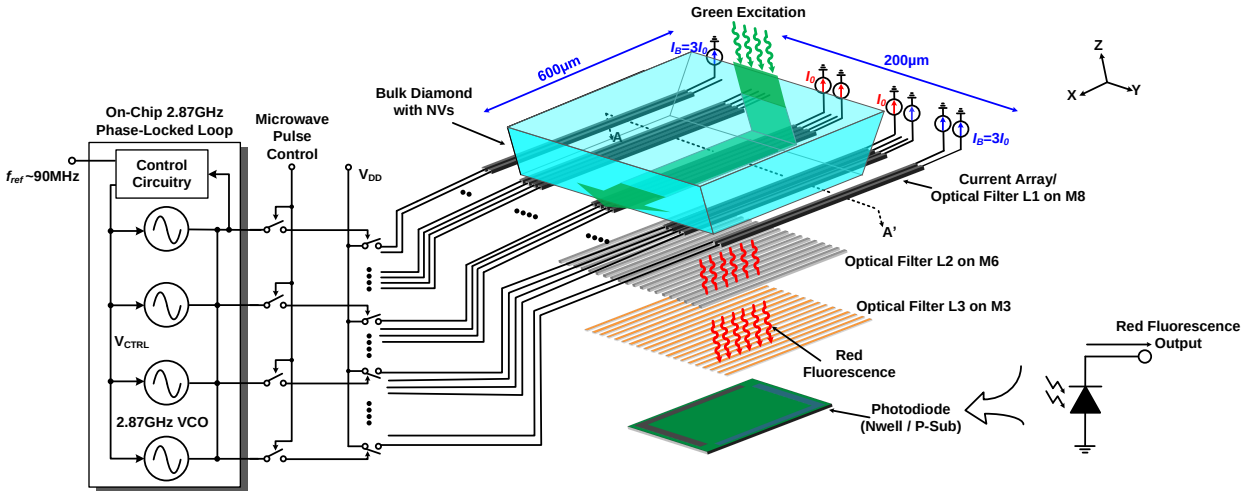

Figure 5-1: The overall schematic of the CMOS quantum magnetometer with high scalability.

5.2 Background and Prior Research

To explore the feasibility of a chip-scale, low-cost quantum magnetometer, a custom-designed CMOS prototype was realized and reported, for the first time, in [87]. This chip, using TSMC 65-nm CMOS technology, integrates most of the critical components (except the green light source) for ODMR. Using this hybrid CMOS-NV-center integration platform, the ODMR spectrum of a nanodiamond layer attached on top of the chip was measured (Chapter 4). The estimated sensitivity of the system was 74 $\mu T/Hz^{1/2}$. Since the lattice orientations in the nanodiamond particles are random, the amount of frequency splitting in each NV is also random. As a result, this prototype cannot be used for vector-field sensing. Recently, we attached a film of bulk diamond (with uniform and well-defined lattice structure) to the same CMOS chip and demonstrated vector-sensing capability with 32 $\mu T/Hz^{1/2}$ sensitivity[102].

Our first CMOS prototype demonstrates the basic concept of chip-scale miniaturization of NV-center quantum sensors. The achieved sensitivity was still limited by two main factors. The first was that the dominant noise source was the green shot noise despite the presence of the grating filter [102]. Ideally, this sensor would be limited by the red fluorescence shot noise and therefore, needs a higher green-to-red suppression ratio. We estimated that, for the diamonds used in [87, 102], the intensity

of red fluorescence was about 40∼50 dB lower than that of the incident green light. Ultimately, an additional 30 dB out-of-band rejection is required for the photonic filter, so that the majority of photodiode noise is no longer generated by the green background. The second factor limiting performance was the small sensing area (only 50 μm×50 μm). This limited the number of NV centers, N. Increasing N improves the sensitivity due to larger SNR of the ODMR spectrum. This can be achieved by using a larger sensing area and higher NV-center density. Note that the SNR has the following dependency with N:

$$SNR \text{ is } \begin{cases} \propto N & \text{when noise is green-light limited} \\ \propto \sqrt{N} & \text{when noise is red-light limited} \end{cases}. \tag{5.1}$$

5.3 A Scalable CMOS-NV Magnetometer for Enhanced Sensitivity

In this section, the design details of a new-generation CMOS-NV magnetometer[88] are provided. The highly scalable architecture of our CMOS-NV magnetometer allows for the microwave driving of NVs over a large area. The photodiode noise was further reduced with the adoption of a new on-chip photonic filter. These structures are co-designed with the on-chip electronics.

5.3.1 Systematic Architecture of the Chip

The overall schematic of the CMOS-NV magnetometer is given in Fig:5-1. Shown on the left of Fig:5-1 is an on-chip phase-locked loop (PLL) which generated the 2.87 GHz microwave signal (see Section 5.3.5). To drive the NVs with the on-chip generated microwave field, an array of current-driven linear wires were implemented using the M8 of the chip, of which the driving currents were toggled by the PLL output. Such a design addressed a major challenge regarding the uniformity of the microwave magnetic field over a large area. In Section 5.3.2, detailed explanations of the microwave launcher are provided. In this work, a diamond area of ∼500× 500

μm^2 is excited by the microwave. The sensing area with uniform microwave excitation was limited to 300 $\times$ 80 μm^2 as discussed in Section 5.3.4. Shown in Section 5.3.3 and 5.3.4, the current-driven wire array, along with additional two layers of metal gratings, form a photonic filter in order to suppress the green light. Finally, the spin-dependent red fluorescence of the NV centers was measured using a n-well/p-substrate photodiode.

5.3.2 Generation of High-Homogeneity Magnetic Field

Our NV-CMOS sensor interrogated an ensemble of NV centers to perform magnetometry. The microwave field strength determines both the ODMR resonance amplitude (C) and the resonance linewidth. In CW-ODMR, optimizing the sensitivity requires maximizing the contrast while minimizing the resonance linewidth [50]. For ensembles, the delivery of a homogeneous microwave magnetic field is critical in order to simultaneously perform this optimization across the entire area [53]. Such microwave homogeneity is also critical for coherent quantum control protocols, such as Ramsey-type sequence, which can significantly increase the magnetic sensitivity[188]. Homogeneous microwave fields *synchronously* rotate the spin states of a large number of NV centers on the Bloch sphere[20, 223]. Since the microwave-field strength determines the Rabi frequency of each NV electron spin, spatial variation of the microwave field causes dephasing of the overall quantum ensemble.

Traditional microwave-launching structures include single straight wires[50, 113], metal loops[180, 39, 183] and split-ring resonators[20, 223]. They can only keep the field homogeneity in an area that is much smaller than the launcher size. That is undesired for compact chip implementation when excitation of a large-size diamond is desired. Meanwhile, the above structures also have poor power-delivery efficiency, hence watt-level microwave input power is common[39, 20, 223]. We note the above solutions share one commonality in that they all rely on passive structures driven by a single electrical port. That, unfortunately, makes it extremely difficult, if not impossible, to synthesize a certain desired current distribution,[1] because the only

[1]For electrically-small structures (size$\ll\lambda_{2.87\mathrm{GHz}}$), the distributions of the current on the struc-

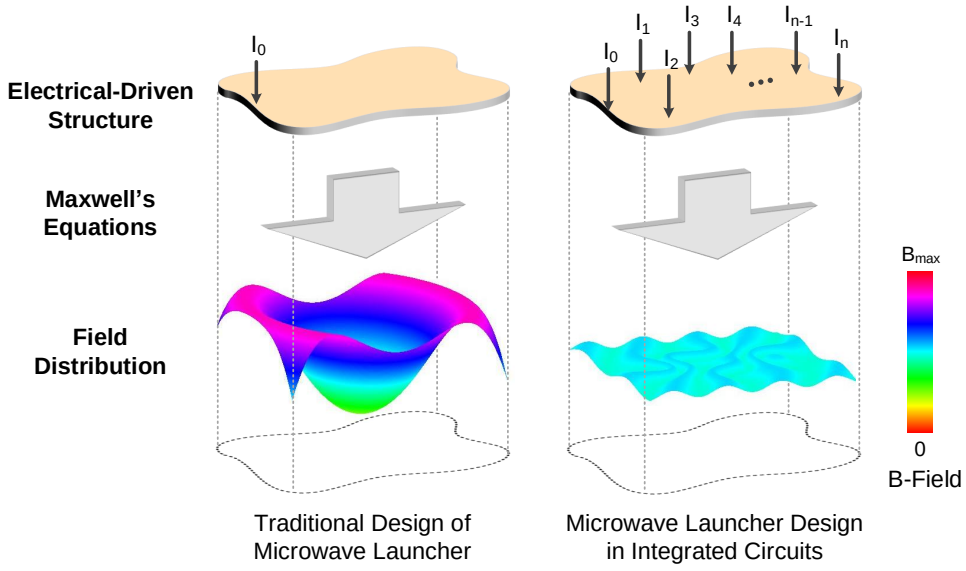

Figure 5-2: **Comparison of design methodologies for the microwave launcher in a quantum sensor.** A distributed co-design of passive and active components is equivalent to adding more boundary conditions to an electromagnetic-solving problem, hence providing better control of the near-field pattern.

design variable is the structural geometry.

One distinct advantage of the implementation using integrated circuits is the highly flexible and tight integration between passive and active components. A large number of biased transistors, when forming current sources, can be used to mandate the complex current values at various particular locations on the passive structure (Fig:5-2). Compared to the aforementioned passive-only structures, this new design methodology provides abundant additional degrees of freedom through the positions and currents of the embedded transistors. A finer control of near-field wave distribution is therefore much easier. Note that similar concepts were already proposed and applied to millimeter-wave and terahertz integrated circuit designs[77, 173, 83].

Following the above methodology, the microwave launcher design shown in Fig:5-1 evolved from an ideal, infinite sheet of uniformly-distributed surface current density J_x (see Fig:5-3a), which generates a homogeneous field B_y with a transverse (y-) direction and strength of $\mu_0 J_x/2$ (μ_0: permeability of vacuum). However, such current

ture and the generated near-field magnetic wave follow a one-to-one mapping. Note that although displacement current also generates magnetic fields, our following discussions are constrained to structures mainly with conduction current.

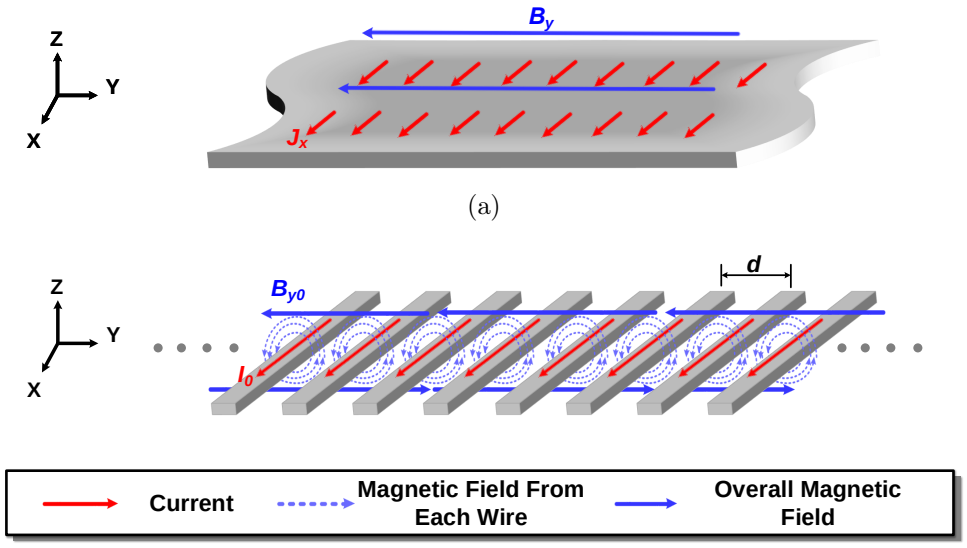

Figure 5-3: **Approaches to generate homogeneous magnetic field. a**, an infinite sheet of uniformly-distributed current, **b**, an infinite array of wires with uniform driving current.

uniformity is hard to imitate in a single metal structure, due to the self-redistribution of current like skin effect. To prevent such redistribution, the current sheet is first transformed into an infinite array of wires, each driven by an identical current I_0 (Fig:5-3b). With a tight wire center-to-center pitch d (or equivalent current density of I_0/d), a uniform transverse magnetic field can still be obtained, with a field strength of $\mu_0 I_0/2d$. The wire array also ensures high scalability in the longitudinal (x-) direction for large-area diamonds.

$$\oint Hdl = 2d \cdot H_{y1} = I_0 \quad \text{or} \quad H_{y1} = \frac{I_0}{2d} \tag{5.2}$$

In reality, only a finite wire array can be implemented. The introduced boundaries, however, break the above homogeneity. Fig:5-4 shows the simulated field distribution of a 48-wire array with d=4 μm. Although the transverse component of the field B_y maintains homogeneity, the vertical component B_z becomes non-zero and exhibits large gradient over y-axis. To understand that, we focus at a reference point (Point R) located above an array of N wires and closer to the left side (i.e. $y_R < 0$ in Fig:5-5a). The wires are then divided to three groups: the n wires located between

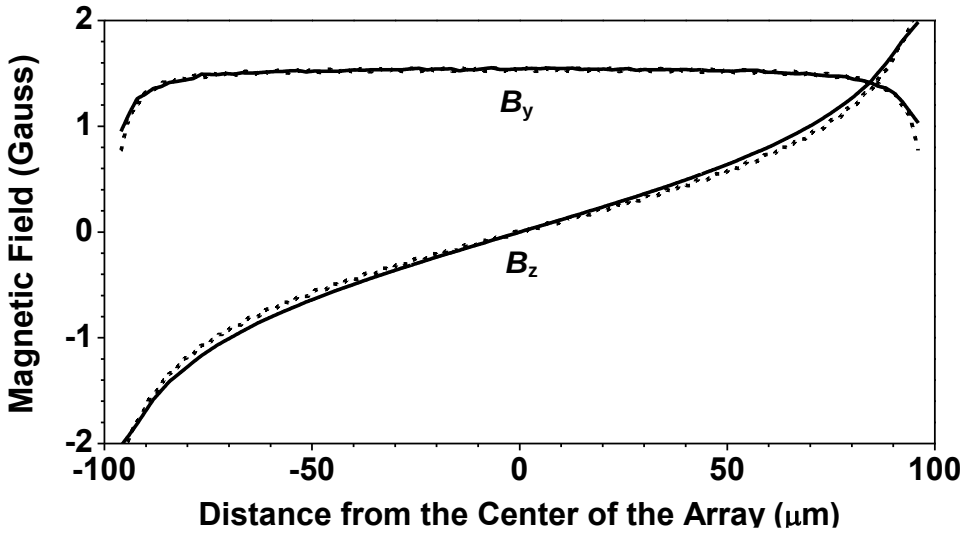

Figure 5-4: Simulated and calculated field distribution (f=2.87 GHz) of a wire array with uniform driving current (I_0=1 mA).

y_R and the left boundary $-L$ (Group A), another n wires symmetrically located at the right side of Point R (between y_R and $2y_R + L$, Group B), and the rest (Group C). Next, note that at Point R, the vertical magnetic fields generated by Group A and B cancel, and the B_z generated by Group C, by Ampere's Law, is:

$$B_{z,C}(y_R) = -\frac{1}{2\pi}\int_{2y_R+L}^{+L} \frac{\mu_0 J_x dy}{y - y_R} = \frac{\mu_0 J_x}{2\pi} \ln \frac{L + y_R}{L - y_R} \tag{5.3}$$

where the discreteness of the array is approximated as a uniform current sheet with a current density of $J_x = I_0/d$. Note that (5.3) also applies for $y_R > 0$. Shown in Fig:5-4, the result calculated from (5.3) well matches the simulation by HFSS[6]. Intuitively, B_z increases towards the edges because Group C has a larger total current there and gets closer to Point R.

To create an opposite magnetic-field gradient for nulling the above B_z, a pair of additional m-wire arrays (Group D in Fig:5-5b), which are driven by I_D per wire, were symmetrically placed at $y = -L-D$ to $-L$ and $y = L$ to $L+D$. Their combined

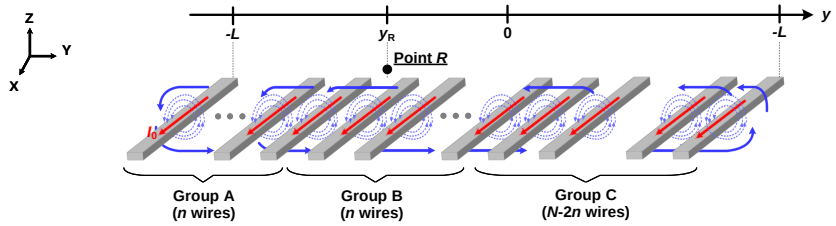

(a)

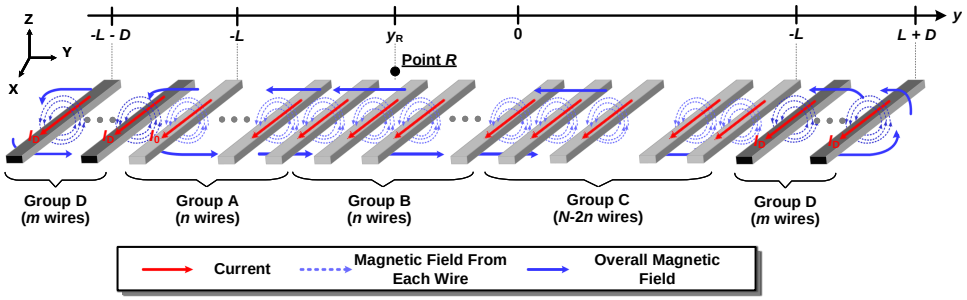

(b)

Figure 5-5: **Different Array Diagrams.** **a**, A finite array of wires with uniform driving current. **b**, An additional pair of boundary wire arrays (Group D) for nulling the vertical magnetic field between $-L$ and $+L$.

impact on the vertical magnetic field at $y = y_R$ is derived as:

$$\begin{aligned} B_{z,D}(y_R) &= \int_{-L-D}^{-L} \frac{\mu_0 m I_D dy}{2\pi D(y_R - y)} - \int_{L}^{L+D} \frac{\mu_0 m I_D dy}{2\pi D(y - y_R)} \\ &= \frac{m\mu_0 I_D}{2\pi D} \ln \frac{(y_R + L + D)(L - y_R)}{(L + D - y_R)(y_R + L)}, \end{aligned} \tag{5.4}$$

of which some example plots are shown in Fig:5-6, indicating the similarity of its curve shape to that from Group C. To further determine the value of I_D, we compared the derivatives of (5.3) and (5.4) around the center of the launcher:

$$\frac{dB_z}{dy}|_{y=0} = \begin{cases} \frac{\mu_0 J_x}{\pi L} & \text{for Group } C \\ -\frac{\mu_0 m I_D}{\pi L(L+D)} & \text{for Group } D \end{cases}. \tag{5.5}$$

Therefore, for zero B_z around the array center, the value of I_D should be:

$$I_{D,0} = \frac{L + D}{m} J_x = \frac{L + D}{md} I_0 = (1 + \frac{N}{2m}) I_0. \tag{5.6}$$

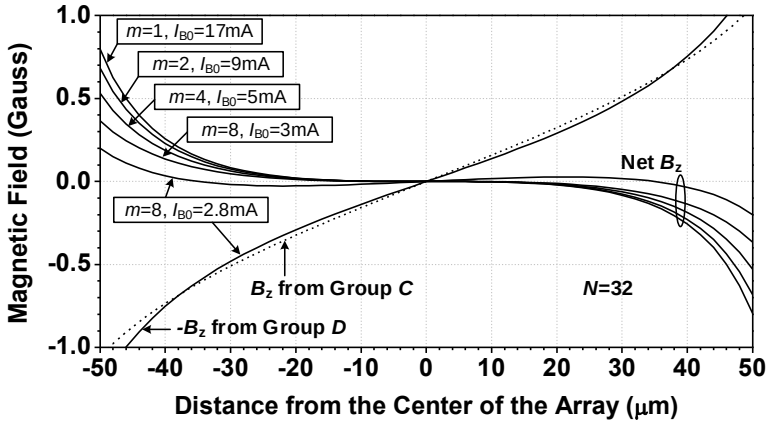

Figure 5-6: Calculated profiles of vertical field generated by Group C and D (and the residue after the cancellation) of the array shown in Fig:5-5b. Note that the B_z of Group D is plotted with its polarity reversed, to facilitate a straightforward comparison with B_z from Group C.

The last step of (5.6) assumed that the boundary arrays adopt the same wire pitch d as the N-wire uniform array in the center .[2] For a 32-wire uniform array (N=32) with I_0=1 mA and d=4 μm, the vertical field $B_{z,D}$ generated by the boundary array pair with varying wire numbers m, as well as the residual of B_z after cancellation, are plotted in Fig:5-6. We see that a larger m improves the area of uniformity at a modest expense of higher current consumption. Interestingly, if the I_D value is slightly lower than the one calculated by (5.6) (e.g. for m=8, the calculated value for I_D is 3 mA), the B_z field around y=0 is not cancelled perfectly but the overall 95% uniformity area is extended to $y \approx \pm 40$ μm. Lastly, Fig:5-7 shows the HFSS-simulated field distribution of the entire launcher (N=32, m=8, d=4 μm), which was implemented at the Metal 8 (M8) interconnect layer of our chip prototype. The calculated profile in Fig:5-7 was achieved with $I_D = 2.8 I_0$. Note that the HFSS simulation was done with a slightly larger I_D ($I_D = 3 I_0$) to account for the uncalculated effect of current in the return path. Compared to Fig:5-4, the overall homogeneity of the magnetic vector field was significantly improved.

[2]This condition is adopted in our design, but this is not necessary. Similarly, the strategy here assumes that the wires in Group D are adjacent to Group A, B and C. In Section 5.6, we show that a certain gap between the two groups achieves homogeneity across a larger area.

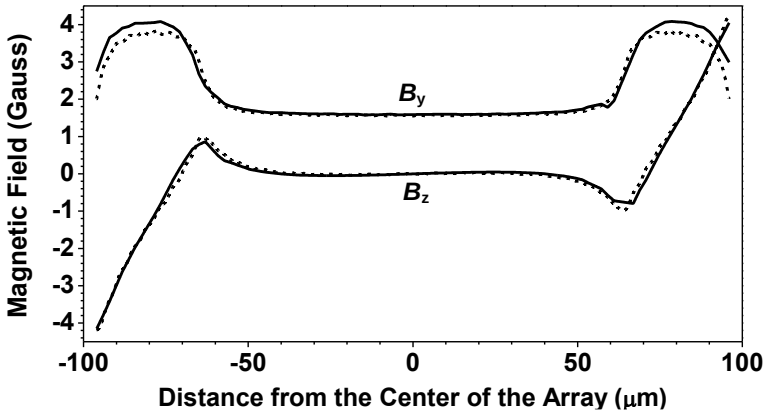

Figure 5-7: Simulated (solid line) and calculated (dashed line) field distribution of the entire launcher wire array. Here, f=2.87 GHz, N=32, m=8, I_0=1 mA, I_D≈3 mA.

5.3.3 Nano-Photonic Filter on CMOS

Using an FDTD solver, Lumerical, we simulated the green-to-red suppression ratio due to the slit in M8 layer (d=900 nm), which was ∼9 dB (Fig:5-10a) and was first shown in Chapter 4. Increasing the slit thickness by stacking more grating layers (in M7, M6...) was expected to further increase the suppression of the green light[80]. However, that caused degradation of red-light transmission due to the scattering at the side walls formed by the sparse inter-layer via pillars. Moreover, as Section 5.3.4

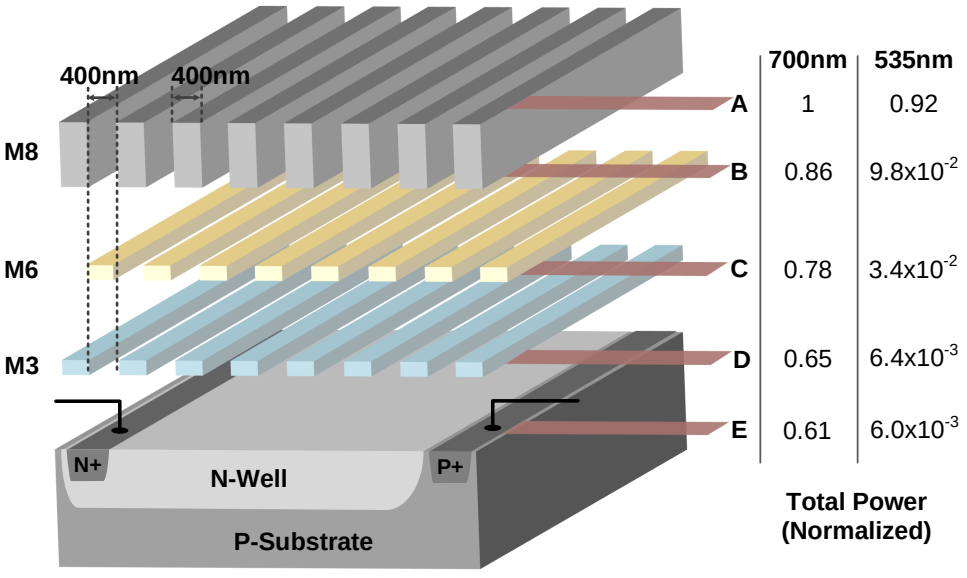

Figure 5-8: Simulated transmission values through the filter. The total power was derived by surface integrals of Poynting vectors at varying depths of the chip.

describes, the grating structure in M8 was also used for the microwave wire array (Section 5.3.2). Connecting it to the lower metal layers would significantly decrease the density and the uniformity of the RF current inside the wires. In our chip, an alternative approach based on the wavelength-dependent diffraction pattern of the grating was adopted.

As the simulation in Fig:5-10a shows, the diffraction of the light coming out of the grating in M8 caused repeated self-imaging patterns in the chip dielectric. That optical phenomenon is called the Talbot effect[185] and the vertical (z-) period of the self-images (i.e. Talbot length) is:

$$z_T = \frac{\lambda}{1 - \sqrt{1 - \frac{\lambda^2}{t^2}}}, \tag{5.7}$$

where λ is the wavelength in the dielectric and t is the grating period (800 nm in our case). For the red (700 nm) and green (535 nm) light, z_T was ~2.5 μm and ~3.4 μm (see Fig:5-10a). Thus we strategically placed additional metal structures at the Talbot length for green to block the light. In the 65 nm CMOS process used for this work, the distance between M8 and M6 layers was close to the half Talbot length for red; therefore, a M6 grating with 400 nm strip width and pitch was placed. With the positions of the metal strips right under the slits of M8, the M6 grating had little

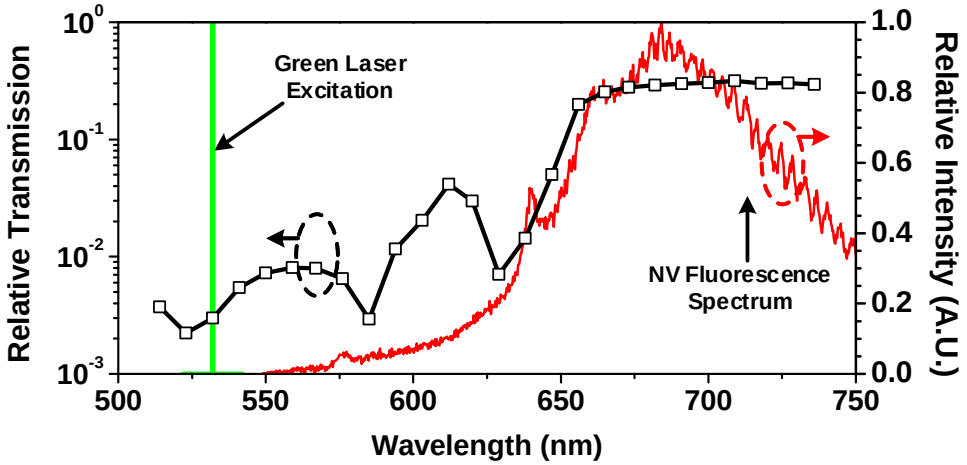

Figure 5-9: The transmission through the filter at different wavelength.

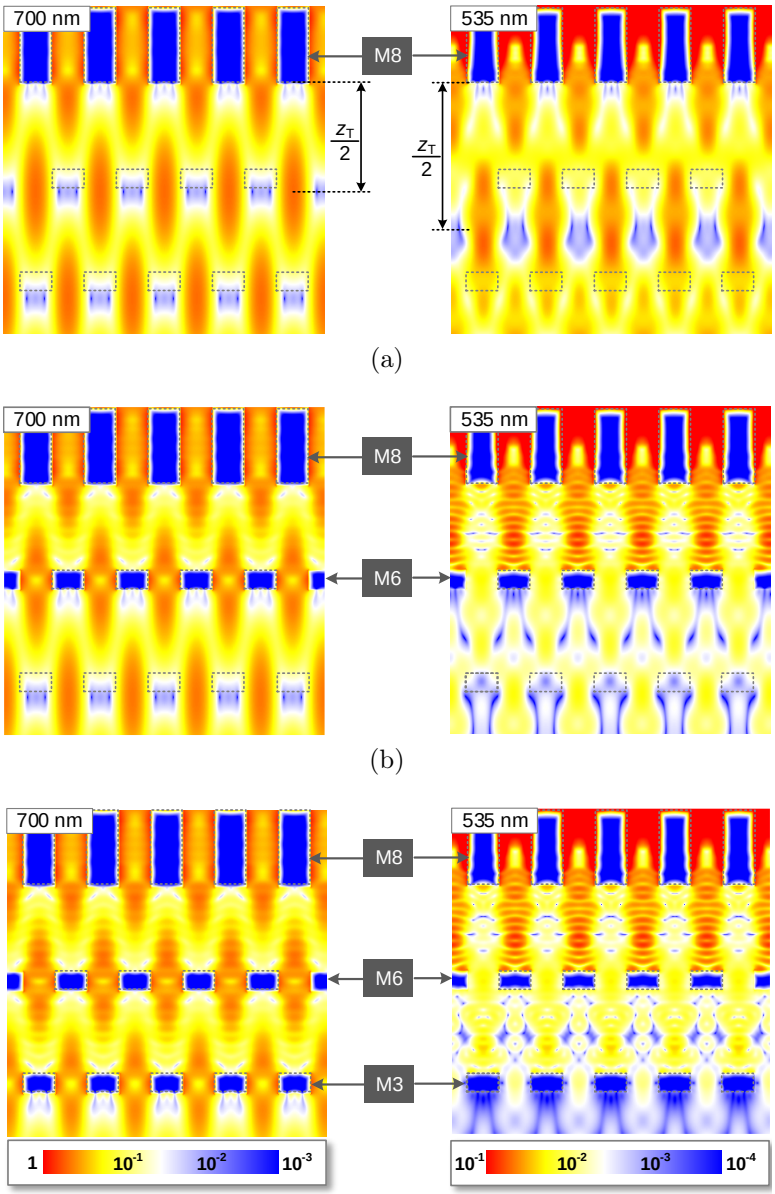

Figure 5-10: **Simulated Poynting Vector Profile.** The simulated FDTD Poynting vector profile $|P|=|E \times H|$ for **a**, single-layer grating in M8, **b** double gratings in M8 and M6, and **c** triple-layer gratings in M8, M6 and M3. Note: the scale bar for green (right column) was 10× lower than that for red (left column), in order to count for the ∼10-dB plasmonic loss in the M8 grating and to better show M6 and M3 gratings further suppress the transmission at 535 nm.

interference with the red-light transmission, while blocking a significant portion of the green light (Fig:5-10b). It is noteworthy that a similar multi-grating concept was previously adopted for lensless 3D CMOS cameras[205], where the angle sensitivity

of the structure is utilized. To the authors' best knowledge, this is the first time in CMOS that the idea of diffraction selectivity is applied into optical spectral filtering.

Following the same principle, a third grating layer in M3, was added to further enhance the green-light rejection (Fig:5-10c). The same grating strip width and pitch of 400 nm was used. Fig:5-8 provides the normalized transmitted power (Poynting vector integrated over a x-y cross-sectional area) at varying chip depths. For green light, the plasmonic behavior attenuates the power by 9.7 dB, and the M6 and M3 gratings pose an additional 12.1 dB loss, leading to a total attenuation of 21.8 dB. Meanwhile, the total insertion loss for red light was only 2.1 dB. Note that the reflection loss at the top of M8, which was $\sim$3 dB due to the 50% metal fill factor, was not included in both cases.

Lastly, the simulated transmission response (excluding the 50% surface reflection) of the filter from 500 nm to 750 nm was plotted in Fig:5-9. The spectrum of the NV-center red fluorescence was also shown. It can be seen that the majority of the fluorescence power between 650 to 725 nm was transmitted efficiently to the photodiode beneath the filter.

5.3.4 Co-Design of the Circuits, Microwave Launcher and Photonic Filter

The full schematic of the microwave launcher with the switches and current sources banks is shown in Fig:5-11. NMOS current mirrors were used to control the current in each individual wire of the array. PMOS switches were used to convert the output voltage of the PLL into microwave currents in the array. The current sources were design to enable current control from $I_0 = 0.1$ mA to $I_0 = 1$ mA. At low current values our simulation in Fig:5-12 indicates that when the PMOS switches were off, the current of wire returns to zero at a slow speed. This is due to the large parasitic capacitance of the wire array and the limited discharging current. To increase the pull down speed, a row of NMOS switches were also used (see Fig:5-11) to provide a fast discharging (see the comparison in Fig:5-12). The transistors dimensions (W_1/L_1,

W_2/L_2, and W_3/L_3) were scaled up by a factor of 3 at the boundaries. As described in Section 5.3.2, the microwave launcher was implemented on M8 with wire width and spacing of 2 μm. Therefore, all the transistor layouts were designed in a multiplier fashion so that they can fit in the tight wire pitch. A pair of wide return ground paths were used to close the current loop.

Part of the photonic filter was also implemented on M8 with unit width and spacing of 400 nm (shown in Fig:5-8). The smallest dimension, limited by the design rule of the technology, was selected to enhance the coupling to the surface plasmon polariton mode. To cater the needs of both components, shown in Fig:5-11, each of the microwave launcher wires other than the boundary wires were divided into three sub-wires with their two ends electrically connected. The width and the spacing of these sub-wires were 400 nm. In addition, each of the 2 μm spacing in the microwave launcher was filled with another two floating dummy wires with 400-nm width and spacing (Fig:5-11). These dummy wires do not affect the microwave generation/delivery operation, but along with the other sub-wires, they form the desired photonic filter geometry, which was 350×130 μm^2 of total area. In this prototype, a

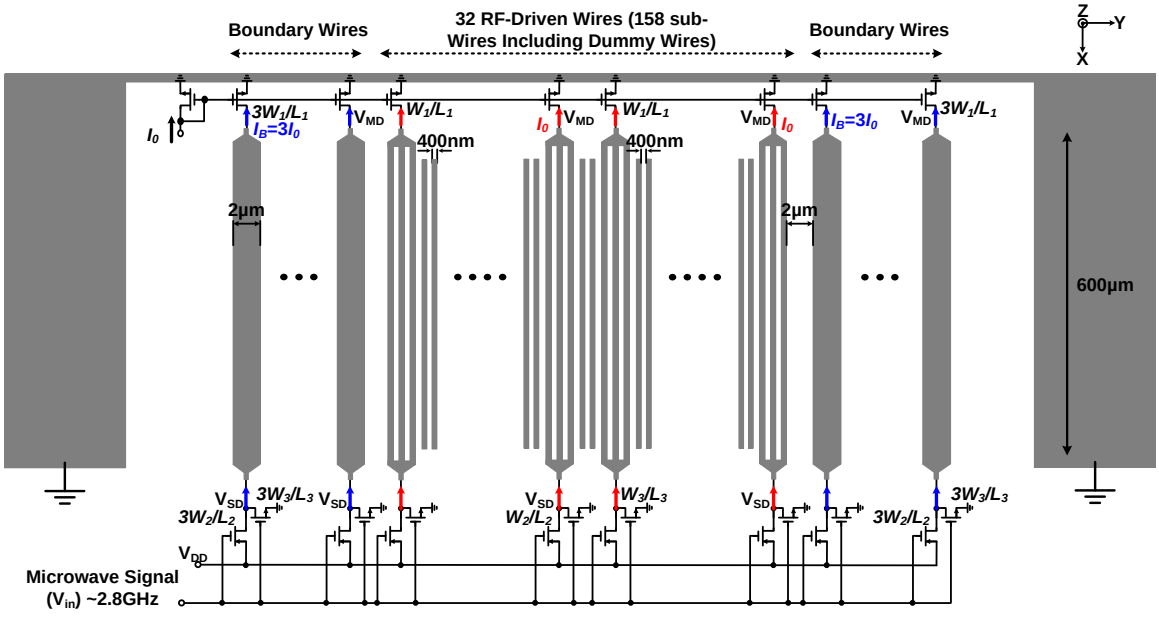

Figure 5-11: Schematic of the microwave launcher with the switches and the current sources.

conservative size was adopted for the sensing area, since the edge effects like leakage of light were uncertain. The size of the photodiode placed under the filter was 300×80 μm^2. In future designs, the photodiode area may increase for better SNR.

This array generates >95% field homogeneity over > 50% of its area compared to 25% in [87]. Uniform array spacing was adopted in this design, however, in Section 5.6, we show that a certain gap between group D and group A/C can achieve homogeneity across a larger area. The design was only enabled by CMOS technologies, where we can integrate a very tight wire array with efficient switching and current control.

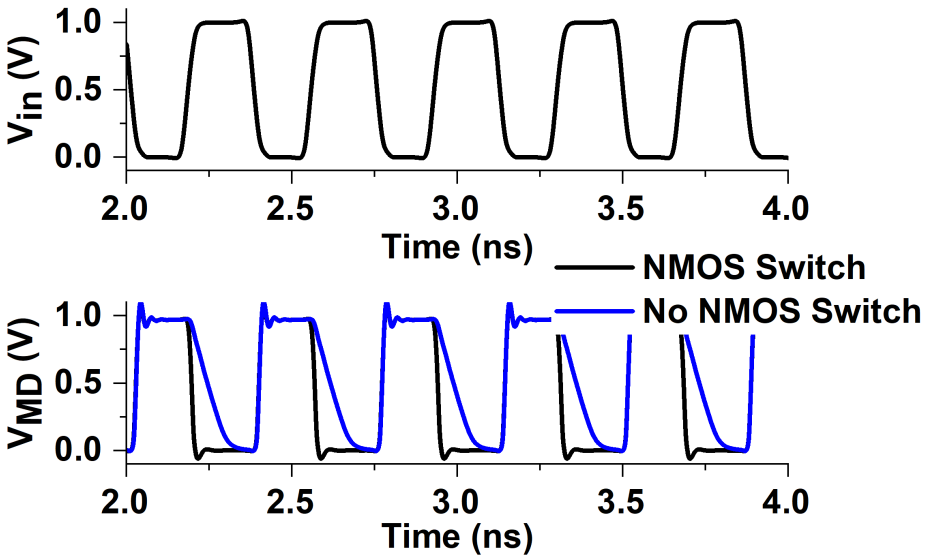

Figure 5-12: Comparison the switching performance with and without extra NMOS switch. The first plot shows the input microwave signal (V_{in}) and the second one shows the voltage at the drain of the NMOS current source (V_{MD}).

5.3.5 On-Chip Synthesis of the Microwave Frequency

A PLL loop was used to stabilize the output of the VCO that drives the NV centers. The full schematic of the PLL was shown in Fig:5-13. To ensure a uniform phase of the magnetic field across the wire array, the VCO was based on a tightly-coupled ring-oscillator array. Four sub-oscillators were placed with a spacing of ∼50 μm (see Fig:5-1). The two oscillators in the middle drive 32 wires, while the other two oscillators on the array boundaries drive 8 wires each. Compared to a central-

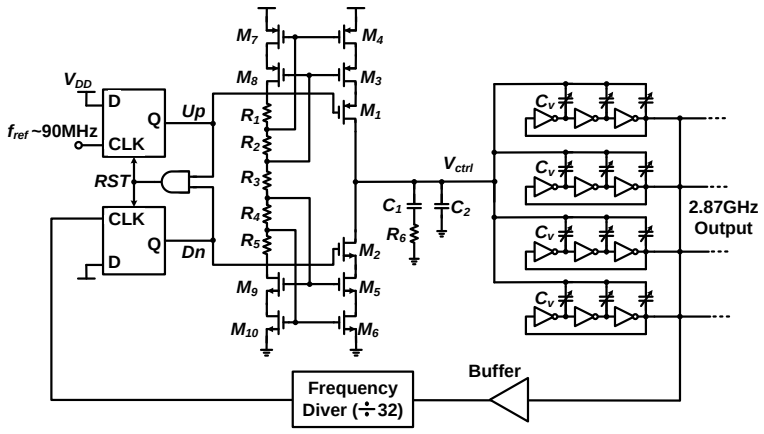

Figure 5-13: Schematic of the 2.87-GHz PLL.

ized signal-generation scheme, the coupled-oscillator eliminates the phase variation caused by different lengths of the microwave-distributing traces. Here, ring oscillators, instead of LC oscillators, were chosen, in order to eliminate the need for extra inductors, as well as any magnetic coupling and degradation of field homogeneity in the diamond-sensing area. A ring oscillator also offers wider tuning range and layout compactness. Its inferior phase noise was improved by 6 dB due to the oscillator coupling, and in fact our analysis indicates that our sensor sensitivity was currently limited by the green and red light noise, as explained in Section 5.5. The VCO frequency was tuned using varactors (C_v=9 to 42 fF) with a coefficient of 1.2 GHz/V. The charge pump current of the PLL was 5 mA and the loop filter parameters were C_1=1 nF, R_6=220 Ω, and C_2=20 pF.

5.4 Chip Prototype and Experimental Results

The chip prototype was fabricated using a TSMC 65-nm CMOS technology. The chip micrograph is shown in Fig:5-14. The chip has an area of 1×1.5 mm^2 and consumes 40 mW of power. A diamond slab with NV centers was placed and attached on top of the CMOS chip as shown in Fig:5-1. This diamond was a single crystalline CVD-grown diamond from Element 6. It was electronically irradiated with a dosage of 10^{18} e$^-$/cm^2 at 1 MeV, and then annealed for 2 hours at 850°C. Immersion oil was used to adhere the diamond slab to the chip. By bridging the difference of the refractive index, the

oil also minimizes the fluorescence loss. The measured filter rejection for green light (532 nm) was ∼25 dB, which matches the simulation results in Section 5.3.3. A 45° cut was introduced in the diamond's corner to direct the vertical incident green laser horizontally. This further enhanced the overall green rejection ratio to ∼33 dB. The measured responsivity of the on-chip photodiode was 0.19 A/W.

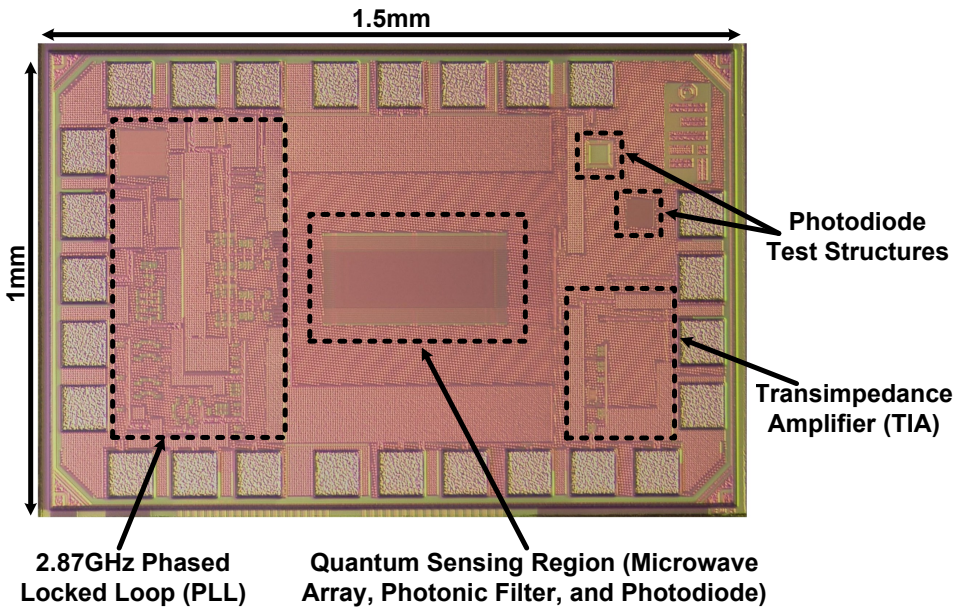

Figure 5-14: The micrograph of the CMOS quantum magnetometry chip.

5.4.1 ODMR Measurements

The measurement setup to generate the ODMR spectral line is shown in Fig:5-15a. A 532-nm laser light was used to excite the NV centers in the diamond. The red fluorescence from the on-chip photodiode was recorded while sweeping the reference signal (∼100 MHz) of the on-chip PLL. Due to the limited green-red suppression ratio of the on-chip filter, the red fluorescence signal was still superposed on a large green-light background at the output of the photodiode. Meanwhile, we note the green-light excitation exhibits large power fluctuation. To remove the fluctuating background signal, a FM scheme was used, where the microwave frequency $f_p(t)$ was periodically varied with a deviation of 6 MHz and repetition frequency f_m of 3 kHz. That was done by modulating the 100 MHz reference signal of the on-chip PLL. As shown in

Fig:5-15b, the corresponding photodiode output changes at f_m (with harmonics at $2f_m$, $3f_m$, etc.). Such a time-varying component mainly results from the transition line and the associated red-fluorescence change, which was then readily measured by a lock-in amplifier (SR865) with the reference at f_m. The lock-in amplifier also provides narrow-band filtering around f_m. Note that the FM technique is common in spectroscopy[206] and atomic/molecular clocks[207]. Lastly, to further de-embed the excitation noise within the lock-in amplifier bandwidth, a differential detection scheme was adopted, where a split beam off the same laser was measured by an off-chip photodiode; such a duplicated noise signal was then taken by the lock-in amplifier

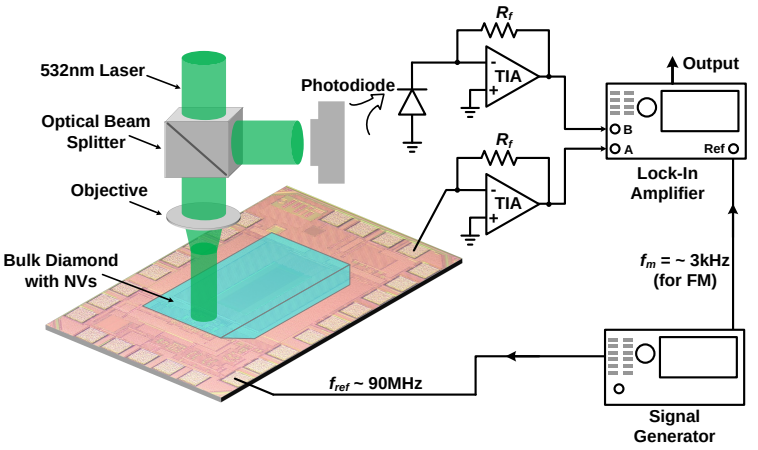

(a)

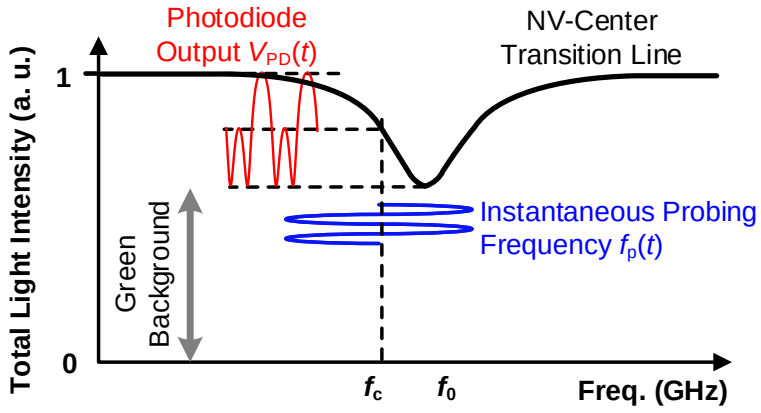

(b)

Figure 5-15: **FM Experiment Schematic.** **a**, The test setup for the hybrid NV-CMOS magnetometer. **b**, The frequency-modulation scheme used in the setup.

and was subtracted from the chip output. Two identical resistive transimpedance amplifiers (TIA) with gain of 10K were used to convert the photodiode currents into voltage. This gain was chosen to prevent the saturation of the amplifier due to the green current background (40 μA)

First, without an externally applied magnetic field, the ODMR plot shown in Fig:5-16a was measured. A strong spin resonance, which results from all four NV centers in the diamond lattice, was detected at 2.87 GHz. The FM technique introduced previously can be interpreted as taking the first-order derivative of the regular transition line; as a result, the measured curve has the zigzag shape shown in Fig:5-16a. The zero-crossing point corresponds to the actual transition frequency. Next, a 5.4 mT DC magnetic field was applied to the sensor from a nearby permanent magnet. This results in a Zeeman splitting. As shown in the measured ODMR plot in Fig:5-16b, four pairs of resonances were observed. They correspond to the four NV-center orientations of the single crystalline diamond. The difference of the transition frequencies (i.e. zero-crossing points) in each resonance pair was proportional to the external static magnetic field along the associated NV-center orientation. The proportionality constant, as described in Section 5.2, was γ_e=28 GHz/T. Accordingly, the magnetic fields along the four NV-center orientations were 0.77 mT, 2.27 mT, 3.25 mT, and 4.77 mT, respectively. Lastly, as the comparison between Fig:5-16a and 5-16b shows, the chip output signal with external magnetic field was reduced due to the breaking of the degeneracy of the resonances from 2.87 GHz. Fig:5-16b indicates that, by mapping the projections of the external magnetic field along the four NV-center orientations the Cartesian components of the applied magnetic field can be reconstructed.

One practical way to use the sensor for vector-field sensing, was to first "bias" the sensor with a static magnetic field (e.g. a permanent magnet), which allows for the four resonances to be completely split (such as shown in Fig:5-16b). Then, we record the additional change of the sensor output voltage $\Delta v_{\mathrm{out,i}}$ (i=±1, ±2, ±3, ±4) around each zero-crossing point of the FM-based ODMR curve. Note that $\Delta v_{\mathrm{out,i}}$ was caused by the shift of each resonance frequency Δf_i due to the projection of the

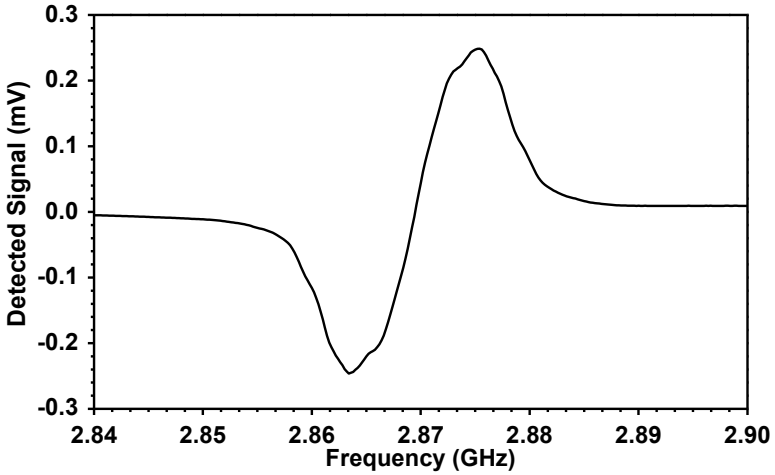

(a)

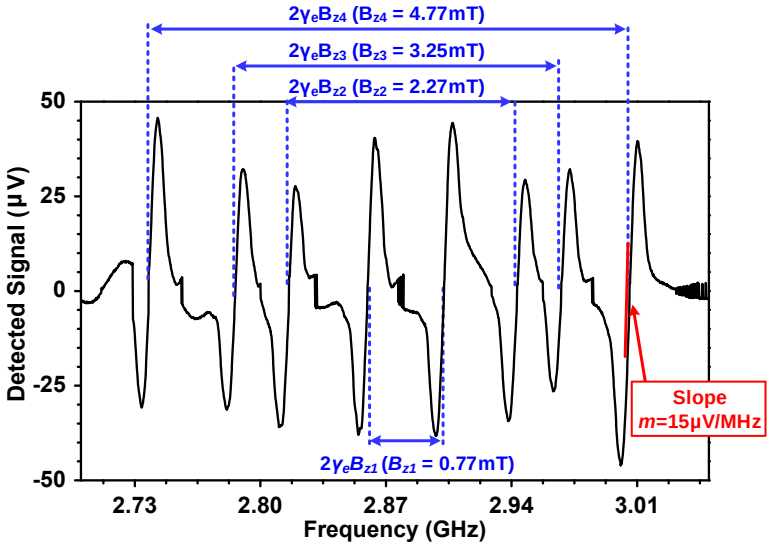

(b)

Figure 5-16: **Measured ODMR plot from the CMOS chip.** **a**, No external magnetic field was applied, and **b**, a 5.4 mT external magnetic field was applied.

added field on the associated NV-center axis ΔB_{zi} (to be measured) on top of the bias static field, its expression was (for positive i):

$$\Delta v_{\mathrm{out,i}} = m\Delta f_i = m\gamma_e \Delta B_{\mathrm{zi}}, \tag{5.8}$$

where m was the slope of the ODMR curve at each transition zero-crossing point ($\sim$15 μV/MHz in our case, see Fig:5-16b). The value of ΔB_{zi} can be derived from $\Delta B_{\mathrm{zi}} = \Delta v_{\mathrm{out,i}}/(m\gamma_e)$. Note that the transition frequencies of both $|m_s = \pm 1\rangle$ sub-levels are also temperature dependent (with a coefficient of -74 kHz/K[3]). To cancel such temperature-induced drifts, it was better to measure the differential change of each pair of $|m_s = \pm 1\rangle$ transitions, and use the following equation for ΔB_{zi}[102]:

$$\Delta B_{\mathrm{zi}} = \frac{\Delta v_{\mathrm{out,i}} - \Delta v_{\mathrm{out,-i}}}{2m\gamma_e} \quad (i = 1, 2, 3, 4). \tag{5.9}$$

5.5 Magnetic Sensitivity Estimation

In order to calculate the magnetic sensitivity of the sensor, the noise floor, σ (unit: V/Hz$^{1/2}$), was measured. The sensor noise was measured by monitoring the read-out of noise in the lock-in amplifier while sweeping the modulation frequency f_m. The results are shown in Fig:5-17, where the sensor shot noise floor was $\sim$0.1 μV/Hz$^{1/2}$. The increased noise below 3 kHz was caused by the interference from the unshielded testing environment. This allows us to calculate the magnetometer sensitivity η_B (unit: T/Hz$^{1/2}$), which is the minimum detectable magnetic field with 1 s integration time, using the following equation:

$$\eta_B = \frac{\sigma}{\gamma_e m}. \tag{5.10}$$

η_B was 245 nT/Hz$^{1/2}$ at f_m=3 kHz.

The sensor performance was limited by the green shot noise. The estimated theoretical magnetic sensitivity (η_g) of the sensor can be estimated using the following:

$$\eta_g = \frac{\sigma_g}{\gamma_e m} = \frac{\sqrt{2(2qi_gR_f^2 + 4KTR_f)}}{\gamma_e m} \tag{5.11}$$

where σ_g is the theoretical noise limit from the green light. The first term of σ_g represents the shot noise of the green light detected by the photodiode. q is the electronic charge, i_g is the current measured at the photodiode due to the green light (~40 μA), and R_f is the feedback resistor of the TIA (10 kΩ). The second term represents the noise of the TIA (assuming it was mainly limited by R_f). K is the Boltzmann's constant, T is the temperature. The factor of 2 was due to the addition of the noise power due to the two detection branches. The calculated theoretical value was ~150 nT/Hz$^{1/2}$, which agrees to good extent with the measured value, and the difference was due to the residual green light fluctuation. Even though this differential measurements technique increases the total shot noise limit by a factor of $\sqrt{2}$, it helps in canceling almost all the external laser fluctuation, which was almost one order of magnitude larger than the shot noise limit in our case.

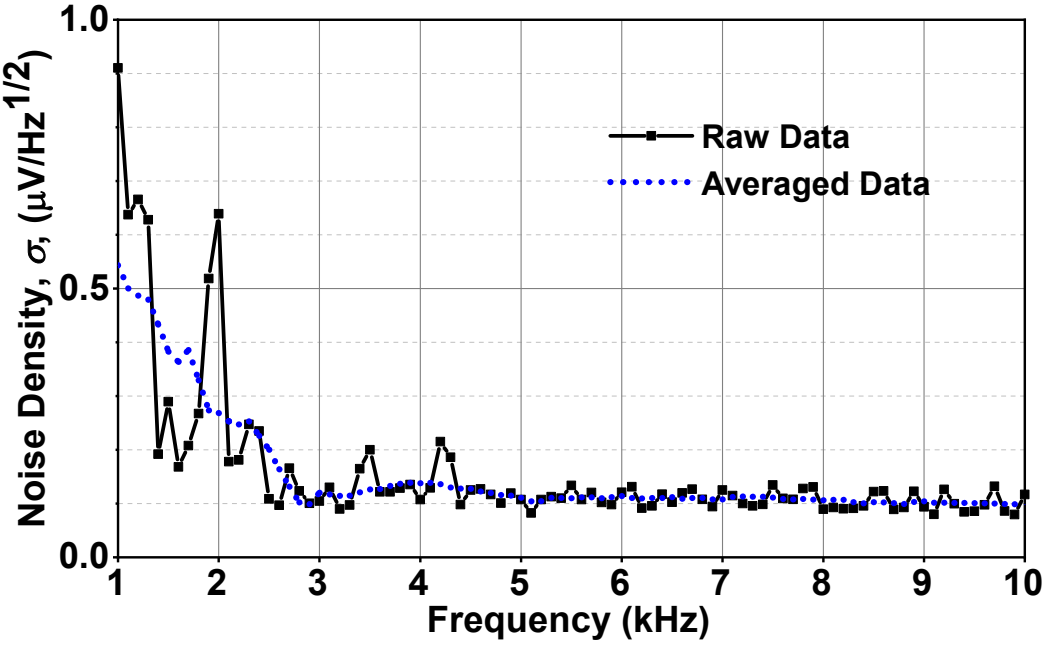

Figure 5-17: The measured output noise floor of the sensor.

To confirm that the green light noise was the dominant source of noise. The contributions of the other noise sources in the system were estimated as follows:

1. The magnetic sensitivity due to the NV red fluorescence shot noise (η_r) was $\sim 10\text{nT}/\sqrt{\text{Hz}}$ at $f_m = 3$ kHz as given in:

$$\eta_r = \frac{\sigma_r}{\gamma_e m} = \frac{\sqrt{(2qi_r)R_f^2}}{\gamma_e m} \approx \frac{\sqrt{(2q\frac{V_{\max}}{CR_f})R_f^2}}{\gamma_e m}. \tag{5.12}$$

In (5.12), $V_{\max}$ was the maximum voltage of the ODMR curve in Fig:5-16b, which was $\sim$45 μV, and C was the ODMR contrast of ~ 0.01.

2. The magnetic sensitivity (η_m) due to the amplitude noise converted from the microwave generator spectral purity is determined by (see 5.5):

$$\eta_m = \frac{\sigma_m}{\gamma_e m} \approx \frac{2\pi f_m \phi_n m}{\gamma_e m} \approx \frac{2\pi f_m \phi_n}{\gamma_e}, \tag{5.13}$$

where m was the slope of the FM-ODMR curve. Based on the measured PLL phase noise (ϕ_n) of -88 dBc/Hz at f_m, η_m is ~ 30 pT/$\sqrt{\text{Hz}}$.

Estimation of the Contribution of the Microwave Phase Noise on the Sensor Sensitivity

The microwave signal that drives the NV centers can be represented as:

$$V_{\text{RF}} = V_0 \cos(\omega_0 t + \phi_n(t)), \tag{5.14}$$

where V_0, and ω_0 are the microwave signal amplitude and frequency, respectively. $\phi_n(t)$ was the phase noise of the microwave frequency. The instantaneous frequency can be represented as:

$$\omega(t) = \omega_0 + \frac{d\phi_n(t)}{dt}, \tag{5.15}$$

The frequency fluctuations around the operating frequency (ω_0) was related to the phase noise by:

$$\delta\omega = \frac{d\phi_n(t)}{dt}, \tag{5.16}$$

In our case, a lock-in amplifier was used to observe the noise around the modulation frequency (ω_m). Therefore, $\phi_n(t)$=$\phi_n \cos 2\pi f_m t$ can be assumed to have a sinusoidal form, where ϕ_n was the phase noise of the microwave source at the modulation frequency (f_m) in dBc/Hz. This means the peak frequency fluctuation was $\approx 2\pi f_m \phi_n$. Therefore the voltage spectral density due to the PM to AM noise conversion was represented as:

$$\sqrt{\frac{\bar{V_n^2}}{\delta f}} \approx 2\pi f_m \phi_n m, \tag{5.17}$$

where m was the slope of the FM curve in V/Hz.

Estimation of Sensitivity for Future Hybrid CMOS-NV Magnetometers

The sensor sensitivity was inversely proportional to the SNR of the sensor output:

$$S \propto \frac{1}{SNR} = \frac{\sigma_i \cdot \Delta\nu}{\gamma_e \cdot I_r}, \tag{5.18}$$

where σ_i was the total noise current density (unit: A/Hz$^{1/2}$), $\Delta\nu$ is the linewidth of the ODMR curve, I_r is the photo-current due to the red fluorescence signal, and γ_e is 28 GHz/T. From our experiments, the linewidth of the ODMR was 6 MHz. The noise was limited by the shot noise of either the green excitation (for low optical filtering ratio) or the red fluorescence (for high optical filtering ratio):

$$\sigma_i = \sqrt{2 \cdot q \cdot (I_g + I_r)}, \tag{5.19}$$

where q is the electronic charge, and I_g and I_r are the photo-currents due to the unfiltered green light and red fluorescence, respectively. The value of I_g was estimated as:

$$I_g = P_g \cdot R_{\mathrm{PD}} \cdot \eta_g, \tag{5.20}$$

where P_g is the input optical power, R_{PD} is the photodiode responsivity, and η_g is the green rejection of the optical filter. The value of I_r is proportional to the total number n_{nv} of NV centers in the diamond, which is proportional to the sensing area A_{nv} and NV density ρ_{nv}. Lastly, the performance using the spin-controlled pulse sequence was estimated based on the fact that the equivalent transition linewidth (hence the zero-crossing slope m) of the configuration was reduced by $\sim$100$\times$ for AC magnetic field measurements [188, 16].

5.6 Conclusions

In this Chapter, we present a vector-field magnetometer, which was based on a hybrid-CMOS chip-scale platform. The chip has the essential components for the manipulation and detection of the NV centers' spin states. We demonstrate room-temperature magnetic field sensing with a sensitivity of 245 nT/Hz$^{1/2}$, which was 130$\times$ better

	Tech	Optical Isolation	Sensing Area	Form Factor	Sensitivity
Clevenson, et al.; (Nature Physics, 2015)	Discrete Devices	>60 dB	1 mm x 1mm	~ 1 m^3	0.29 nT Hz$^{-0.5}$
Fescenko, et al.; Arxiv 2020	Discrete Devices	>60 dB	1 mm x 1mm	~ 1 m^3	0.9 pT Hz$^{-0.5}$
CMOS-NV Magnetometer 1.1 VLS, 2018	65 nm CMOS	10 dB	50 µm x 50 µm	~ 1 mm^3	73 uT Hz$^{-0.5}$
CMOS-NV Magnetometer 1.2 Nature Electronics, 2019	65 nm CMOS	20 dB	50 µm x 50 µm	~ 1 mm^3	32 uT Hz$^{-0.5}$
CMOS-NV Magnetometer 2.0 In submission, 2020	65 nm CMOS	35 dB	80 µm x 100 µm	~ 1 mm^3	245 nT Hz$^{-0.5}$

Figure 5-18: Table comparing different figures of merit across different NV sensing experiments. The top two rows are experiments done with discrete devices while the bottom three rows show the progress made across Chapters 4 - 5.

than our previous prototype [102]. A microwave launcher with uniform microwave generation was introduced that can be scaled up for large diamond areas (i.e. large SNR). An enhanced multi-layer nanophotonic filter for lower background noise was also presented.

Figure 5-18 compares our work vs other published works. You can see that while our sensitivity has improved by over two orders of magnitude from [87] to [89], it is still ∼5 orders of magnitude worse than the best reported values[57]. While these experiments have reported better sensitivity, they are also significantly larger (1 m^3) compared to our own device (1 mm^3). The scalable architecture and component designs presented in this Chapter provide a clear pathway to further push the sensitivity of our sensor to this performance. This is shown in Fig:5-19, which plots the estimated sensitivity with varying optical filtering performance, sensing areas and NV-centers densities. As shown in Fig:5-10, current locations for lower optical grating layers are still not optimal due to the fixed BEOL stack configuration. In more advanced CMOS technology nodes, where a denser stack of thinner metal layers are available, the optical filtering performance can be further improved. For the microwave launcher, a better optimized configuration of the boundary wire arrays (i.e. Group D in Fig:5-

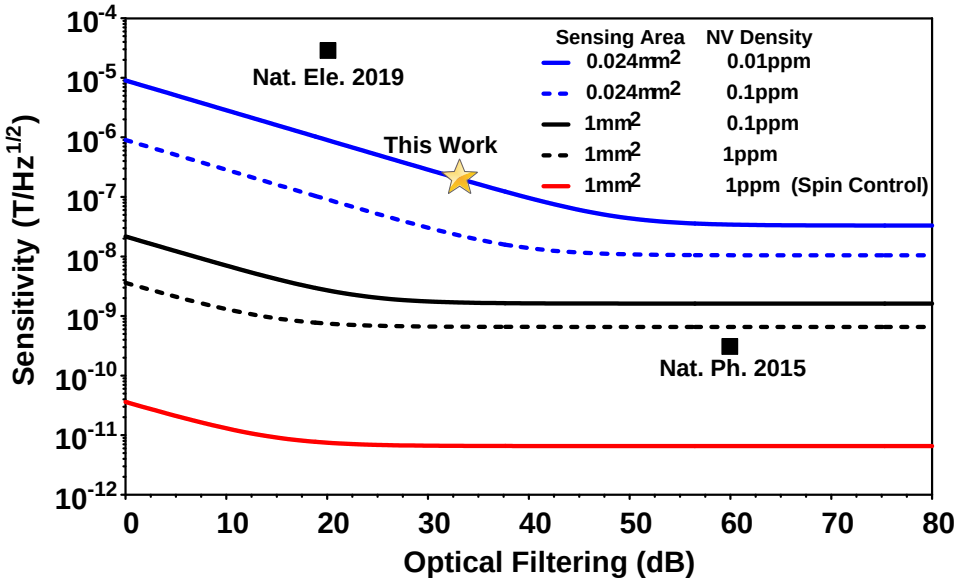

Figure 5-19: Estimation of sensitivity for hybrid CMOS-NV magnetometers with different configurations.

5b) can lead to higher magnetic homogeneity over a larger proportion of the total launcher area. For example, we find that if each Group D consists of m=4 wires (d=4 μm) with I_D=6.35 mA, and a gap of 12 μm exists between Group D and Group A/C, 95% magnetic homogeneity was achieved for the entire -60 to 60-μm space above Group A-B-C. Homogeneity over large space also promises a significant sensitivity enhancement via spin-controlled pulse sequence [16]. Lastly, the ability to manipulate the NV centers over a larger area also enables the integration of larger numbers of detectors for gradient magnetometry, multiplexed analytical NMR spectroscopy[67], atomic gyroscopes[95], and other quantum-sensing applications [44].

Chapter 6

Related Works

This thesis focuses primarily on developing S^3IC systems. Tangential to this effort, three projects were completed. The first integrated NVND ensembles within functionalized fibre. Using the model developed in Chapter 3, we used NVNDs for distributed magnetometry[122]. The fibre integration of optoelectronic and solid-state spin devices produced a rugged and waterproof quantum-enhanced sensing platform. The second project developed the surface functionalization of nanodiamonds[176]. This work developed a coating, micellization, and delivery strategy that causes the membranes of neurons to be covered with nanodiamonds. Both projects used NV centers hosted in NVND ensembles to expand the functionality of NV sensing. The final project was an internship at MIT Lincoln Laboratory where I constructed an improved version of the optical microscope shown in Section 2.2.

The first project oversaw the integration of NVND ensembles within functionalized fibre[122]. While NV centers have been used for remote detection of ferrous metals, geophysics, and biosensing, their development into fieldable devices has been limited due to their need to combine optical, microwave, and spin-readout into a single system. Existing approaches have yielded localized devices without distributed capabilities. This work reports a continuous system-in-a-fibre architecture that enables distributed magnetic sensing over extended lengths. Key to this realization was a thermally drawn fibre that had hundreds of embedded photodiodes connected in parallel and a hollow optical waveguide that contained a fluid full of NVNDs. This fibre was placed in a

larger coaxial cable to deliver the required MW excitation. This distributed quantum sensor was realized in a water-immersible 90-m-long cable with 102 detection sites. A sensitivity of 63 $\pm$ 5 nT/$\sqrt{\text{Hz}}$ per site, limited by laser shot noise, was established along a 90 m test section. This fibre architecture opens new possibilities as a robust and scalable platform for distributed quantum sensing technologies.

The second project studied the surface chemistry of nanodiamonds to avoid agglomeration on top of cell membranes[176]. While nanodiamonds are a promising tool for a range of biologically relevant nanoscale sensing applications–thermometry[110], pH sensing[144], and electric[48, 36, 100] and magnetic field sensing[127, 12, 70, 96, 66, 182]–their use in making actual biological discoveries has been limited. This failure is partly due to their agglomeration in physiological conditions and challenges with their delivery to cell surfaces. This work addresses both of these conditions through nanodiamond surface functionalization. We developed a coating, micellization, and delivery strategy that causes the membranes of neurons to be equipped with nanodiamonds and show via electron microscopy, optical microscopy, and cell health assays that the nanodiamonds thus functionalized stay on membranes without adversely affecting cell health. In contrast, commercially available nanodiamonds aggregate and undergo other processes (e.g., endocytosis) that limits their functionality as enduring reporters of membrane signaling. Given its simplicity, we expect our method to be readily applicable to other cell types, as well as other nanoparticle sensing platforms that require single particles be delivered to cell membranes.

6.1 Distributed Quantum Fibre Magnetometry

Current distributed fibre sensors have high sensitivity to temperature[15, 204], strain[24, 132, 218], and pressure[114, 216, 208] – but not to magnetic fields[42, 179, 41]. This work adds spin-based quantum magnetometry to the sensing capabilities of distributed fibre sensors through the integration of NV ensembles. Recent advances toward component integration have achieved magnetometry point probes consisting of micro-diamonds on fibre facets[56] or nanodiamonds on tapered fibres[116]. How-

ever, practical devices will require compact and stable architectures and – for some applications – distributed sensor arrays for magnetometry. Here we introduce an NV-based fibre magnetometer composed of hollow-core silica fibre, drawn with a functional cladding containing the necessary electronics for ODMR magnetometry[122]. We likewise use the fibre as a delivery mechanism for the pump field[172], allowing spin polarization and readout, while extending component integration by having the fibre serve as a backbone for photodetection and microwave spin control.

The fibre preform structure, fabrication process, and schematic are described in Reference [122] and is summarized below. First, we draw a hollow-core silica fibre (index 1.46) through a high-temperature draw tower. Then we embedded a series of tightly packed photodiode (PD) chips in a polycarbonate (PC) cladding. During our next thermal draw, we insert two copper wires and a hollow-core silica fibre, prepared in advance, through holes in the PC. To achieve the required dimensions of the final device, we controlled the feed and draw speed of the PC. The cable assembly was completed by inserting the fibre into a notched coaxial cable. The completed cable spool was 90 m long. The schematic of the microfluidic system allows distributed long-range magnetometry as described below. The system was composed of a 532 nm laser source coupled to a hollow-core silica waveguide. A notched coaxial cable waveguides the required microwave fields to control the NV's spin state, producing ODMR. The fibre contains periodically spaced sensing modules (average spacing of 17 cm) to measure the magnetic field magnitude $|B(s)|$ at a distance s along the fibre. The 532 nm excitation field required for ODMR was guided in the silica shell. We scanned a NV-micro-diamond droplet with air pressure supplied at the back end of the fibre. When the droplet was aligned with one of the embedded PDs, the red NV fluorescence was detected from the green pump background using a lock-in technique. The PDs were connected in parallel through two fibre-embedded copper wires[159]. The surrounding coaxial cable[122] drove the NV spin resonance for ODMR. The embedded PDs collected the emitted NV fluorescence, and the generated photocurrent was measured using a centralized readout bus located at the end of the fibre.

Using the analysis of NVND ensembles presented in Chapter 3, we measured a

sensitivity of 63 ± 5 nT/$\sqrt{\text{Hz}}$ when accounting for the 100 ms time constant and the 0.78 Hz ENBW of the lock-in amplifier (24 dB/oct roll-off). To showcase the distributed quantum magnetometry capabilities of our device, we deployed it down a 70 m corridor. We measured the magnetic field at 102 points along the corridor. We observed a spike in the magnetic field of ∼180 μT at the location of Airgas cylinders. We also used the unique distributed nature of our fibre magnetometer to localize and quantify a magnetic source in space. A magnet cube (3x3x3 mm) was placed 1.3 cm away from the fibre, and we aligned it to the fibre so that adjacent sensing modules were 3, 2.2, 5.7, and 3 cm apart. Determining the applied magnetic field at each node gave the magnetic field distribution along the fibre. Modeling the applied magnetic field as a magnetic dipole allowed us to determine the location, orientation, and magnitude of the magnetic object[122]. For example, we determined the axial and radial position with an accuracy of 1.87 and 2.87 mm, respectively.

We estimate that an additional order of magnitude improvement in sensitivity is possible by improving green filtering by ∼20 dB. Two possible solutions to filter the green light are inserting a thin free-space optical filter within the cladding or modifying the cladding to have a photonic Bragg grating layer[184]. The noise would then be dominated by the shot noise from the NV centers. The SNR could also be improved by increasing the total amount of collected NV fluorescence, as shown in bulk diamond NV ensemble magnetometers, which have recently demonstrated a sensitivity of pT/$\sqrt{\text{Hz}}$ for DC magnetometry[213, 39, 16]. Additional improvement could be achieved by using NV centers with improved spin coherence[197, 127, 56, 14].

In conclusion, we have demonstrated a distributed fully-integrated magnetic field sensor that enables localization and quantification of magnetic fields along a hundred meter-scale length with a sensitivity of 63 nT/$\sqrt{\text{Hz}}$ and a spatial resolution of 17 cm. Such a distributed water-immersible quantum fibre magnetometer promises new applications for remote detection and tracking in a range of fields including geophysics, ferrous metal detection, and biomedical sensing.

6.2 Membrane-targeted Delivery of Nitrogen-Vacancy Nanodiamonds

My primary contribution to this work was performing ODMR measurements on labeled neurons. The goal of the experiment was to determine if silanized nanodiamonds (Si-NVNDs) or hydroxyl-terminated nanodiamonds (OH-NVNDs) were better for precise targeting of membranes without significant agglomeration. Previous work has focused on OH-NVNDs with cellular delivery occurring through endocytosis[85, 134]. However, this method has demonstrated agglomeration which hampers neurite growth[84]. Thus in this work, we focused on staining neural membranes with both Si-NVNDs and OH-NVNDs. We started with commercial nanodiamonds (Adámas Nanotechnologies, made via the high-pressure-high temperature method) and silanized them producing a hydrophobic shell. They were then encapsulated in PEG350-PE micelles, dispersed in physiological buffer, and subsequently incubated with primary neurons for a few minutes, and washed. Finally, the samples were imaged by optical microscopy, as detailed below.

We performed optical confocal microscopy of neurons stained by each of these kinds of functionalized NVNDs. We used a membrane stain (WGA-488) to show whether NVNDs were internalized into the neural cytosol or stayed on the cell membrane (with the caveat that our resolution was limited by optical diffraction). This co-labeling allowed us to estimate the fraction of NVNDs on the membrane vs. inside the cell. We found a significantly higher percentage of Si-NVNDs than OH-NVNDs on the membrane, for both NVNDs with mean diameters of 100 nm and 40 nm[176].

The previous experiments were done using confocal microscopy. To verify that the red fluorescent spots in these confocal microscopy studies indeed originated from NVNDs, we performed ODMR. We found NV resonant frequencies for both 100 nm and 40 nm Si-NVNDs delivered to neurons[176]. The measured ODMR spectra originating from the fluorescent locations show that these fluorescent labels were indeed NVNDs.

6.3 Constructing a Spin Microscope at MIT Lincoln Laboratories

From May 2019 to January 2020, I worked at MIT Lincoln Laboratories. The goal was to develop a spin microscope optimized for large field of view (4 mm x 4 mm), high frame rate, and sensitivity. This setup combined three advantages found within MIT LL's quantum sensing group: highly uniform MW field delivery over large areas [54, 99], their optimized diamond growth, and propriety MIT LL camera technology, the digital focal plane array (DFPA). This camera offers both very large electron well depth and dynamical programming of the camera. This programming allows for on-chip lock-in detection of NV fluorescence. Both of these features are highly advantageous for wide-field imager setups. This spin microscope should have very high sensitivity capable of implementing advanced dynamical decoupling sequences on NV centers across the FOV. This device should have broad utility in fields ranging from microelectronics reliability studies, modeling chemical reactions, to the biological sciences.

Chapter 7

Outlook and Closing Thoughts

7.1 Conclusion

This dissertation has presented my seven years of research at MIT. Over that time the NV community has rapidly advanced the state-of-the-art of the field. NV centers have progressed from original platform demonstrations[68] to fully realized commercial devices[153]. Massive flagship government-funding programs[1] further illustrate this increasing interest. Over the coming years I imagine that the application space of NV sensing generally, and S^3IC particularly, will continue to expand with new frontiers of development and integration.

Chapter 3 presents Q-CAT imaging. We extended the ODMR model for NV centers developed in chapter 2 to NVNDs, building on the works shown in Ref. [81, 128]. We also performed statistical characterization of NVND properties in regards to generating MT images. We emphasized the applicability of Q-CAT imaging by using it on a variety of material systems of increasing electro-thermal physics complexity, with particular emphasis on GaN HEMTs. This system showcases wide-field measurements with a field of view greater than 100 μm x 100 μm, compatibility with standard microscopes, can be applied to many materials, and a mean thermal sensitivity comparable to micro-Raman spectroscopy and IR microscopy. This work highlights S^3IC as a diagnostic tool to improve ICs.

Chapters 4 and 5 demonstrate chip-scale quantum magnetometry by integrating

spin systems with CMOS technology - S^3IC. We integrated the essential components to detect NV-ODMR: a microwave generator, an inductor, an optical pump beam filter, and a PD. The microwave launcher we present provided better than 95% uniformity with a scalable design. The on-chip optical filter provided better than 25 dB suppression of the green pump through both a plasmonic and Talbot filter. Ultimately the performance of the chip, 245 $nT/Hz^{1/2}$, was limited by green shot noise of our pump - indicating that further improvements in green filtering are necessary to reach NV fluorescence shot-noise limited performance. In addition, using a diamond waveguide geometry[39] – possibly with a higher NV density[2] (0.01 ppm to 10 ppm) – should increase the SNR by orders of magnitudes. In addition, dynamical decoupling sequences[188, 44] can improve the sensitivity by a few orders of magnitude for measuring magnetic fields at frequencies above the NV decoherence rate. The scalable architectures and component designs presented provide a clear pathway to further push the proposed sensor to sub-$nT/Hz^{1/2}$ sensitivities.

7.2 Outlook

Q-CAT imaging is a powerful technique for MT imaging. Three possible improvements in the platform are improving the primary figures of merit, the magnetic and temperature sensitivity, decreasing the variance in the thermal response of the NVNDs, and expanding the functionality of the platform. The sensitivity could be improved by using NVNDs possessing coherence times approaching what has been demonstrated with bulk diamond[14, 197] or by using dynamical decoupling pulse sequences[188]. We estimate that $mK/\sqrt{Hz}$[110] temperature precision and sub $nT/\sqrt{Hz}$[14] magnetic field sensitivity are achievable with Q-CAT imaging. Improving the nanodiamond fabrication and delivery would decrease the variation in NVND thermal response. This variation needs to be significantly smaller than the temperature sensitivity so that precision is limited by experimental noise. The final improvement is expanding the functionality of this technique. The unique method of NVND deposition enables the imaging of non-planar geometries, perhaps allowing the

imaging of vertical sidewalls. Also, the temporal resolution of this technique could be extended for periodic signals through stroboscopic imaging, in which the laser readout for the NVNDs is pulsed in sync with the application of the electric current. In this manner, a temporal resolution of 10 ns could be achieved, which is limited by the laser gating time. This application could be of interest in studying the transient MT behavior of microelectronic devices, such as the peak temperature of GaN HEMTs at MHz frequencies. Studying GaN HEMTs at this operating frequency is crucial for constructing high efficiency power converters. Finally, the ability to image the magnetic field across an electrical device could be useful in device verification studies and preventing hardware Trojan attacks[25].

The hybrid NV-CMOS quantum magnetometers shown in Chapters 4 - 5 are incomplete. There are additional components that should be integrated and capabilities that need to be demonstrated. For example additional MW frequencies could be implemented to allow for double quantum magnetometry, reducing common mode noise. We note that the CMOS-integration of all currently off-chip electronic components, such as the TIA and the lock-in amplifier, has been demonstrated in prior research[207] and would simplify the experiment. One component not presently integrated into our diamond-CMOS platform is the pump laser for NV optical excitation. This optical pump can be integrated into our platform through using a chip-scale laser diode[137], green Vertical-Cavity Surface-Emitting Lasers[101], or CMOS-compatible waveguided delivery of the optical pump beam[129]. Alternatively, dispersive cavity readout [55] offers an alternative readout mechanism with the possibility to reach the NV spin-projection limit ($\sim$ 50 fT/$\sqrt{\text{Hz}}$). This readout mechanism is especially attractive because it eliminates the need to filter out the green pump - the primary limitation currently.

There are a variety of magnetometers currently available. For example SQUID magnetometers have demonstrated fT/$\sqrt{\text{Hz}}$ sensitivities[51] but require cryogenic temperatures and are thus not widely used. CMOS-compatible magnetometer in contrast are widely integrated throughout commercial electronic devices. There are fluxgate, anisotropic magnetoresitance (AMR or GMR), and Hall effect (HE) sen-

sors. In particular, AMR and HE sensors have dominated the commercial market for decades[72]. HE sensors are cheaper than AMR sensors with relatively poor sensitivity (10 nT/$\sqrt{\text{Hz}}$) but larger operating range. AMR sensors, in contrast, are significantly more sensitive (200 pT/$\sqrt{\text{Hz}}$)[72]. Interestingly, SERF magnetometers have recently been miniaturised into commercial devices [201, 154]. These devices demonstrate improved sensitivities (200 fT/$\sqrt{\text{Hz}}$) compared to AMR or HE sensors, though are significantly more expensive ($\sim$ \$9000). Thus, the NV-CMOS hybrid platform shown in this thesis has much potential as a commercial device because it combines the advantages of CMOS (cheap, scalable) with NV centers (sensitive, high bandwidth, large operating range, vector sensing capability). We estimate that a sensitivity of $\sim$ pT/$\sqrt{\text{Hz}}$ is possible with this platform using conventional optical readout.

The ability to manipulate NV centers on-chip enables a variety of applications. Possible applications include parallel readout of an entire magnetic field spectrum (magnetic spectrometer). NV ensemble sensing over a larger area also enables the integration of more PDs for gradient magnetometry with applications toward navigation in a GPS denied environment; multiplexed NMR spectroscopy[67], atomic gyroscopes[95]; and other quantum-sensing applications[44]. In addition to chip-scale quantum sensing capability, our CMOS-based spin control and readout scheme will provide a uniquely scalable solution for implementing spin quantum-bit controls. This platform is particularly essential to develop a large-scale quantum information processor[217, 203, 33, 143], which enables quantum enhanced sensing[63, 202, 44] and quantum information processing [23, 147, 86].

7.3 Closing Thoughts

When I started doing research at MIT, I could not imagine the exciting possibilities that the NV platform would offer. I began with constructing simple optical setups. That work continually increased in complexity, both in breadth and depth of scientific thought, culminating in interdisciplinary projects staffed with experts in various

technologies and processes such as neurons, CMOS chips, GaN HEMTs, and optical fibre. Thus, while this dissertation concludes my work on NV centers at MIT, I believe that S^3ICs will continue to impact the future scientific directions of NV-based sensing platforms. It really is just the end of the beginning for NV centers, with the only limit on applications being creativity.

Appendix A

Derivation of Q-CAT Fitting Model

We can derive an analytical expression for the expected ODMR spectrum by extending the derivation for an NV within an optical trap[81]. This means determining the ODMR curve's lineshape around each NV resonance as a function of f, $\delta\nu$, and C, where f is the microwave frequency, $\delta\nu$ is the linewidth of the Lorentzians[50] seen in Figure 2-2, and C is the NV's contrast - the normalized change in fluorescence rate between the $|m_s = \pm 1\rangle$ and $|m_s = 0\rangle$ states.

In order to determine information about the NV's local environment, we must first fit the NV's ODMR curve, $I(f; \epsilon, \delta\nu, C)$, to determine both T and B_z. The functional form of $I(f; \epsilon, \delta\nu, C)$ is used to fit the ODMR curves shown in Figure 1 of the main text and to construct the temperature and magnetic field images shown in Figures 3-5. $I(f; \epsilon, \delta\nu, C)$ has the form

$$I(f; \epsilon, \delta\nu, C) = \frac{\sum_{i=1}^{N} \sum_{m=1}^{2} r_{im}(f; \epsilon_{im}, \delta\nu, C)}{\sum_{i=1}^{N} \sum_{m=1}^{2} r_{im}(0; \epsilon_{im}, \delta\nu, C)} \tag{A.1}$$

where $r_{im}(0)$ is the NV fluorescence rate at zero microwave frequency, N is the number of NVs, i represent the number of NVs up to N, and m is the two $|m_s = \pm 1\rangle$ spin states. We know that and the relationship between $r(f; \epsilon_{im}, \delta\nu, C)$ and $r_{im}(0)$ is given by[50]

$$r_{im}(f;\epsilon_{im},\delta\nu,C) \approx r(0)_{im}\left(1-\frac{C}{1+\left(\frac{f-\epsilon_{im}}{\delta\nu}\right)^2}\right) \tag{A.2}$$

which simplifies to

$$r_{im}(f;\epsilon_{im},\delta\nu,C) = r(0)_{im}\Big(1-L(f;\epsilon_{im},\delta\nu,C)\Big) \tag{A.3}$$

where $L(f;\epsilon,\delta\nu,C)$ is the three-parameter Lorentzian function. Thus, $I(f;\epsilon_{im},\delta\nu,C)$ becomes

$$I(f;\epsilon,\delta\nu,C) = 1-\frac{\sum_{i=1}^{N}\sum_{m=1}^{2}L(f;\epsilon_{im},\delta\nu,C)}{N} \tag{A.4}$$

in the limit where all NVs emit at the same fluorescence rate, or

$$\sum_{i=1}^{N}\sum_{m=1}^{2}r_{im}(0;\epsilon_{im},\delta\nu,C) = \sum_{i=1}^{N}\sum_{m=1}^{2}r_{im}(0) = Nr_0 \tag{A.5}$$

Equation A.4 is correct for an ODMR spectrum with an integer number of N and uniform collection efficiency. NVs located within a diamond lattice have $N = 4$, as shown in Figure A-1a top. A representative ODMR curve originating from all four NV orientations within a diamond lattice under a static magnetic field is shown in Figure A-1b, with the four NVs identified with each of their spin states. NV resonant frequencies are determined by the solution to the Hamiltonian described in the previous section (Equation 2.1). For NVs within nanodiamond (NVND) ensembles, N is very large and this makes Equation A.4 hard to apply.

To modify Equation A.4 in the regime of large N, we observe how NVND ensemble ODMR spectra change as a function of $|B|$. As shown in Figure 1b of the main text, as N increases the ODMR curve broadens. We make the following assumption that $N = \infty$ and is isotropically distributed. This model is shown in Figure A-1a bottom. Figure A-1c shows a fluorescence image of deposited Adámas nanodiamonds. The boxed nanodiamond gives the ODMR spectra shown in Figure A-1d as a function of magnetic field. This broadening is very different than what is observed in Figure A-1b, and this motivates the adoption of the isotropic model to explain NVND ODMR

spectra. Thus, this isotropic model has four repercussions: (i) a broadening of the ODMR curve as a function of $|B|$, resulting from the varying B_z across the NV ensemble; (ii) the insensitivity of the NVND ensemble to B_z, as there will always be a maximally aligned NV within the ensemble; (iii) Equation 8 is no longer accurate as the anisotropic collection effiency of the optical system needs to be considered, which results in $r(\theta)_0$- the θ dependent NV fluorescence collection rate; (iv) the distribution in B_z means that the normalized fluorescence of NVNDs increases as a function of $|B|$ to 1.

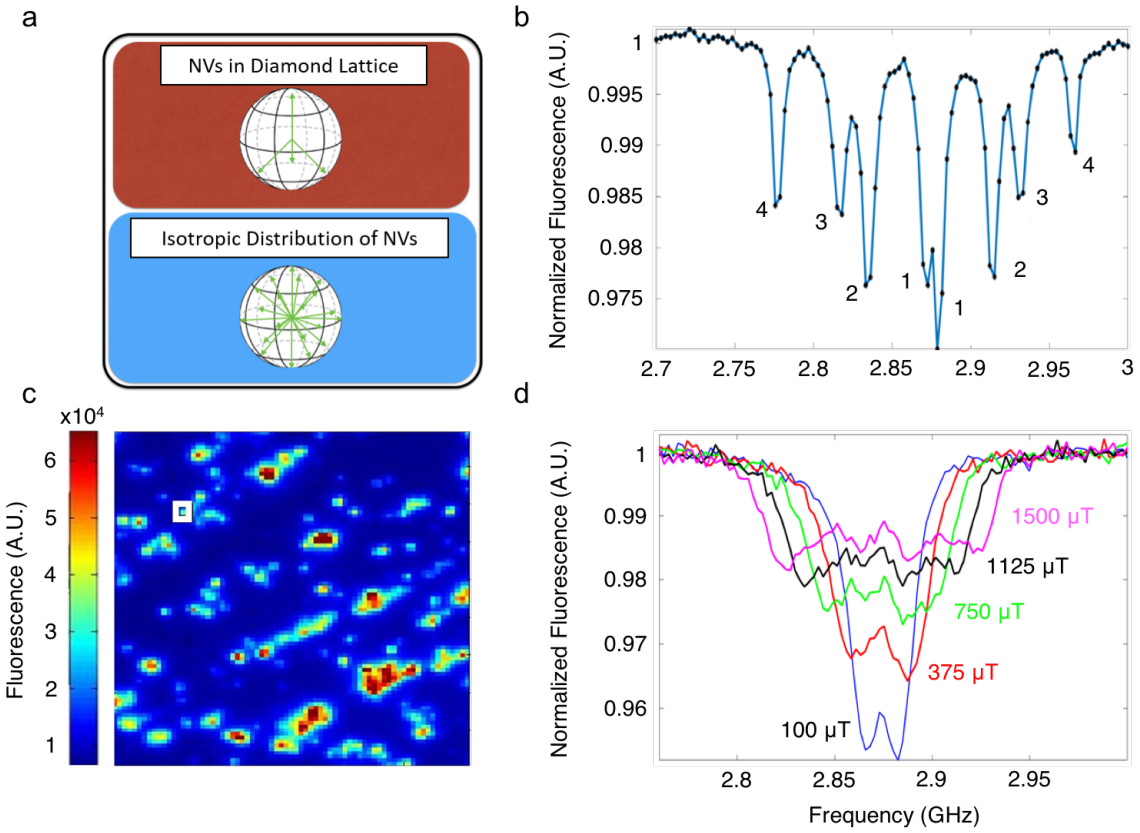

Figure A-1: **Overview of NVND Ensemble Model**. **a**, Different models that explain ODMR spectra. **b**, Representative ODMR curve of NVs in a diamond lattice under a static magnetic field. **c**, Fluorescence image of deposited nanodiamonds with one NVND boxed. **d**, ODMR spectra of boxed NVND as a function of magnetic field.

With the assumption that NV orientations are isotropically distributed, we modify Equation A.5 by integrating around the unit sphere. To simplify the calculation, we make the approximation that the driving microwave field affects all NV orientations

equally.

$$1 - I(f;\epsilon,\delta\nu,C) \propto \int_0^{\pi} \sum_{m=1}^{2} R(\theta) L(f;\epsilon_{\theta m},\delta\nu,C) sin(\theta) d\theta \tag{A.6}$$

where $R(\theta)$ represents the angular dependent weighting of the normalized fluorescence value r_0, which originates from the invalidation of Equation 7. The sum for both the $|m_s = \pm 1\rangle$ spin states remains inside the integral, and we have integrated about ϕ. The lack of ϕ dependence on $R(\theta)$ is due to the symmetry of the optical collection around ϕ. Inserting the dependence of T and $|B|$ explicitly, Equation A.5 becomes

$$1 - I(f;T,|B|,\delta\nu,C) \propto$$
$$\int_0^{\pi} \left(\frac{R(\theta)C}{1 + \left(\frac{f - \left(D(T) + \sqrt{E^2 + \left(\gamma B_z(\theta)\right)^2} \right)}{\delta\nu} \right)^2} + \frac{R(\theta)C}{1 + \left(\frac{f - \left(D(T) - \sqrt{E^2 + \left(\gamma B_z(\theta)\right)^2} \right)}{\delta\nu} \right)^2} \right) sin(\theta) d\theta \tag{A.7}$$

To use Equation A.7, $R(\theta)$ still needs to be determined. The form of $R(\theta)$ will depend on the numerical aperture (NA) of the experiment's objective, because the objective will collect less light from NVs at oblique angles to it. For most of the data shown in this work, NV fluorescence was collected using a 50X long working distance objective with a NA of 0.55. We will determine $R(\theta)$ for this NA, as a representative sample.

A.1 Solving for $R(\theta)$

To determine $I(f;T,|B|,\delta\nu,C)$, we assume that the NVs within a nanodiamond are isotropically distributed. However, this assumption does not account for the anisotropic collection efficiency of our optical system. This angular dependence is represented in parameter $R(\theta)$. $R(\theta)$ depends on several parameters: microwave strength, the amount of light absorbed by the NV, and the amount of collected light

emitted. Since we assume that $\delta\nu$ is constant for all NV orientations (to simplify the calculation), only the angular dependence of the absorption and collection efficiency is considered. Thus,

$$R(\theta) \propto \zeta(\theta) * CE(\theta) \tag{A.8}$$

where $\zeta(\theta)$ is the angular dependence of the NV's absorption and $CE(\theta)$ is the angular dependence of the optical system's collection efficiency.

A.1.1 Determining $\zeta(\theta)$

To calculate $\zeta(\theta)$, we first model the NV as a classical dipole. The absorption from a single transition dipole is proportional to $\left|\vec{p}\cdot\vec{E}\right|^2$, where $\vec{p}$ is the associated dipole moment and $\vec{E}$ is the electric field vector of the excitation beam. We assume that $\vec{E}$ is perpendicular to the objective axis, $\hat{z}$, and thus has the form $\vec{E} = E_x\hat{x} + E_y\hat{y}$. The coordinate system is shown in Figure A-2. Since the NV has two dipoles[82] , the total absorption is proportional to

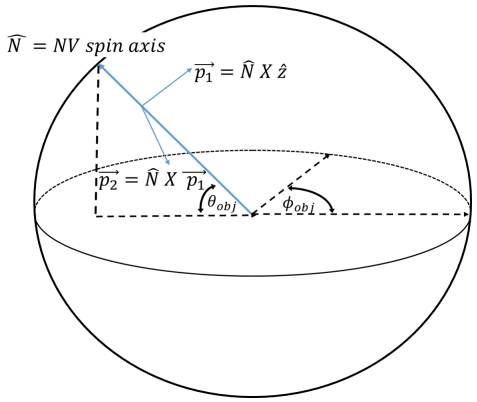

Figure A-2: **Diagram of NV-objective Coordinate System**. Diagram of the coordinate system used to determine $\zeta(\theta)$.

$$\zeta(\theta) \propto \left|\vec{p_1}\cdot\vec{E}\right|^2 + \left|\vec{p_2}\cdot\vec{E}\right|^2 \tag{A.9}$$

Without loss of generality to the final functional form of $\zeta(\theta)$, we can define the dipole directions, $\vec{p_1}$ and $\vec{p_2}$, as

$$\vec{p_1} = p_1 \hat{N} \times \hat{z} \tag{A.10}$$

$$\vec{p_2} = p_2 \hat{N} \times \hat{p_1} \tag{A.11}$$

where $\hat{N}$ is the direction of the NV axis given by

$$\hat{N} = \sin\theta\cos\phi\hat{x} + \sin\theta\sin\phi\hat{y} + \cos\theta\hat{z} \tag{A.12}$$

We define θ as the polar angle and ϕ as the azimuthal angle defined from the origin of the NV. Thus,

$$\vec{p_1} = p_1(\sin\theta\sin\phi\hat{x} - \sin\theta\cos\phi\hat{y}) \tag{A.13}$$

The absorption due to the first dipole is

$$\zeta(\theta,\phi)_{p_1} \propto p_1^2(E_x\sin\theta\sin\phi - E_y\sin\theta\cos\phi)^2 \tag{A.14}$$

We next integrate $\zeta(\theta,\phi)$ over ϕ and get

$$\zeta(\theta)_{p_1} \propto p_1^2\pi(E_x^2 + E_y^2)\sin^2(\theta) \tag{A.15}$$

Similarly, $\vec{p_2}$ becomes

$$\vec{p_2} = p_2(\sin\theta\cos\theta\cos\phi\hat{x} + \sin\theta\cos\theta\sin\phi\hat{y} - (\sin^2\theta\cos^2\phi + \sin^2\theta\sin^2\phi)\hat{z}) \tag{A.16}$$

Thus, the absorption from the second dipole is proportional to

$$\zeta(\theta)_{p_2} \propto p_2^2\pi\sin^2\theta\cos^2\theta(E_x^2 + E_y^2) \tag{A.17}$$

where we again integrate over ϕ. Hence, the total NV absorption is

$$\zeta(\theta,\phi)_{total} \propto \zeta(\theta)_{p_1} + \zeta(\theta)_{p_2} = p_1^2\pi(E_x^2 + E_y^2)\sin^2\theta + p_2^2\pi\sin^2\theta\cos^2\theta(E_x^2 + E_y^2) \tag{A.18}$$

From symmetry we know that $p_1 = p_2$ and $|E|^2 = E_x^2 + E_y^2$. Thus,

$$\zeta(\theta,\phi)_{total} \propto p_1^2\pi(|E|^2)\sin^2\theta(1+\cos^2\theta) \propto 1 - \cos^4\theta \tag{A.19}$$

A.1.2 Determining CE(θ)

We calculate $CE(\theta)$ by treating the NV's dipole moments classically. The power radiated by both NV dipoles is given by

$$\langle P_{total}\rangle = \langle P_1\rangle + \langle P_2\rangle \tag{A.20}$$

where each dipoles power is given by

$$\langle P\rangle \propto |p_\perp|^2 \tag{A.21}$$

where $p_\perp$ is given by

$$p_\perp = \vec{p} - \hat{r}(\hat{r}\cdot\vec{p}) \tag{A.22}$$

and $\vec{p}$ is given by

$$\vec{p} = p_x\hat{x} + p_y\hat{y} + p_z\hat{z} \tag{A.23}$$

Here we define the origin of our coordinate system from our objective axis, as shown in Figure A-3, with the NV frame aligned with the objective. Thus, $\hat{r}$ becomes

$$\hat{r} = \sin\theta_{obj}\cos\phi_{obj}\hat{x} + \sin\theta_{obj}\sin\phi_{obj}\hat{y} + \cos\theta_{obj}\hat{z} \tag{A.24}$$

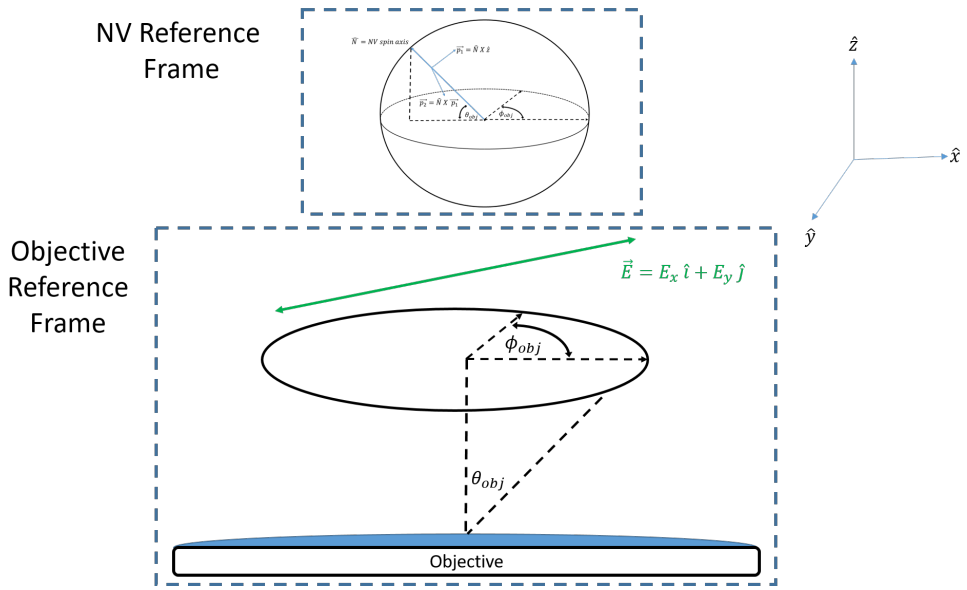

Figure A-3: **Schematic of Objective Reference Frame**. Objective reference frame shown with respect to NV reference frame.

Solving for each component of $p_\perp$ gives

$$p_{\perp_{\hat{x}}} = p_x(1-\sin^2\theta_{obj}\cos^2\phi_{obj}) - p_y\sin^2\theta_{obj}\sin\phi_{obj}\cos\phi_{obj} - p_z\sin\theta_{obj}\cos\phi_{obj}\cos\theta_{obj} \tag{A.25}$$

$$p_{\perp_{\hat{y}}} = p_y(1-\sin^2\theta_{obj}\sin^2\phi_{obj}) - p_x\sin^2\theta_{obj}\sin\phi_{obj}\cos\phi_{obj} - p_z\sin\theta_{obj}\sin\phi_{obj}\cos\theta_{obj} \tag{A.26}$$

$$p_{\perp_{\hat{z}}} = p_z(1-\cos^2\theta_{obj}) - p_x\sin\theta_{obj}\cos\theta_{obj}\cos\phi_{obj} - p_y\sin\theta_{obj}\sin\phi_{obj}\cos\theta_{obj} \tag{A.27}$$

Equations A.25-A.27 are true for both NV dipoles. To solve for $p_{\perp_1}$ and $p_{\perp_2}$, we need to plug in p_x, p_y, and p_z for each of the dipoles. Comparing Equations A.24 and A.14, we see that the components for p_1 are

$$p_{x_1} = p_1\sin\theta\sin\phi \tag{A.28}$$

$$p_{y_1} = -p_1 \sin\theta \cos\phi \tag{A.29}$$

$$p_{z_1} = 0 \tag{A.30}$$

To solve Equations A.25-A.27 for p_1 we use Equation A.23 with the following relation given by observing Figure A-3. We see that $\theta_{obj} = -\theta$ and $\phi_{obj} = \phi$. These give

$$p_{\perp_x}^2 = (p_1 \sin\theta \sin\phi)^2 \tag{A.31}$$

$$p_{\perp_y}^2 = (-p_1 \sin\theta \cos\phi)^2 \tag{A.32}$$

$$p_{\perp_z}^2 = 0 \tag{A.33}$$

To get $\langle P_1 \rangle$, we need to integrate $p_\perp(\theta, \phi)^2$ about θ and ϕ. Thus,

$$\langle P_1 \rangle \propto \int_0^{\theta_{max}} \int_0^{2\pi} p_{\perp_1}^2 \sin\theta d\theta d\phi = \int_0^{\theta_{max}} \int_0^{2\pi} (p_{\perp_x}^2 + p_{\perp_y}^2 + p_{\perp_z}^2) \sin\theta d\theta d\phi \tag{A.34}$$

where θ_{max} is the maximum collection angle determined by the NA of the objective. Thus, θ_{max} is given by

$$n \sin\theta_{max} = NA \tag{A.35}$$

$$\theta_{max} = \sin^{-1}(NA/n) \tag{A.36}$$

where n is the index of refraction of air. Thus, $\langle P_1 \rangle$ is

$$\langle P_1 \rangle \simeq 1.04 \sin^2\theta \tag{A.37}$$

Similarly, for $\langle P_2 \rangle$ we have

$$\langle P_2 \rangle \simeq 0.12\sin^4\theta + 0.3\sin^3\theta\cos\theta + 0.45\sin^2\theta\cos^2\theta - 0.02\sin^2\theta\cos\theta + 0.06\cos\theta\sin\theta - 0.47\cos^2\theta \quad \text{(A.38)}$$

Thus,

$$\langle P_{total} \rangle \simeq 1.04\sin^2\theta + 0.12\sin^4\theta + 0.3\sin^3\theta\cos\theta + 0.45\sin^2\theta\cos^2\theta - 0.02\sin^2\theta\cos\theta + 0.06\cos\theta\sin\theta - 0.47\cos^2\theta \quad \text{(A.39)}$$

We treat $\langle P_{total} \rangle \propto CE(\theta)$. Thus,

$$R(\theta) \propto (1-\cos^4\theta)(1.04\sin^2\theta + 0.12\sin^4\theta + 0.3\sin^3\theta\cos\theta + 0.45\sin^2\theta\cos^2\theta - 0.02\sin^2\theta\cos\theta + 0.06\cos\theta\sin\theta - 0.47\cos^2\theta) \quad \text{(A.40)}$$

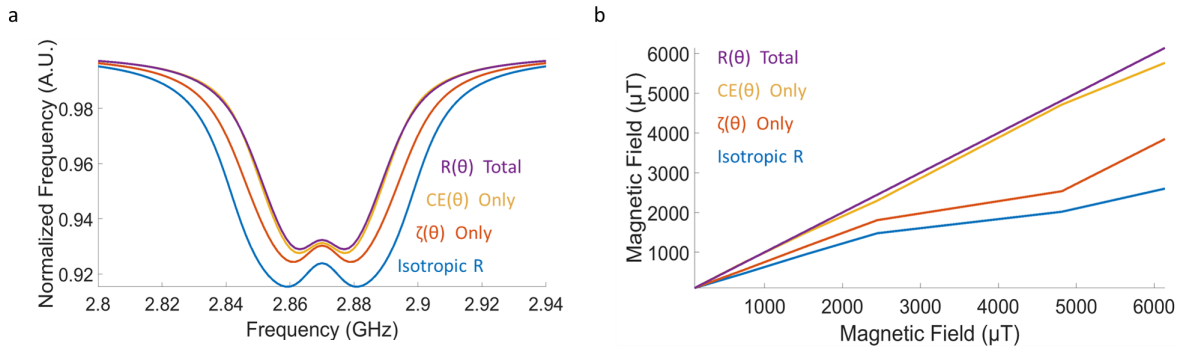

Figure A-4: **Comparison of Different** $R(\theta)$. **a**, NVND ODMR as a function of different $R(\theta)$ **b**, $|B|$ measurement for same data with different $R(\theta)$ models.

The different versions of $R(\theta)$ are shown in Figure A-4. Figure A-4a shows how treating R as a constant independent of θ means that orientations that would couple best to the external magnetic field are not suppressed. The result of this is shown in Figure A-4b, where a smaller magnetic field is measured than what is expected. This effect will be minimized for optical systems with larger NA.

Bibliography

[1] Antonio Acín, Immanuel Bloch, Harry Buhrman, Tommaso Calarco, Christopher Eichler, Jens Eisert, Daniel Esteve, Nicolas Gisin, Steffen J Glaser, Fedor Jelezko, Stefan Kuhr, Maciej Lewenstein, Max F Riedel, Piet O Schmidt, Rob Thew, Andreas Wallraff, Ian Walmsley, and Frank K Wilhelm. The quantum technologies roadmap: a european community view. *New Journal of Physics*, 20(8):080201, 2018.

[2] V. M. Acosta, E. Bauch, M. P. Ledbetter, C. Santori, K.-M. C. Fu, P. E. Barclay, R. G. Beausoleil, H. Linget, J. F. Roch, F. Treussart, S. Chemerisov, W. Gawlik, and D. Budker. Diamonds with a high density of nitrogen-vacancy centers for magnetometry applications. *Phys. Rev. B*, 80:115202, Sep 2009.

[3] V.M. Acosta, E. Bauch, M.P. Ledbetter, A. Waxman, L.-S. Bouchard, and D. Budker. Temperature dependence of the nitrogen-vacancy magnetic resonance in diamond. *Physical review letters*, 104(7):070801, 2010.

[4] K. akoubovskii, G. J. Adriaenssens, and M. Nesladek. Photochromism of vacancy-related centres in diamond. *Journal of Physics: Condensed Matter*, 12(2):189, 2000.

[5] Paolo Andrich, Jiajing Li, Xiaoying Liu, F. Joseph Heremans, Paul F. Nealey, and David D. Awschalom. Microscale-resolution thermal mapping using a flexible platform of patterned quantum sensors. *Nano Letters*, 18(8):4684–4690, 2018.

[6] ANSOFT. *High Frequency Structure Simulator (HFSS) User Guide*. ANSYS Inc., 2008.

[7] T. R. Anthony, J. L. Fleischer, J. R. Olson, and David G. Cahill. The thermal conductivity of isotopically enriched polycrystalline diamond films. *J. APPL. PHYS.*, 69(12):8122, 1991.

[8] K. Arai, C. Belthangady, H. Zhang, N. Bar-Gill, S. J. Devience, P. Cappellari, A. Yacoby, and R. L. Walsworth. Fourier magnetic imaging with nanoscale resolution and compressed sensing speed-up using electronic spins in diamond. *Nature Nanotechnology*, 10(10):859–864, 2015.

[9] Silvia Arroyo-Camejo, Marie-Pierre Adam, Mondher Besbes, Jean-Paul Hugonin, Vincent Jacques, Jean-Jacques Greffet, Jean-François Roch, Stefan W. Hell, and François Treussart. Stimulated emission depletion microscopy resolves individual nitrogen vacancy centers in diamond nanocrystals. *ACS Nano*, 7(12):10912–10919, 2013.

[10] Nabeel Aslam, Matthias Pfender, Philipp Neumann, Rolf Reuter, Andrea Zappe, Felipe Fávaro de Oliveira, Andrej Denisenko, Hitoshi Sumiya, Shinobu Onoda, Junichi Isoya, et al. Nanoscale nuclear magnetic resonance with chemical resolution. *Science*, 357(6346):67–71, 2017.

[11] K. R. Bagnall, E. A. Moore, S. C. Badescu, L. Zhang, and E. N. Wang. Simultaneous measurement of temperature, stress, and electric field in Gan Hemts with micro-raman spectroscopy. *Review of Scientific Instruments*, 88(11):113111, 2017.

[12] G. Balasubramanian, I.Y. Chan, R. Kolesov, M. Al-Hmoud, J. Tisler, C. Shin, C. Kim, A. Wojcik, P. R. Hemmer, A. Krueger, T. Hanke, A. Lietenstorfer, R. Bratschitsch, F. Jelezko, and J. Wrachtrup. Nanoscale imaging magnetometry with diamond spins under ambient conditions. *Nature*, 455(7213):648–651, 2008.

[13] G. Balasubramanian, A. Lazariev, S. R. Arumugam, and D. Duan. Nitrogen-Vacancy color center in diamond - emerging nanoscale applications in bioimaging and biosensing. *Current Opinion in Chemical Biology*, 20:69–77, 2014.

[14] G. Balasubramanian, P. Neumann, D. Twitchen, M. Markham, R. Kolesov, N. Mizuochi, J. Isoya, J. Achard, J. Beck, J. Tissler, V. Jacques, P. R. Hemmer, F. Jelezko, and J. Wrachtrup. Ultralong spin coherence time in isotopically engineered diamond. *Nature Materials*, 8(5):383–387, 2009.

[15] X. Bao, D. J. Webb, and D. A. Jackson. 32-km distributed temperature sensor based on brillouin loss in an optical fiber. *Optics Letters*, 18(18):1561–1563, 1993.

[16] John F. Barry, Jennifer M. Schloss, Erik Bauch, Matthew J. Turner, Connor A. Hart, Linh M. Pham, and Ronald L. Walsworth. Sensitivity optimization for nv-diamond magnetometry. *Rev. Mod. Phys.*, 92:015004, Mar 2020.

[17] John F. Barry, Matthew J. Turner, Jennifer M. Schloss, David R. Glenn, Yuyu Song, Mikhail D. Lukin, Hongkun Park, and Ronald L. Walsworth. Optical magnetic detection of single-neuron action potentials using quantum defects in diamond. *Proceedings of the National Academy of Sciences*, 113(49):14133–14138, 2016.

[18] E. Bauch, S. Singh, J. Lee, C. A. Hart, J.M. Schloss, M. J. Turner, J. F. Barry, L. Pham, N. Bar-Gill, S. F. Yelin, and R. L. Walsworth. Decoherence of dipolar spin ensembles in diamond. *ArXiv e-prints*, 2019.

[19] Erik Bauch, Connor A. Hart, Jennifer M. Schloss, Matthew J. Turner, John F. Barry, Pauli Kehayias, Swati Singh, and Ronald L. Walsworth. Ultralong dephasing times in solid-state spin ensembles via quantum control. *Phys. Rev. X*, 8:031025, Jul 2018.

[20] Khadijeh Bayat, Jennifer Choy, Mahdi Farrokh Baroughi, Srujan Meesala, and Marko Loncar. Efficient, Uniform, and Large Area Microwave Magnetic Coupling to NV Centers in Diamond Using Double Split-Ring Resonators. *ACS: Nano Letters*, 14:1208–1213, 2014.

[21] T. Beechem, A. Christensen, S. Graham, and D. Green. Micro-raman thermometry in the presence of complex stresses in gan devices. *Journal of Applied Physics*, 103(12):124501, 2008.

[22] S. Beer and P. Seitz. Real-time tomographic imaging without x-rays: a smart pixel array with massively parallel signal processing for real-time optical coherence tomography performing close to the physical limits. In *Research in Microelectronics and Electronics, 2005 PhD*, volume 2, pages 135–138, 2005.

[23] Hannes Bernien, Bas Hensen, Wolfgang Pfaff, Gerwin Koolstra, MS Blok, Lucio Robledo, TH Taminiau, Matthew Markham, DJ Twitchen, Lilian Childress, et al. Heralded entanglement between solid-state qubits separated by three metres. *Nature*, 497(7447):86, 2013.

[24] V. Bhatia and A. M. Vengsarkar. Optical fiber long-period grating sensors. *Optics Letters*, 21(9):692–694, 1996.

[25] S. Bhunia, M. S. Hsiao, M. Banga, and S. Narasimhan. Hardware trojan attacks: Threat analysis and countermeasures. *Proceedings of the IEEE*, 102(8):1229–1247, 2014.

[26] J. M. Boss, K. Chang, J. Armijo, K. Cujia, T. Rosskopf, J. R. Maze, and C. L. Degen. One- and two-dimensional nuclear magnetic resonance spectroscopy with a diamond quantum sensor. *Phys. Rev. Lett.*, 116:197601, May 2016.

[27] Jens M Boss, KS Cujia, Jonathan Zopes, and Christian L Degen. Quantum sensing with arbitrary frequency resolution. *Science*, 356(6340):837–840, 2017.

[28] C. D. S. Brites, P. P. Lima, N. J. O. Silva, A. Millán, V. S. Amaral, F. Palacio, and L. D. Carlos. Thermometry at the nanoscale. *Nanoscale*, 4(16):4799–4829, 2012.

[29] D. A. Broadway, N. Dontschuk, A. Tsai, S. E. Lillie, C. T. K. Lew, J. C. McCallum, B. C. Johnson, M. W. Doherty, A. Stacey, L. C. L. Hollenberg, and J. P. Tetienne. Spatial mapping of band bending in semiconductor devices using in situ quantum sensors. *Nature Electronics*, 1(9):502–507, 2018.

[30] Dominik B. Bucher, David R. Glenn, Hongkun Park, Mikhail D. Lukin, and Ronald L. Walsworth. Hyperpolarization-enhanced nmr spectroscopy with femtomole sensitivity using quantum defects in diamond. *ArXiv e-prints*, 2018.

[31] J. Cai, F. Jelezko, M. B. Plenio, and A. Retzker. Diamond-based singlemolecule magnetic resonance spectroscopy. *New Journal of Physics*, 15:013020, 2013.

[32] F. Casola, T. van der Sar, and A. Yacoby. Probing condensed matter physics with magnetometry based on nitrogen-vacancy centres in diamond. *Nature Review Materials*, 3(01):17088, 2017.

[33] Edoardo Charbon, Fabio Sebastiano, Masoud Babaie, Andrei Vladimirescu, Mina Shahmohammadi, Robert Bogdan Staszewski, Harald AR Homulle, Bishnu Patra, Jeroen PG Van Dijk, Rosario M Incandela, et al. 15.5 cryo-cmos circuits and systems for scalable quantum computing. In *Solid-State Circuits Conference (ISSCC), 2017 IEEE International*, pages 264–265. Ieee, 2017.

[34] Georgios Chatzidrosos, Arne Wickenbrock, Lykourgos Bougas, Nathan Leefer, Teng Wu, Kasper Jensen, Yannick Dumeige, and Dmitry Budker. Miniature cavity-enhanced diamond magnetometer. *Physical Review Applied*, 8(4):044019, 2017.

[35] E. H. Chen, O. Gaathon, M. E. Trusheim, and D. Englund. Wide-Field Multispectral Super-Resolution Imaging Using Spin-Dependent Fluorescence in Nanodiamonds. *Nanoletters*, 13(5):2073–2077, 2013.

[36] Edward H Chen, Hannah A Clevenson, Kerry A Johnson, Linh M Pham, Dirk R Englund, Philip R Hemmer, and Danielle A Braje. High-sensitivity spin-based electrometry with an ensemble of nitrogen-vacancy centers in diamond. *Physical Review A*, 95(5):053417, 2017.

[37] S. Chowdhury and U. K. Mishra. Lateral and vertical transistors using the AlGaN/GaN heterostructure. *IEEE Transactions on Electron Devices*, 60(10):3060–3066, 2013.

[38] H. Clevenson, L. M Pham, C. Teale, K. Johnson, D. Englund, and D. Braje. Robust high-dynamic-range vector magnetometry with nitrogen-vacancy centers in diamond. *Applied Physics Letters*, 112(25):252406, 2018.

[39] Hannah Clevenson, Matthew E Trusheim, Carson Teale, Tim Schröder, Danielle Braje, and Dirk Englund. Broadband magnetometry and temperature sensing with a light-trapping diamond waveguide. *Nature Physics*, 11(5):393, 2015.

[40] J. B. Cui, K. Amtmann, J. Ristein, and L. Ley. Noncontact temperature measurements of diamond by raman scattering spectroscopy. *Journal of Applied Physics*, 83(12):7929–7933, 1998.

[41] D. J.and Bibby G. W.and Ross J. N. Dakin, J. P.and Pratt. Distributed optical fibre raman temperature sensor using a semiconductor light source and detector. *Electronic Letters*, 21(13):569–570, 1985.

[42] J. P Dakin. Distributed optical fiber sensors. in distributed and multiplexed fiber optic sensors ii. *International Society for Optics and Photonics*, 1797:76–109, 1993.

[43] C. L. Degen. High-sensitivity diamond magnetometer with nanoscale resolution. *Applied Physics Letters*, 92(24):243111, 2008.

[44] Christian L Degen, F Reinhard, and P Cappellaro. Quantum sensing. *Reviews of modern physics*, 89(3):035002, 2017.

[45] M. W. Doherty, V. M. Acosta, A. Jarmola, M. S. J. Barson, N. B. Manson, D. Budker, and L. C. L. Hollenberg. Temperature shifts of the resonances of the Nv- center in diamond. *Physical Review B*, 90(4):041201, 2014.

[46] M. W. Doherty, N. B. Manson, P. Delaney, F. Jelezko, J. Wrachtrup, and L. C. L. Hollenberg. The nitrogen-vacancy colour centre in diamond. *Physics Reports*, 528(1), 2013.

[47] Marcus W. Doherty, Viktor V. Struzhkin, David A. Simpson, Liam P. McGuinness, Yufei Meng, Alastair Stacey, Timothy J. Karle, Russell J. Hemley, Neil B. Manson, Lloyd C. L. Hollenberg, and Steven Prawer. Electronic properties and metrology applications of the diamond nv^- center under pressure. *Phys. Rev. Lett.*, 112:047601, Jan 2014.

[48] Florian Dolde, Helmut Fedder, Marcus W Doherty, Tobias Nöbauer, Florian Rempp, Gopalakrishnan Balasubramanian, Thomas Wolf, Friedemann Reinhard, Lloyd CL Hollenberg, Fedor Jelezko, et al. Electric-field sensing using single diamond spins. *Nature Physics*, 7(6):459, 2011.

[49] H. Dong, B. Wen, and R. Melnik. Relative importance of grain boundaries and size effects in thermal conductivity of nanocrystalline materials. *Scientific Reports*, 4(7037), 2014.

[50] A. Dréau, M. Lesik, L. Rondin, P. Spinicelli, O. Arcizet, J.-F. Roch, and V. Jacques. Avoiding power broadening in optically detected magnetic resonance of single nv defects for enhanced dc magnetic field sensitivity. *Phys. Rev. B*, 84:195204, Nov 2011.

[51] D. Drung, C. Abmann, J. Beyer, A. Kirste, M. Peters, F. Ruede, and T. Schurig. Highly sensitive and easy-to-use squid sensors. *IEEE Transactions on Applied Superconductivity*, 17(2):699–704, 2007.

[52] Arnaud Dubois. *Handbook of Full-Field Optical Coherence Microscopy:*. Pan Stanford Publishing, 2016.

[53] E. R. Eisenach, J. F. Barry, L. M. Pham, R. G. Rojas, D. R. Englund, and D. A. Braje. Broadband loop gap resonator for nitrogen vacancy centers in diamond. *Review of Scientific Instruments*, 89(9):094705, 2018.

[54] E. R. Eisenach, J. F. Barry, L. M. Pham, R. G. Rojas, D. R. Englund, and D. A. Braje. Broadband loop gap resonator for nitrogen vacancy centers in diamond. *Review of Scientific Instruments*, 89(9):094705, 2018.

[55] Erik R. Eisenach, John F. Barry, Michael F. O'Keeffe, Jennifer M. Schloss, Matthew H. Steinecker, Dirk R. Englund, and Danielle A. Braje. Cavity quantum electrodynamic readout of a solid-state spin sensor. *arXiv:2003.01104 [cond-mat, physics:physics, physics:quant-ph]*, March 2020.

[56] S. M.and Serebryannikov E. E.and Hemmer P.and Scully M. O.and Zheltikov A. M. Fedotov, I. Vand Blakley. High-resolution magnetic field imaging with a nitrogen-vacancy diamond sensor integrated with a photonic-crystal fiber. *Optics Letters*, 41(3):472–475, 2016.

[57] Ilja Fescenko, Andrey Jarmola, Igor Savukov, Pauli Kehayias, Janis Smits, Joshua Damron, Nathaniel Ristoff, Nazanin Mosavian, and Victor M. Acosta. Diamond magnetometer enhanced by ferrite flux concentrators. *arXiv:1911.05070 [cond-mat, physics:physics]*, November 2019.

[58] Christopher Foy, Lenan Zhang, Matthew E. Trusheim, Kevin R. Bagnall, Michael Walsh, Evelyn N. Wang, and Dirk R. Englund. Wide-field magnetic field and temperature imaging using nanoscale quantum sensors. *ArXiv e-prints*, 2019.

[59] C. Fu, H. Lee, K. Chen, T. Lim, H. Wu, P. Lin, P. Wei, P. Tsao, H. Chang, and W. Fann. Characterization and application of single fluorescent nanodiamonds as cellular biomarkers. *Proceedings of the National Academy of Sciences*, 104(3):727–732, 2007.

[60] G. D. Fuchs, V. V. Dobrovitski, R. Hanson, A. Batra, C. D. Weis, T. Schenkel, and D. D. Awschalom. Excited-state spectroscopy using single spin manipulation in diamond. *Phys. Rev. Lett.*, 101:117601, Sep 2008.

[61] T. Gefen, A. Rotem, and Retzker. Overcoming resolution limits with quantum sensing. *Nature Communication*, 10:4992, 2019.

[62] I. Georgescu. Nobel prize 2012: Haroche & wineland. *Nature Physics*, 8(777), 2012.

[63] Vittorio Giovannetti, Seth Lloyd, and Lorenzo Maccone. Advances in quantum metrology. *Nature photonics*, 5(4):222, 2011.

[64] Hall Glauber and Hänsch. Trabesinger, a. nobel prize 2005. *Nature Physics*, 1(930), 2005.

[65] D. R. Glenn, R. R. Fu, D. Kehayias, P. ans Le Sage, E. A. Lima, B.P. Weiss, and R.L. Walsworth. Micrometer-scale magnetic imaging of geological samples using a quantum diamond microscope. *Geochemistry, Geophysics, Geosystems*, 18(8), 2017.

[66] D. R. Glenn, K. Lee, H. Park, R. Weissleder, A. Yacoby, M. D Lukin, H. Lee, R. L Walsworth, and C. B Connolly. Single-cell magnetic imaging using a quantum diamond microscope. *Nature Methods*, 12(8):736–738, 2015.

[67] David R Glenn, Dominik B Bucher, Junghyun Lee, Mikhail D Lukin, Hongkun Park, and Ronald L Walsworth. High-resolution magnetic resonance spectroscopy using a solid-state spin sensor. *Nature*, 555(7696):351, 2018.

[68] M. S. Grinolds, S. Hong, P. Maletinsky, L. Luan, M. D. Lukin, R. L. Walsworth, and A. Yacoby. Nanoscale magnetic imaging of a single electron spin under ambient conditions. *Nature Physics*, 9(4):215–219, 2013.

[69] M. S. Grinolds, M. Warner, K. Degreve, Y. Dovzhenko, L. Thiel, R.L. Walsworth, S. Hong, P. Maletinsky, and A. Yacoby. Subnanometre resolution in three-dimensional magnetic resonance imaging of individual dark spins. *Nature Nanotechnology*, 9(03):279, 2014.

[70] M.S. Grinolds, M. Warner, K. De Greve, Y. Dovzhenko, L. Thiel, R. L. Walsworth, S. Hong, P. Maletinsky, and A. Yacoby. Subnanometre resolution in three-dimensional magnetic resonance imaging of individual dark spins. *Nature Nanotechnology*, 9(4):279–284, 2014.

[71] A. Grosz, M. J. Haji-Sheikh, and S. C. Mukhopadhyay. *High Sensitivity Magnetometers*. Springer, 2017.

[72] A. Grosz, V. Mor, S. Amrusi, I. Faivinov, E. Paperno, and L. Klein. A high-resolution planar hall effect magnetometer for ultra-low frequencies. *IEEE Sensors Journal*, 16(9):3224–3230, 2016.

[73] A. Gruber, A. Dräbenstedt, C. Tietz, L. Fleury, J. Wrachtrup, and C. Von Borczyskowski. Scanning confocal optical microscopy and magnetic resonance on single defect centers. *Science*, 276(5321):2012–2014, 1997.

[74] T Häberle, D Schmid-Lorch, F Reinhard, and J Wrachtrup. Nanoscale nuclear magnetic imaging with chemical contrast. *Nature nanotechnology*, 10(2):125, 2015.

[75] H.-J. Hagemann, W. Gudat, and C. Kunz. Optical Constants from the Far Infrared to the x-Ray Region: Mg, Al, Cu, Ag, Au, Bi, C, and Al2O3. *Journal of the Optical Society of America*, 65(6):742, 1975.

[76] E. L. Hahn. Spin echoes. *Phys. Rev.*, 80:580–594, Nov 1950.

[77] Ali Hajimiri. The Future of High Frequency Circuit Design. In *Proc. of the European Solid State Device Research Conf.*, 2009.

[78] Matti Hämäläinen, Riitta Hari, Risto J. Ilmoniemi, Jukka Knuutila, and Olli V. Lounasmaa. Magnetoencephalography—theory, instrumentation, and applications to noninvasive studies of the working human brain. *Rev. Mod. Phys.*, 65:413–497, Apr 1993.

[79] J. S. Hodges, L. Li, M. Lu, E. H. Chen, M. E. Trusheim, S. Allegri, X. Yao, O. Gaathon, H. Bakhru, and D. Englund. Long-lived NV spin coherence in high-purity diamond membranes. *New J. Phys.*, 14(9), 2012.

[80] Lingyu Hong, Hao Li, Haw Yang, and Kaushik Sengupta. Fully integrated fluorescence biosensors on-chip employing multi-functional nanoplasmonic optical structures in cmos. *IEEE Journal of Solid-State Circuits*, 52(9):2388–2406, 2017.

[81] V. R. Horowitz, B. J. Alemán, D. J. Christle, A. N. Cleland, and D. D. Awschalom. Electron spin resonance of nitrogen-vacancy centers in optically trapped nanodiamonds. *Proceedings of the National Academy of Sciences*, 109(34):34, 2012.

[82] F.M. Hossain, M.W. Doherty, H.F. Wilson, and L.C.L. Hollenberg. Ab initio electronic and optical properties of the n-v-center in diamond. *Phys. Rev. Lett.*, 101(22):226403, 2008.

[83] Zhi Hu, Mehmet Kaynak, and Ruonan Han. High-Power Radiation at 1-THz in Silicon: A Fully Scalable Array Using A Multi-Functional Radiating Mesh Structure. *IEEE Journal of Solid-State Circuits (JSSC)*, 53(5):1313–1327, 2018.

[84] Y. Huang, C. Kao, K. Liu, H. Huang, M. Chiang, C. Soo, H. Chang, T. Chiu, J. Chao, and E. Hwang. The effect of fluorescent nanodiamonds on neuronal survival and morphogenesis. *Scientific Reports*, 4(6919), 2015.

[85] Y. Y. Hui, L. Su, O. Y. Chen, Y. Chen, T. Liu, and H. Chang. Wide-field imaging and flow cytometric analysis of cancer cells in blood by fluorescent nanodiamond labeling and time gating. *Scientific Reports*, 4(5574), 2015.

[86] Peter C Humphreys, Norbert Kalb, Jaco PJ Morits, Raymond N Schouten, Raymond FL Vermeulen, Daniel J Twitchen, Matthew Markham, and Ronald Hanson. Deterministic delivery of remote entanglement on a quantum network. *Nature*, 558(7709):268, 2018.

[87] M. I. Ibrahim, C. Foy, D. Kim, D. R. Englund, and R. Han. Room-temperature quantum sensing in cmos: On-chip detection of electronic spin states in diamond color centers for magnetometry. In *2018 IEEE Symposium on VLSI Circuits*, pages 249–250, 2018.

[88] Mohamed I. Ibrahim, Christopher Foy, Dirk R. Englund, and Ruonan Han. A Scalable Quantum Magnetometer in 65nm CMOS with Vector-Field Detection Capability. In *IEEE International Solid-State Circuits Conference*, pages 458–460, San Francisco, CA, 2019.

[89] Mohamed I. Ibrahim, Christopher Foy, Dirk R. Englund, and Ruonan Han. High-scalability cmos quantum magnetometer with spin-state excitation and detection in diamond color centers. *ArXiv e-prints*, 2020.

[90] IEEE. 2019 heterogeneous integration roadmap (hir) identifies long-term technology requirements to inspire collaboration in the electronics industry. `www.businesswire.com/news/home/20191010005211/en/2019-Heterogeneous-Integration-Roadmap-HIR-Identifies-Long-Term.`, 10 2019.

[91] F. Infante, P. Perdu, S. Petremont, and D. Lewis. A new methodology for short circuit localization on integrated circuits using magnetic microscopy technique coupled with simulations. In *2009 16th IEEE International Symposium on the Physical and Failure Analysis of Integrated Circuits*, pages 208–212, 2009. ISSN: 1946-1550.

[92] Viktor Ivády, Tamás Simon, Jeronimo R. Maze, I. A. Abrikosov, and Adam Gali. Pressure and temperature dependence of the zero-field splitting in the ground state of nv centers in diamond: A first-principles study. *Phys. Rev. B*, 90:235205, Dec 2014.

[93] A. Jarmola, V. M. Acosta, K. Jensen, S. Chemerisov, and D. Budker. Temperature and magnetic-field-dependent longitudinal spin relaxation in nitrogen-vacancy ensembles in diamond. *Physical Review Letters*, 108:197601, 2012.

[94] J.-C. Jaskula, E. Bauch, S. Arroyo-Camejo, M. D. Lukin, S. W. Hell, A. S. Trifonov, and R. L. Walsworth. Superresolution optical magnetic imaging and spectroscopy using individual electronic spins in diamond. *Optics Express*, 25(10):11048–11064, 2017.

[95] J.-C. Jaskula, K. Saha, A. Ajoy, D.J. Twitchen, M. Markham, and P. Cappellaro. Cross-sensor feedback stabilization of an emulated quantum spin gyroscope. *Physical Review Applied*, 11(5), May 2019.

[96] K. Jensen, N. Leefer, A. Jarmola, Y. Dumeige, V. M Acosta, P. Kehayias, B. Patton, and D. Budker. Cavity-enhanced room-temperature magnetometry using absorption by nitrogen-vacancy centers in diamond. *Physical Review Letters*, 112(16):160802, 2014.

[97] W. Jeong, K. Kim, Y. Kim, W. Lee, and P. Reddy. Characterization of nanoscale temperature fields during electromigration of nanowires. *Scientific Reports*, 4(1):4975, 2014.

[98] Jun Ye, H. Schnatz, and L. W. Hollberg. Optical frequency combs: from frequency metrology to optical phase control. *IEEE Journal of Selected Topics in Quantum Electronics*, 9(4):1041–1058, 2003.

[99] P. Kapitanova, V. V. Soshenko, V. V. Vorobyov, D. Dobrykh, S. V. Bolshedvorskii, V. N. Sorokin, and A. V. Akimov. 3D Uniform Manipulation of NV Centers in Diamond Using a Dielectric Resonator Antenna. *JETP Letters*, 108(9):588–595, November 2018.

[100] S. Karaveli, O. Gaathon, A. Wolcott, R. Sakakibara, O. A. Shemesh, D. S. Peterka, E. S. Boyden, J. S. Owen, R. Yuste, and D. Englund. Modulation of nitrogen vacancy charge state and fluorescence in nanodiamonds using electrochemical potential. *Proceedings of the National Academy of Sciences*, 113(15):3938–3943, 2016.

[101] Daiji Kasahara, Daisuke Morita, Takao Kosugi, Kyosuke Nakagawa, Jun Kawamata, Yu Higuchi, Hiroaki Matsumura, and Takashi Mukai. Demonstration of blue and green gan-based vertical-cavity surface-emitting lasers by current injection at room temperature. *Applied Physics Express*, 4(7):072103, 2011.

[102] Donggyu Kim, Mohamed I. Ibrahim, Christopher Foy, Matthew E. Trusheim, Ruonan Han, and Dirk R. Englund. A CMOS-integrated quantum sensor based on nitrogen–vacancy centres. *Nature Electronics*, 2(7):284–289, 2019.

[103] Myeongsub Mike Kim, Alexandre Giry, Mohammad Mastiani, Gustavo O. Rodrigues, Alessandro Reis, and Philippe Mandin. Microscale thermometry: A review. *Microelectronic Engineering*, 148:129 – 142, 2015.

[104] Franziska K. K. Kirschner, Felix Flicker, Amir Yacoby, Norman Y. Yao, and Stephen J. Blundell. Proposal for the detection of magnetic monopoles in spin ice via nanoscale magnetometry. *Phys. Rev. B*, 97:140402, Apr 2018.

[105] I. K. Kominis, T. W. Kornack, J. C. Allred, and M. V. Romalis. A subfemtotesla multichannel atomic magnetometer. *Nature Photonics*, 422:596–599, 2003.

[106] M. Kuball, J. M. Hayes, M. J. Uren, I. Martin, J. C. H. Birbeck, R. S. Balmer, and B. T. Hughes. Measurement of temperature in active high-power AlGaN/GaN HFETs using raman spectroscopy. *IEEE Electron Device Letters*, 23(1):7 – 9, 2002.

[107] M. Kuball and J. W. Pomeroy. A review of raman thermography for electronic and opto-electronic device measurement with submicron spatial and nanosecond temporal resolution. *IEEE Transactions on Device and Materials Reliability*, 16(4):667–684, 2016.

[108] M. Kuball, G.J. Riedel, J.W. Pomeroy, A. Sarua, M.J. Uren, T. Martin, K.P. Hilton, J.O. Maclean, and D.J. Wallis. Time-resolved temperature measurement of AlGaN/GaN electronic devices using micro-raman spectroscopy. *IEEE Electron Device Letters*, 28(2):86–89, 2007.

[109] G. Kucsko, S. Choi, J. Choi, P. C. Maurer, H. Zhou, R. Landig, H. Sumiya, S. Onoda, J. Isoya, F. Jelezko, E. Demler, N. Y. Yao, and M. D. Lukin. Critical thermalization of a disordered dipolar spin system in diamond. *Phys. Rev. Lett.*, 121:023601, Jul 2018.

[110] G. Kucsko, P. C. Maurer, N. Y. Yao, M. Kubo, H. J. Noh, P. K. Lo, H. Park, and M. D. Lukin. Nanometre-scale thermometry in a living cell. *Nature*, 500(7460):54–58, 2013.

[111] G. de Lange, Z. H. Wang, D. Ristè, V. V. Dobrovitski, and R. Hanson. Universal dynamical decoupling of a single solid-state spin from a spin bath. *Science*, 330:60–63, 2010.

[112] A. Laraoui, H. Aycock-Rizzo, Y. Gao, X. Lu, E. Riedo, and C. A. Meriles. Imaging thermal conductivity with nanoscale resolution using a scanning spin probe. *Nature Communications*, 6(8954):8954, 2015.

[113] D. Le Sage, K. Arai, D. R. Glenn, S. J. DeVience, L. M. Pham, L. Rahn-Lee, M. D. Lukin, A. Yacoby, A. Komeili, and R. L. Walsworth. Optical magnetic imaging of living cells. *Nature*, 496(7446):486–489, 2013.

[114] B. Lee. Review of the present status of optical fiber sensors. opt. fiber technol. *IEEE Photonics Technology Letters*, 9(2):57–79, 2003.

[115] J.E Lenz. A review of magnetic sensors. *Proceedings of the IEEE*, 78(6):973–989, 1990.

[116] J.and Sun F.and Song X.and Feng F.and Wang J.and Zhu W.and Lou L.and Wang G. Liu, X.and Cui. Fiber-integrated diamond-based magnetometer. *Applied Physics Letters*, 103(14):143105, 2013.

[117] Michael A. Lombardi, Thomas P. Heavner, and Steven R. Jefferts. Nist primary frequency standards and the realization of the si second. *NCSLI Measure*, 2(4):74–89, 2007.

[118] M. Loretz, T. Rosskopf, and C. L. Degen. Radio-frequency magnetometry using a single electron spin. *Phys. Rev. Lett.*, 110:017602, Jan 2013.

[119] Igor Lovchinsky, JD Sanchez-Yamagishi, EK Urbach, S Choi, S Fang, TI Andersen, K Watanabe, T Taniguchi, A Bylinskii, E Kaxiras, et al. Magnetic resonance spectroscopy of an atomically thin material using a single-spin qubit. *Science*, page eaal2538, 2017.

[120] Igor Lovchinsky, AO Sushkov, E Urbach, NP de Leon, Soonwon Choi, Kristiaan De Greve, R Evans, R Gertner, E Bersin, C Müller, et al. Nuclear magnetic resonance detection and spectroscopy of single proteins using quantum logic. *Science*, 351(6275):836–841, 2016.

[121] R. Lutwak, J. Deng, W. Riley, M. Varghese, J. Leblanc, G. Tepolt, M. Mescher, D. K. Serkland, K. M. Geib, and G. M. Peake. The chip-scale atomic clock - low-power physics package. In *Proceedings of the 36th Annual Precise Time and Time Interval Systems and Applications Meeting*, pages 339–354, 2012.

[122] Shai Maayani, Christopher Foy, Yoel Fink, and Dirk R. Englund. Distributed quantum fiber magnetometry. *Laser & Photonics Reviews*, 2019.

[123] B.J. Maertz, A.P. Wijnheijmer, G.D. Fuchs, M.E. Nowakowski, and D.D. Awschalom. Vector magnetic field microscopy using nitrogen vacancy centers in diamond. *Applied Physics Letters*, 96(9):092504, 2010.

[124] H. J. Mamin, M. H. Sherwood, M. Kim, C. T. Rettner, K. Ohno, D. D. Awschalom, and D. Rugar. Multipulse double-quantum magnetometry with near-surface nitrogen-vacancy centers. *Phys. Rev. Lett.*, 113:030803, Jul 2014.

[125] HJ Mamin, M Kim, MH Sherwood, CT Rettner, K Ohno, DD Awschalom, and D Rugar. Nanoscale nuclear magnetic resonance with a nitrogen-vacancy spin sensor. *Science*, 339(6119):557–560, 2013.

[126] N.B. Manson, J.P. Harrison, and Sellars M.J. Nitrogen-vacancy center in diamond: Model of the electronic structure and associated dynamics. *Phys. Rev. B*, 74(104303):104303, 2006.

[127] J.R Maze, P.L Stanwix, J.S Hodges, S. Hong, J.M. Taylor, P. Cappellaro, L. Jiang, M.V. Gurudev Dutt, E. Togan, A.S Zibrov, A. Yacoby, R.L. Walsworth, and M.D. Lukin. Nanoscale magnetic sensing with an individual electronic spin in diamond. *Nature*, 455(7213):644–647, 2008.

[128] T. Mittiga, S. Hsieh, C. Zu, B. Kobrin, F. Machado, P. Bhattacharyya, N.Z. Rui, A. Jarmola, S. Choi, D. Budker, and N.Y. Yao. Imaging the local charge environment of nitrogen-vacancy centers in diamond. *Physical Review Letters*, 121(24):246402, 2018.

[129] David J Moss, Roberto Morandotti, Alexander L Gaeta, and Michal Lipson. New cmos-compatible platforms based on silicon nitride and hydex for nonlinear optics. *Nature photonics*, 7(8):597, 2013.

[130] M Mrózek, D. Rudnicki, P. Kehayias, A. Jarmola, D. Budker, and W. Gawlik. Longitudinal spin relaxation in nitrogen-vacancy ensembles in diamond. *EPJ Quantum Technology*, 2:1–11, 2015.

[131] Kartikeya Murari, Ralph Etienne-Cummings, Nitish Thakor, and Gert Cauwenberghs. Which photodiode to use: a comparison of cmos-compatible structures. *IEEE sensors journal*, 9(7):752–760, 2009.

[132] M. F.; Vengsarkar A. M.; Claus R. O. Murphy, K. A.; Gunther. Quadrature phase-shifted, extrinsic fabry–perot optical fiber sensors. *Optics Letters*, 16(4):273–275, 1991.

[133] A. Nagl, S. R. Hemelaar, and R. Schirhagl. Improving surface and defect center chemistry of fluorescent nanodiamonds for imaging purposes–a review. *Analytical and Bioanalytical Chemistry*, 407(25):7521–7536, 2015.

[134] Felix Neugart, Andrea Zappe, Fedor Jelezko, C. Tietz, Jean Paul Boudou, Anke Krueger, and Jörg Wrachtrup. Dynamics of diamond nanoparticles in solution and cells. *Nano Letters*, 7(12):3588–3591, 2007. PMID: 17975943.

[135] P. Neumann, I. Jakobi, F. Dolde, C. Burk, R. Reuter, G. Waldherr, J. Honert, T. Wolf, A. Brunner, J. H. Shim, D. Suter, H. Sumiya, J. Isoya, and J. Wrachtrup. High-Precision Nanoscale Temperature Sensing Using Single Defects in Diamond. *Nano Letters*, 13(6):2738–2742, 2013.

[136] Newport. Technical note. `https://www.newport.com/n/gaussian-beam-optics`, April 2020.

[137] Thomas Oeckinghaus, Rainer Stöhr, Roman Kolesov, Julia Tisler, Friedemann Reinhard, and Jörg Wrachtrup. A compact, diode laser based excitation system for microscopy of nv centers. *Review of Scientific Instruments*, 85(7):073101, 2014.

[138] The Royal Swedish Academy of Sciences. Nobelprize.org. *NobelPrize.org*, Oct 1991.

[139] The Royal Swedish Academy of Sciences. Nobelprize.org. *NobelPrize.org*, Oct 1997.

[140] The Royal Swedish Academy of Sciences. Nobelprize.org. *NobelPrize.org*, Oct 2001.

[141] Edmund Optics. Using tube lenses with infinity corrected objectives. `https://www.edmundoptics.com/knowledge-center/application-notes/microscopy/using-tube-lenses-with-infinity-corrected-objectives/`, April 2020.

[142] Preeti Ovartchaiyapong, Kenneth W Lee, Bryan A Myers, and Ania C Bleszynski Jayich. Dynamic strain-mediated coupling of a single diamond spin to a mechanical resonator. *Nature communications*, 5:4429, 2014.

[143] Bishnu Patra, Rosario M Incandela, Jeroen PG Van Dijk, Harald AR Homulle, Lin Song, Mina Shahmohammadi, Robert Bogdan Staszewski, Andrei Vladimirescu, Masoud Babaie, Fabio Sebastiano, et al. Cryo-cmos circuits and systems for quantum computing applications. *IEEE Journal of Solid-State Circuits*, 2018.

[144] M. Pelliccione, B. A. Myers, L. M. A. Pascal, A. Das, and A. C. Bleszynski Jayich. Two-dimensional nanoscale imaging of gadolinium spins via scanning probe relaxometry with a single spin in diamond. *Phys. Rev. Applied*, 2:054014, Nov 2014.

[145] Song Peng and G Michael Morris. Resonant scattering from two-dimensional gratings. *JOSA A*, 13(5):993–1005, 1996.

[146] E. Perevedentseva, Y. Lin, M. Jani, and C. Cheng. Biomedical Applications of Nanodiamonds: Imaging and Therapy. *Nanomedicine*, 8(12), 2013.

[147] Wolfgang Pfaff, BJ Hensen, Hannes Bernien, Suzanne B van Dam, Machiel S Blok, Tim H Taminiau, Marijn J Tiggelman, Raymond N Schouten, Matthew Markham, Daniel J Twitchen, et al. Unconditional quantum teleportation between distant solid-state quantum bits. *Science*, 345(6196):532–535, 2014.

[148] Matthias Pfender, Nabeel Aslam, Gerald Waldherr, Philipp Neumann, and Jörg Wrachtrup. Single-spin stochastic optical reconstruction microscopy. *Proceedings of the National Academy of Sciences*, 111(41):14669–14674, 2014.

[149] L. M. Pham, S. J. Devience, F. Casola, I. Lovchinsky, A. O. Sushkov, E. Bersin, J. Lee, E Urbach, P. Cappellaro, H. Park, A. Yacoby, Y.M. Lukin, and R.L Walsworth. Nmr technique for determining the depth of shallow nitrogen-vacancy centers in diamond. *Physical Review Applied*, 93:045425, 2016.

[150] T. Plakhotnik, M. W. Doherty, J. H. Cole, R. Chapman, and N. B. Manson. All-Optical Thermometry and Thermal Properties of the Optically Detected Spin Resonances of the nv– Center in Nanodiamonds. *Nano Letters*, 14(9):4989–4996, 2014.

[151] T. Plakhotnik, M. W. Doherty, J. H. Cole, R. Chapman, and N. B. Manson. All-optical thermometry and thermal properties of the optically detected spin resonances of the Nv-center in nanodiamond. *Nano Letters*, 14(9):4989–4996, 2014.

[152] QDT. Quantum diamond technology. `https://quantumdiamondtech.com/`, April 2020.

[153] Qnami. The quantum wave. `https://qnami.ch/`, January 2020.

[154] QuSpin. Qzfm gen-2. `https://quspin.com/products-qzfm/`, 2020.

[155] Surjeet Rajendran, Nicholas Zobrist, Alexander O. Sushkov, Ronald Walsworth, and Mikhail Lukin. A method for directional detection of dark matter using spectroscopy of crystal defects. *Phys. Rev. D*, 96:035009, Aug 2017.

[156] Aleksandar D. Rakić, Aleksandra B. Djurišić, Jovan M. Elazar, and Marian L. Majewski. Optical Properties of Metallic Films for Vertical-Cavity Optoelectronic Devices. *Applied Optics*, 37(22):5271, 1998.

[157] Norman F. Ramsey. A molecular beam resonance method with separated oscillating fields. *Phys. Rev.*, 78:695–699, Jun 1950.

[158] Behzad Razavi. *RF microelectronics*, volume 2. Prentice Hall New Jersey, 1998.

[159] M. Rein, V. D. Favrod, C. Hou, T. Khudiyev, A. Stolyarov, J. Cox, C.-C. Chung, C. Chhav, M. Ellis, J. Joannopoulos, and Y. Fink. Diode fibres for fabric-based optical communications. *Nature*, 560(7717):214–218, 2018.

[160] L. Rondin, J.-P. Tetienne, T. Hingant, J.-F. Roch, P. Maletinsky, and V. Jacques. Magnetometry with nitrogen-vacancy defects in diamond. *Reports on Progress in Physics*, 77(5), 2013.

[161] T. Rosskopf, A. Dussaux, K. Ohashi, M. Loretz, R. Schirhagl, H. Watanabe, S. Shikata, K. M. Itoh, and C. L. Degen. Investigation of surface magnetic noise by shallow spins in diamond. *Physical Review Letters*, 112:147602, 2014.

[162] D Rugar, HJ Mamin, MH Sherwood, M Kim, CT Rettner, K Ohno, and DD Awschalom. Proton magnetic resonance imaging using a nitrogen–vacancy spin sensor. *Nature nanotechnology*, 10(2):120, 2015.

[163] A. Sarua, H. Ji, M. Kuball, M.J. Uren, T. Martin, K.P. Hilton, and R.S. Balmer. Integrated micro-Raman/infrared thermography probe for monitoring of self-heating in Algan/Gan transistor structures. *IEEE Transactions on Electron Devices*, 53(10):2438 – 2447, 2006.

[164] R. Schirhagl, K. Chang, M. Loretz, and C. L. Degen. Nitrogen-Vacancy Centers in Diamond: Nanoscale Sensors for Physics and Biology. *Annual Review of Physical Chemistry*, 65(1):83–105, 2014.

[165] Romana Schirhagl, Kevin Chang, Michael Loretz, and Christian L Degen. Nitrogen-vacancy centers in diamond: Nanoscale sensors for physics and biology. *Annual review of physical chemistry*, 2013.

[166] J. M. Schloss, J. F. Barry, M. J. Turner, and R.L. Walsworth. Simultaneous broadband vector magnetometry using solid-state spins. *Physical Review Applied*, 10(3):034044, 2018.

[167] J.M Schloss. *Optimizing Nitrogen-Vacancy Diamond Magnetic Sensors and Imagers for Broadband Sensitivity*. PhD thesis, MASSACHUSETTS INSTITUTE OF TECHNOLOGY, 2019.

[168] Yechezkel Schlussel, Till Lenz, Dominik Rohner, Yaniv Bar-Haim, Lykourgos Bougas, David Groswasser, Michael Kieschnick, Evgeny Rozenberg, Lucas Thiel, Amir Waxman, Jan Meijer, Patrick Maletinsky, Dmitry Budker, and Ron Folman. Wide-field imaging of superconductor vortices with electron spins in diamond. *Phys. Rev. Applied*, 10:034032, Sep 2018.

[169] S. Schmitt, T. Gefen, T. Stürner, F. M. Unden, G. Wolff, C. Müller, J. Scheuer, B. Naydenov, M. Markham, S. Pezzagna, J. Meijer, I. Schwarz, M. Plenio, A. Retzker, L. P. McGuinness, and F. Jelezko. Submillihertz magnetic spectroscopy performed with a nanoscale quantum sensor. *Science*, 356(6340):832–837, 2017.

[170] Simon Schmitt, Tuvia Gefen, Felix M. Stürner, Thomas Unden, Gerhard Wolff, Christoph Müller, Jochen Scheuer, Boris Naydenov, Matthew Markham, Sebastien Pezzagna, Jan Meijer, Ilai Schwarz, Martin Plenio, Alex Retzker, Liam P. McGuinness, and Fedor Jelezko. Submillihertz magnetic spectroscopy performed with a nanoscale quantum sensor. *Science*, 356(6340):832–837, 2017.

[171] Rolf Simon Schoenfeld and Wolfgang Harneit. Real time magnetic field sensing and imaging using a single spin in diamond. *Phys. Rev. Lett.*, 106:030802, Jan 2011.

[172] A. W.and Kewes G.and Aichele T.and Benson Schroder, T.and Schell. Fiber-integrated diamond-based single photon source. *Nano Letters*, 11(1):198–202, 2010.

[173] Kaushik Sengupta and Ali Hajimiri. A 0.28 THz Power-Generation and Beam-Steering Array in CMOS Based on Distributed Active Radiators. *IEEE Journal of Solid-State Circuits*, 47(12):3013–3031, 2012.

[174] V. Shah, S. Knappe, P.D.D Schwindt, and J. Kitching. Subpicotesla atomic magnetometry with a microfabricated vapour cell. *Nature Photonics*, 1:649–652, 2007.

[175] Linbo Shao, Mian Zhang, Matthew Markham, Andrew M. Edmonds, and Marko Lončar. Diamond radio receiver: Nitrogen-vacancy centers as fluorescent transducers of microwave signals. *Phys. Rev. Applied*, 6:064008, Dec 2016.

[176] Or A. Shemesh, Ishan Gupta, Ophir Gaathon, Christopher Foy, Sinan Karaveli, Jae-Byum Chang, Asmamaw Wassie, Abraham Wolcott, Daniel A. Martin-Alarcon, Reyu Sakakibara, Dirk Englund, and Edward S. Boyden. Membrane-targeted delivery of nitrogen vacancy nanodiamonds. *In preparation*, 2020.

[177] C. S. Shin, C. E. Avalos, M. C. Butler, D. R. Trease, S. J. Seltzer, P.J. Mustonen, D. J. Kennedy, V. M. Acosta, D. Budker, A. Pines, and V. S. Bajaj. Room-temperature operation of a radiofrequency diamond magnetometer near the shot-noise limit. *Journal Applied Physics*, 112(12):124519, 2012.

[178] D. A. Simpson, E. Morrisroe, J. M. McCoey, A. H. Lombard, D. C. Mendis, F. Treussart, L. T. Hall, S. Petrou, and L. C. L. Hollenberg. Non-Neurotoxic Nanodiamond Probes for Intraneuronal Temperature Mapping. *ACS Nano*, 11(12):12077, 2017.

[179] L. Soto, M. A.and Thévenaz. Modeling and evaluating the performance of brillouin distributed optical fiber sensors. *Optics Express*, 21(25):31347–31366, 2013.

[180] P. L. Stanwix, L. M. Pham, J. R. Maze, D. Le Sage, T. K. Yeung, P. Cappellaro, P. R. Hemmer, A. Yacoby, M. D. Lukin, and R. L. Walsworth. Coherence of Nitrogen-Vacancy Electronic Spin Ensembles in Diamond. *Physical Review B*, 82(20), 2010.

[181] Tobias Staudacher, Fazhan Shi, S Pezzagna, Jan Meijer, Jiangfeng Du, Carlos A Meriles, Friedemann Reinhard, and Joerg Wrachtrup. Nuclear magnetic resonance spectroscopy on a (5-nanometer) 3 sample volume. *Science*, 339(6119):561–563, 2013.

[182] S. Steinert, F. Dolde, P. Neumann, A. Aird, B. Naydenov, G. Balasubramanian, F. Jelezko, and J. Wrachtrup. High sensitivity magnetic imaging using an array of spins in diamond. *Review of Scientific Instruments*, 81(4):043705, 2010.

[183] S. Steinert, F. Ziem, L. T. Hall, A. Zappe, M. Schweikert, N. Götz, A. Aird, G. Balasubramanian, L. Hollenberg, and J. Wrachtrup. Magnetic Spin Imaging under Ambient Conditions with Sub-Cellular Resolution. *Nature Communications*, 4:1–6, 2013.

[184] A. M. Stolyarov, L. Wei, O. Shapira, F. Sorin, S. L. Chua, J. D. Joannopoulos, and Y. Fink. Microfluidic directional emission control of an azimuthally polarized radial fibre laser. *Nature Photonics*, 6(4):229–233, 2012.

[185] H.F. Talbot. Facts Relating to Optical Science. No. IV. *The London, Edinburgh, and Dublin Philosophical Magazine and Journal of Science*, 9(56):401–407, 1836.

[186] R. Tanimoto, T. Hiraiwa, Y. Nakai, Y. Shindo, K. Oka, N. Hiroi, and A. Funahashi. Detection of Temperature Difference in Neuronal Cells. *Scientific Reports*, 6(22071):22071, 2016.

[187] J. M. Taylor, P. Cappellaro, L. Childress, L. Jiang, D. Budker, P. R. Hemmer, A. Yacoby, R. Walsworth, and M. D. Lukin. High-sensitivity diamond magnetometer with nanoscale resolution. *Nature Physics*, 4(10):810–816, 2008.

[188] J.M. Taylor, P. Cappellaro, L. Childress, L. Jiang, D. Budker, A. Hemmer, P.R .and Yacoby, R. Walsworth, and M.D. Lukin. High-sensitivity diamond magnetometer with nanoscale resolution. *Nature Physics*, 4(10):810–816, 2008.

[189] TECHIMAGING. *Photron*, 11 2018.

[190] J Teissier, A Barfuss, P Appel, E Neu, and P Maletinsky. Strain coupling of a nitrogen-vacancy center spin to a diamond mechanical oscillator. *Physical review letters*, 113(2):020503, 2014.

[191] J.-P. Tetienne, T. Hingant, L. J. Martínez, S. Rohart, A. Thiaville, L. Herrera Diez, K. Garcia, J.-P. Adam, J.-V. Kim, J.-F. Roch, I. M. Miron, G. Gaudin, L. Vila, B. Ocker, D. Ravelosona, and V. Jacques. The nature of domain walls in ultrathin ferromagnets revealed by scanning nanomagnetometry. *Nature Communications*, 6(6733):6733, 2015.

[192] J.-P. Tetienne, T. Hingant, L. Rondin, A. Cavaillès, L. Mayer, G. Dantelle, T. Gacoin, J. Wrachtrup, J.-F. Roch, and V. Jacques. Spin relaxometry of single nitrogen-vacancy defects in diamond nanocrystals for magnetic noise sensing. *Phys. Rev. B*, 87:235436, Jun 2013.

[193] J-P Tetienne, L Rondin, P Spinicelli, M Chipaux, T Debuisschert, J-F Roch, and V Jacques. Magnetic-field-dependent photodynamics of single NV defects in diamond: an application to qualitative all-optical magnetic imaging. *New Journal of Physics*, 14(10):103033, oct 2012.

[194] Jean-Philippe Tetienne, Alain Lombard, David A. Simpson, Cameron Ritchie, Jianing Lu, Paul Mulvaney, and Lloyd C. L. Hollenberg. Scanning nanospin ensemble microscope for nanoscale magnetic and thermal imaging. *Nano Letters*, 16(1):326–333, 2016.

[195] D. M. Toyli, D. J. Christle, A. Alkauskas, B. B. Buckley, C. G. Van de Walle, and D. D. Awschalom. Measurement and control of single nitrogen-vacancy center spins above 600 k. *Phys. Rev. X*, 2:031001, Jul 2012.

[196] D. M. Toyli, C. F. de las Casas, D. J. Christle, V. V. Dobrovitski, and D. D. Awschalom. Fluorescence thermometry enhanced by the quantum coherence of single spins in diamond. *Proc. Natl. Acad. Sci.*, 110:8417–8421, 2013.

[197] M. E. Trusheim, L. Li, A Laraoui, E. H. Chen, H. Bakhru, T. Schröder, O. Gaathon, C. A. Meriles, and D. Englund. Scalable Fabrication of High Purity Diamond Nanocrystals with Long- Spin-Coherence Nitrogen Vacancy Centers. *Nano Letters*, 14(1):32–36, 2014.

[198] Matthew E Trusheim and Dirk Englund. Wide-field strain imaging with preferentially aligned nitrogen-vacancy centers in polycrystalline diamond. *New Journal of Physics*, 18(12):123023, dec 2016.

[199] M.E Trusheim. *Nanoscale Engineering of Spin-Based Quantum Devices in Diamond*. PhD thesis, MASSACHUSETTS INSTITUTE OF TECHNOLOGY, 2018.

[200] K. N. Tu, Yingxia Liu, and Menglu Li. Effect of joule heating and current crowding on electromigration in mobile technology. *Applied Physics Reviews*, 4(1):011101, 2017.

[201] TwinLeaf. microserf. `https://twinleaf.com/vector/microSERF/`, 2020.

[202] Thomas Unden, Priya Balasubramanian, Daniel Louzon, Yuval Vinkler, Martin B Plenio, Matthew Markham, Daniel Twitchen, Alastair Stacey, Igor Lovchinsky, Alexander O Sushkov, et al. Quantum metrology enhanced by repetitive quantum error correction. *Physical review letters*, 116(23):230502, 2016.

[203] M Veldhorst, HGJ Eenink, CH Yang, and AS Dzurak. Silicon cmos architecture for a spin-based quantum computer. *Nature communications*, 8(1):1766, 2017.

[204] S. A. Wade, S. F. Collins, and G. W. Baxter. Fluorescence intensity ratio technique for optical fiber point temperature sensing. *Journal of Applied Physics*, 94(8):4743–4756, 2003.

[205] Albert Wang and Alyosha Molnar. A light-field image sensor in 180 nm CMOS. *IEEE Journal of Solid-State Circuits*, 47(1):257–271, 2012.

[206] Cheng Wang and Ruonan Han. Molecular Detection for Unconcentrated Gas with ppm Sensitivity Using Dual-THz-Comb Spectrometer in CMOS. *IEEE Trans. Biomedical Circuits and Systems*, 12(3):709–721, 2018.

[207] Cheng Wang, Xiang Yi, James Mawdsley, Mina Kim, Zihan Wang, and Ruonan Han. An On-Chip Fully-Electronic Molecular Clock Based on sub-THz Rotational Spectroscopy. *Nature Electronics*, 1(7):421–427, 2018.

[208] N.and Tian Y.and Niezrecki C.and Wang X. Wang, W.and Wu. A novel temperature-insensitive optical fiber pressure sensor for harsh environments. *IEEE Photonics Technology Letter*, 17(4):870–872, 2005.

[209] P. Wang, Z. Yuan, P. Huang, X. Rong, M. Wang, X. Xu, C. Duan, C. Ju, F. Shi, and J. Du. High-resolution vector microwave magnetometry based on solid-state spins in diamond. *Nature Communications*, 6(6631):6631, 2015.

[210] W.L Webb. Aircraft navigation instruments. *Electrical Engineering*, 70(5):384–389, 1951.

[211] Jianming Wen, Yong Zhang, and Min Xiao. The talbot effect: recent advances in classical optics, nonlinear optics, and quantum optics. *Advances in optics and photonics*, 5(1):83–130, 2013.

[212] Adam M. Wojciechowski, Mürsel Karadas, Alexander Huck, Christian Osterkamp, Steffen Jankuhn, Jan Meijer, Fedor Jelezko, and Ulrik L. Andersen. Contributed review: Camera-limits for wide-field magnetic resonance imaging with a nitrogen-vacancy spin sensor. *Review of Scientific Instruments*, 89(3):031501, 2018.

[213] Thomas Wolf, Philipp Neumann, Kazuo Nakamura, Hitoshi Sumiya, Takeshi Ohshima, Junichi Isoya, and Jörg Wrachtrup. Subpicotesla diamond magnetometry. *Physical Review X*, 5(4):041001, 2015.

[214] James D. A. Wood, David A. Broadway, Liam T. Hall, Alastair Stacey, David A. Simpson, Jean-Philippe Tetienne, and Lloyd C. L. Hollenberg. Wide-band nanoscale magnetic resonance spectroscopy using quantum relaxation of a single spin in diamond. *Phys. Rev. B*, 94:155402, Oct 2016.

[215] Y. Wu, F. Jelezko, M. B. Plenio, and T. Weil. Diamond quantum devices in biology. *Angewandte Chemie*, 55(23), 2016.

[216] G. Xu, J.and Pickrell and W.and Cooper K.and Wang A. Wang, X.and Peng. A novel temperature-insensitive optical fiber pressure sensor for harsh environments. *IEEE Photonics Technology Letter*, 17(4):870–872, 2005.

[217] Norman Y Yao, Liang Jiang, Alexey V Gorshkov, Peter C Maurer, Geza Giedke, J Ignacio Cirac, and Mikhail D Lukin. Scalable architecture for a room temperature solid-state quantum information processor. *Nature communications*, 3:800, 2012.

[218] W. Yuan, A. Stefani, and O. Bang. Tunable polymer fiber bragg grating (fbg) inscription: Fabrication of dual-fbg temperature compensated polymer optical fiber strain sensors. *IEEE Photonics Technology Letters*, 24(5):401, 2012.

[219] C Patrick Yue and S Simon Wong. On-chip spiral inductors with patterned ground shields for si-based rf ics. *IEEE Journal of solid-state circuits*, 33(5):743–752, 1998.

[220] E. Zanoni, M. Meneghini, A. Chini, D. Marcon, and G. Meneghesso. AlGaN/GaN-based HEMTs failure physics and reliability: Mechanisms affecting gate edge and schottky junction. *IEEE Transactions on Electron Devices*, 60(10):3119 – 3131, 2013.

[221] Anatoly V Zayats, Igor I Smolyaninov, and Alexei A Maradudin. Nano-optics of surface plasmon polaritons. *Physics reports*, 408(3-4):131–314, 2005.

[222] L. Zhang, Z. Lu, Y. Song, L. Zhao, B. Bhatia, K.R. Bagnall, and E.N. Wang. Thermal expansion coefficient of monolayer molybdenum disulfide using micro-raman spectroscopy. *Nano Letters*, 19(7):4745–4751, 2019.

[223] Ning Zhang, Chen Zhang, Lixia Xu, Ming Ding, Wei Quan, Zheng Tang, and Heng Yuan. Microwave Magnetic Field Coupling with Nitrogen-Vacancy Center Ensembles in Diamond with High Homogeneity. *Applied Magnetic Resonance*, 47(6):589–599, 2016.